THE JOURNAL OF PHYSICAL CHEMISTRY C

Article

pubs.acs.org/JPCC

Electronic States at Low-Angle Grain Boundaries in Polycrystalline Naphthalene

Marko Mladenović,*[,†,‡] Nenad Vukmirović,[†] and Igor Stanković[†]

[†]Scientific Computing Laboratory, Institute of Physics Belgrade, University of Belgrade, Pregrevica 118, 11080 Belgrade, Serbia

[‡]School of Electrical Engineering, University of Belgrade, P.O. Box 35-54, 11120 Belgrade, Serbia

ABSTRACT: We investigated the influence of grain boundaries on electronic properties of polycrystalline organic semiconductor naphthalene. The atomic structure of grain boundaries was found using a Monte Carlo method, whereas electronic structure calculations were performed using the charge patching method. We found that grain boundaries introduce trap states within the band gap of the material. Our results show that spatial positions and energies of trap states can be predicted solely from geometrical arrangement of molecules near the boundary. Wave functions of these states are localized on closely spaced pairs of molecules from opposite sides of the boundary. The energies of trap states are strongly correlated with the distances between the molecules in the pair. These findings were used to calculate the electronic density of trap states, which was found to exhibit a qualitatively different behavior for grain boundaries perpendicular to the *a* and *b* directions of the crystal unit cell.

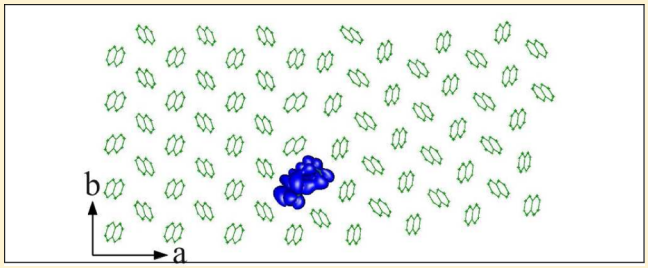

INTRODUCTION

Organic semiconductors are materials of great promise for electronic devices, such as organic field-effect transistors (FETs), organic light-emitting diodes (LEDs), and organic solar cells (OSCs).[1−7] Their advantage over inorganic counterparts is that they are flexible and have a low processing cost. However, devices made of organic semiconductors still have relatively low charge mobility and low efficiency. Small molecule based crystalline organic semiconductors (such as tetracene, pentacene, rubrene, etc.) exhibit the highest mobilities among organic semiconductors due to their crystalline structures. Electronic devices based on these materials are typically obtained using the vacuum-evaporation technique.[8−13] More recently, it became possible to use an inexpensive solution processing technique to obtain structures with a high degree of crystallinity and good charge transport properties,[14−19] which opens the way toward large-scale applications of small molecule based organic semiconductors. Therefore, researchers put effort into improving properties of these materials in order to make them competitive with inorganic semiconductors.

Thin films of crystalline organic semiconductors have a polycrystalline form, which is composed of many different crystalline grains. It has been shown that the transport in a single grain boundary device is limited by the grain boundary.[9] A pronounced dependence of transistor characteristics on the grain size was also established,[12,15,16,20] as well as a strong difference between the characteristics of single-crystal and polycrystalline transistors based on the same material.[11] It was also shown that grain boundary orientation has a large influence on the charge carrier mobility.[18] All of these results indicate that grain boundaries are the most limiting intrinsic factor for efficient charge transport in small molecule based polycrystalline organic semiconductors.

However, there is still a lack of understanding of the specific mechanism by which grain boundaries affect the charge transport. It is typically assumed that they introduce trap states localized at the grain boundary, with energies of these states within the band gap of the material.[9,11,12,20−22] The charges in the trap states do not contribute to transport, and therefore, the presence of traps reduces the effective charge carrier mobility. On the other hand, there are some suggestions that grain boundaries act as barriers and that charge carriers are trapped in the grains.[23,24] Calculations of electrostatic potential at molecules near the grain boundary formed from two misaligned grains indicate the presence of trapping centers at the boundary.[25] Other theoretical and computational studies are primarily focused on the properties of single crystals.[26−37]

In this paper, we shed light on the nature of electronic states at grain boundaries in organic crystalline semiconductors. We directly calculate the wave functions of electronic states and gain microscopic insight into the origin of these states. Using these insights, we develop a simple model for density of trap states prediction. In the following section, the method for electronic structure calculation is introduced. We use naphthalene as a representative of crystalline organic semiconductors based on small molecules. The results of the calculation of electronic states at grain boundaries are

Received: May 16, 2013
Revised: June 26, 2013
Published: July 1, 2013

presented. We find that grain boundaries produce trap states in the band gap, where the highest states are localized on pairs of molecules at the grain boundary, whose mutual distance is much smaller than the corresponding distance in the monocrystal. Strong correlation between the mutual distance between these molecules and the energies of these states was found. Such a correlation enables one to calculate the electronic density of states at the grain boundary directly from mutual distances between molecules. Finally, the results obtained are discussed with a particular focus on their relation to the current body of knowledge about grain boundaries in organic polycrystals.

METHOD FOR ELECTRONIC STRUCTURE CALCULATIONS

The method used for electronic structure calculations of grain boundaries in polycrystalline naphthalene is schematically described in Figure 1. The atomic structure is obtained from

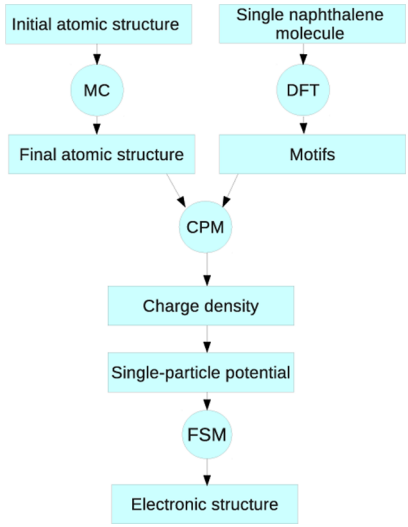

Figure 1. Schematic representation of the algorithm for electronic structure calculations.

a relaxation procedure based on a Monte Carlo (MC) method[38] and is subsequently used to calculate the electronic states using the density functional theory (DFT)[39] based charge patching method (CPM).[40,41]

The initial configuration for MC relaxation is two monocrystals with different crystalline orientations joined at their common boundary. Potential energy of a system is calculated using transferable potentials for phase equilibria (TraPPE).[42,43] Naphthalene molecules are considered as rigid bodies; hence, only interactions between carbon atoms from different molecules described by the weak van der Waals interaction are taken into account. Carbon-hydrogen (CH) groups are treated as one atom with a center of mass at carbon atoms. TraPPE parameters for interactions between CH groups are σ = 3.695 Å, ε/k_B = 50.5 K and, for interaction between C atoms, σ = 3.7 Å, ε/k_B = 30 K. An MC algorithm was then used to minimize the energy of the system. In each step of the MC algorithm, one molecule is randomly chosen, translated for a randomly chosen vector, and rotated by a randomly chosen angle. The decision about the acceptance of this move is made according to the Metropolis algorithm: if the energy of the new configuration is lower than the initial, the move is accepted; otherwise, it is accepted with a probability equal to the Boltzmann weight of the difference of the energy of the new and the old configuration.[38] The simulation is performed until a thermal equilibrium is reached, which is evidenced by the saturation in the dependence of the energy on the number of simulation steps. Simulation is performed at a temperature of 300 K. After the thermal equilibrium is reached, the system is gradually cooled down to 0 K. In this way, dynamic disorder (crystal disorder induced by thermal motion) effects[26] are excluded. Both the effects of dynamic disorder and grain boundaries can, in principle, induce localized states, and it would be very difficult to distinguish between these if the electronic structure calculations were performed for a structure obtained from a snapshot of MC simulations at 300 K. To check that the choice of the temperature of 300 K has only a small effect on the final atomic structure obtained from an MC procedure, we repeated the simulations using the temperatures of 100, 200, and 400 K, as well. Atomic structures obtained from these simulations were nearly identical as the atomic structure obtained from the simulation at 300 K. Therefore, the MC simulation procedure is robust in the sense that the final structure is weakly dependent on the details of the procedure.

TraPPE empirical potentials were previously used for a variety of organic materials.[43−45] The validity of the potentials used in the MC simulation was verified by comparing the naphthalene crystal lattice constants obtained from these empirical potentials to the values from the literature. The initial structure for the crystal lattice parameters optimization is the naphthalene unit cell with the lattice parameters and atomic structure given in ref 46. It is assumed that two angles of the unit cell are 90°, since the naphthalene unit cell is monoclinic.[47] Other unit cell parameters (three lengths and one angle) were varied and MC relaxation was performed for each combination of the unit cell parameters until the convergence of the potential energy was satisfied. In the same manner as for the atomic structure of grain boundaries, the simulation was first performed at 300 K, followed by gradually cooling down to 0 K. The obtained lattice constants are constants that give the crystal lattice with minimal potential energy: a = 8.325 Å, b = 5.92 Å, c = 7.77 Å, and β = 63°. In the literature, there are several results for naphthalene unit cell parameters: In ref 48: a = 8.4 Å, b = 6 Å, c = 8.66 Å, and β = 57.1°. In ref 49: a = 8.098 Å, b = 5.953 Å, c = 8.652 Å, and β = 55.6°. Therefore, lattice constants obtained with TraPPE empirical potentials are in good agreement with previous results. Simulations were performed using temperatures other than 300 K, as well, to check the correctness of the procedure and the results. For additional evaluation of the validity of empirical potentials, the melting temperature of naphthalene was calculated as the temperature of the heat capacity peak.[50] The calculated melting temperature is 340 ± 5 K, which is close to the melting temperature of 352.5 K given in ref 51.

After the atomic structure is obtained, electronic structure calculations can be performed. In principle, DFT can be used for that. However, to avoid finite size effects on the electronic states at the grain boundaries, one needs to include a sufficiently large number of unit cells in the plane of the boundary, as well as several molecular layers nearest to the boundary. This typically includes several thousand atoms, which is beyond the reach of standard DFT calculations. Therefore, the CPM was used instead of standard DFT. CPM is a strong tool by which one can directly construct the electronic charge density instead of self-consistently solving the

dx.doi.org/10.1021/jp404825h | J. Phys. Chem. C 2013, 117, 15741−15748

Kohn−Sham equations as in standard calculations based on DFT. In the CPM, an appropriate motif is assigned to each atom in the system. Motif is a description of the environment of an atom. It contains the information about the types of the central atom and its neighbors. There are five motifs in the system that consists of naphthalene molecules only: C_3−$C_3C_2C_2$, C_2−C_3C_2H, C_2−C_2C_2H, H−C_2−C_2C_2, and H−C_2−C_3C_2, where C_X is the carbon atom connected to X other carbon atoms. Charge density of a motif associated with an atom A is calculated using the formula

$$m_A(\mathbf{r} - \mathbf{R}_A) = \frac{w_A(\mathbf{r} - \mathbf{R}_A)}{\sum_B w_B(\mathbf{r} - \mathbf{R}_B)}\rho(\mathbf{r}) \quad (1)$$

where $\rho(\mathbf{r})$ is the charge density of a single naphthalene molecule obtained by DFT calculations, while $\mathbf{R}_A$ and w_A are, respectively, the position and the weight function of the atom A. Overall charge density is then calculated as a sum of all motif charge densities in the system. With charge density at hand, the single-particle Hamiltonian is given as

$$H = -\frac{\hbar^2}{2m_0}\nabla^2 + v_I + \frac{e}{4\pi\varepsilon_0}\int\frac{\rho(\mathbf{r}')}{|\mathbf{r} - \mathbf{r}'|}d\mathbf{r}' + v_{xc}^{\mathrm{LDA}}(\rho) \quad (2)$$

The first term in eq 2 is the kinetic energy, the second term is the atomic core pseudopotential modeled using norm-conserving pseudopotentials, the third term is the electrostatic Hartree potential, while the fourth term is the exchange-correlation term, which is modeled using the local density approximation (LDA). The eigenvalue problem of the Hamiltonian is solved using the folded spectrum method (FSM),[52] as implemented in the PESCAN code that gives the electronic states around the desired energy, which is the top of the valence band in our case.

WAVE FUNCTIONS AT GRAIN BOUNDARIES

In this section, the wave functions of states at grain boundaries are presented. We consider the system consisting of 1000 molecules (500 at each side of the boundary) arranged in 10 layers that are parallel to the *ab* plane[47] of the unit cell. Electronic structure calculations are performed for a single layer of molecules, which is sufficient to describe the electronic properties of the material, because the electronic coupling in the *c* direction is much weaker than that in the *ab* plane. Calculations are performed for several misorientation angles between the grains: 5, 10, 15, and 20° and for two types of grain boundaries: (1) perpendicular to the *a* direction (*a*-boundary) and (2) perpendicular to the *b* direction (*b*-boundary) of the unit cell. Only small angles are considered, because the total energy of the system increases as the angle of misorientation increases, as demonstrated in Figure 2. For each system, the energies of the 10 highest occupied states in the valence band and their wave functions are calculated.

Results of electronic structure calculations for the *a*-boundary system with a misorientation angle of 10° are presented in Figure 3. These results indicate that there are several states in the band gap whose energies are significantly higher than the energies of the other states. These states are trap states for charge carriers and could strongly affect transport properties of the material. Wave functions of the first and the second highest occupied states are localized on the two molecules at the grain boundary. The distance between these two molecules (defined hereafter as the distance between their centers of mass) is 3.45 Å, while the distance between two nearest molecules in the monocrystal is about 5 Å. The highest occupied states in organic semiconductors originate from electronic coupling of the HOMO (highest occupied molecular orbital) levels of different molecules. Electronic coupling that results from the overlap of HOMO orbitals is strongest for closely spaced molecules. As a consequence, the highest state in Figure 3 is localized on two molecules with the smallest mutual distance. It is the bonding states of HOMO orbitals of the two molecules, whereas the second state in Figure 3 is the antibonding state. At certain energies, the spectrum becomes nearly continuous and the states that are completely delocalized start to appear, such as the 10th calculated state; see Figure 3. States like this originate from delocalized Bloch states of the monocrystal and, therefore, are not induced by grain boundaries.

Electronic calculations for other misorientation angles and boundary directions show similar results. In Figure 4, the results

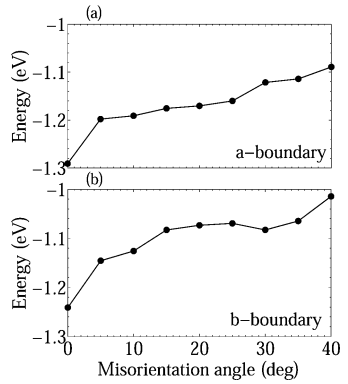

Figure 2. Dependence of potential energy of the system per molecule on the misorientation angle between monocrystal grains for *a*-boundary systems (a) and *b*-boundary systems (b). Each system consists of 1000 molecules.

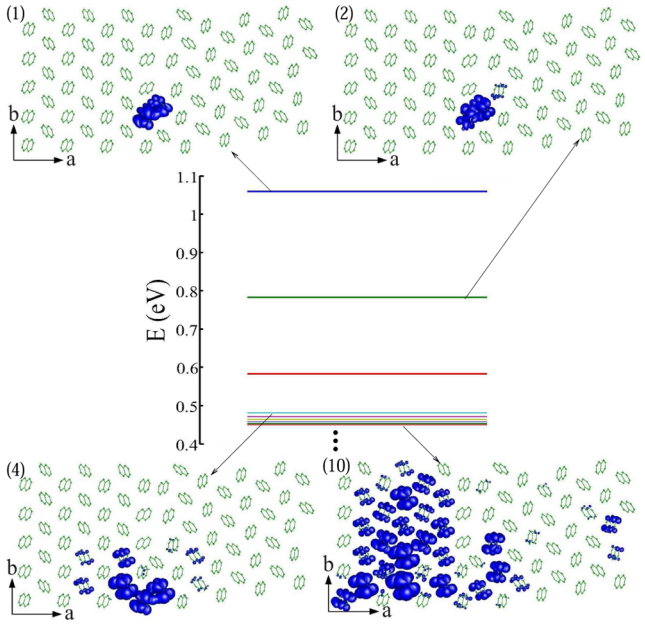

Figure 3. Energies of the states at the top of the valence band and the isosurfaces of their wave function moduli for the system with the misorientation angle of 10° and the grain boundary perpendicular to the *a* direction. Isosurfaces correspond to the probability of finding a hole inside the surface of 90%.

dx.doi.org/10.1021/jp404825h | J. Phys. Chem. C 2013, 117, 15741−15748

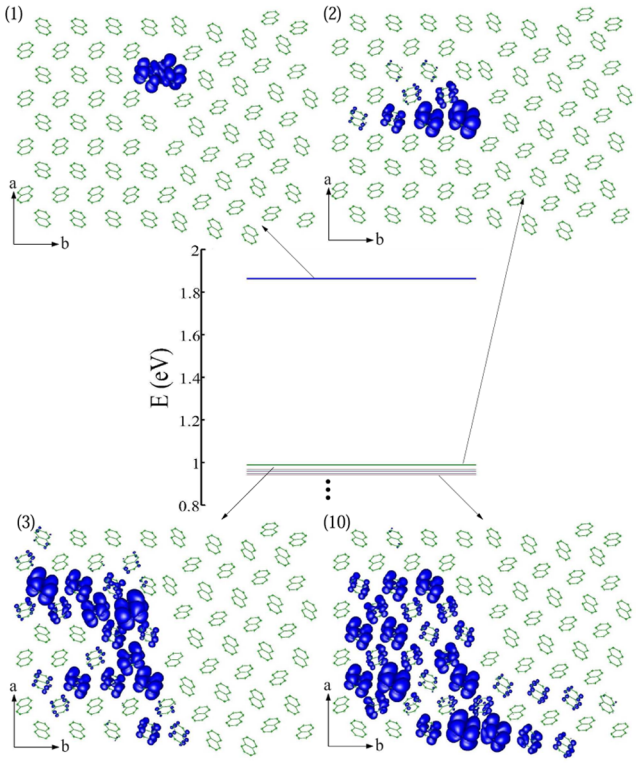

Figure 4. Energies of the states at the top of the valence band and the isosurfaces of their wave function moduli for the system with the misorientation angle of 10° and the grain boundary perpendicular to the *b* direction. Isosurfaces correspond to the probability of finding a hole inside the surface of 90%.

for the *b*-boundary system and the misorientation angle of 10° are presented. In this case, there is only one molecule pair at the grain boundary with a small mutual distance and, consequently, one trap state deep in the band gap. Other states are delocalized.

The presented results indicate that grain boundaries introduce electronic states within the band gap of the material. Hereafter, the states localized at the boundaries will be called trap states, whereas delocalized states will be called valence band states. Some trap states are very deep in the band gap, even more than 1 eV above the valence band. As a reference, the experimentally measured band gap of naphthalene is about 5.2 eV.[48] The traps with energies significantly above the top of the valence band (more than 0.1 eV) are always localized on two molecules belonging to different grains with a mutual distance less than the distance between two nearest molecules in the monocrystal. Such pairs of molecules will be hereafter called trapping pairs. Other localized states at the grain boundary have energies very close to the energies of the top of the valence band (second state in Figure 4, for example). Consequently, only pairs of molecules (trapping pairs) will be taken into account. We find that there is a strong correlation between the distance between the molecules in trapping pairs and the energy of the trap electronic states. This dependence is shown in Figure 5. The best fit of this dependence is given by an exponential function $\Delta E = Ae^{B(R-R_0)}$, where A = 1.4064 eV, B = −4.181 Å^{-1}, and R_0 = 3.2 Å.

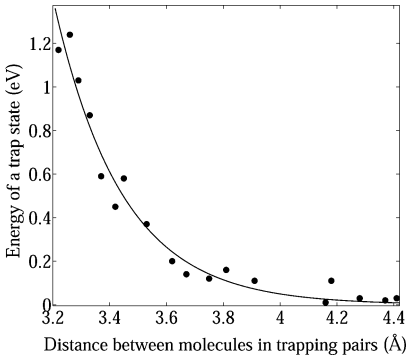

Figure 5. The dependence of the energy of the grain boundary induces trap states on the distance between molecules in trapping pairs. The data obtained from all simulated systems are presented in the figure. Energies of the trapping states are defined with the top of the valence band as a reference level.

DENSITY OF TRAP STATES AT GRAIN BOUNDARIES

Electronic structure calculations can be performed for relatively small boundaries only. Although such calculations were highly valuable for understanding the origin and the degree of wave function localization at the boundary, they do not provide sufficient statistics to reliably calculate the density of trap states. On the other hand, the remarkable dependence, presented in Figure 5, can be used to predict the energy of a trap at a given boundary without any electronic calculation, solely based on the distances between the molecules. This allows us to calculate the energies of all trap states for very large grain boundaries and, consequently, calculate the electronic density of trap states. On the basis of the degree of scattering of the data from the fit in Figure 5, we estimate that this method produces an error in the trap energy calculation of up to 0.1 eV.

Consequently, we have demonstrated that computationally demanding electronic structure calculations can be avoided using the aforementioned approach. Next, we show that even the MC relaxation step can be avoided without significantly compromising the accuracy of the electronic density of trap states. By inspecting the atomic structure near the boundaries in Figure 3, one can notice that it stays nearly unchanged after the relaxation. Only molecules in the vicinity of the boundary slightly change their positions and orientations. The difference in the distance between two molecules in trapping pairs, before and after the relaxation, is below 0.1 Å, as demonstrated in Figure 6. Consequently, both MC relaxation and electronic structure calculations can be avoided in the calculation of electronic density of trap states.

The electronic density of trap states was extracted from the calculations of grain boundaries that contain 100 000 molecules arranged in 100 layers. In the construction of the grain boundary atomic structure, there is an ambiguity related to the width of the void between the two monocrystals that form the boundary. This issue was overcome by shifting one of the crystals in the direction perpendicular to the boundary and selecting the void width in such a way that the potential energy of the system is minimal. The distribution of distances between trapping pairs of molecules is calculated then. Next, using the previously introduced exponential fitting function, the electronic density of trap states is obtained. The results are presented for four different angles: 5, 10, 15, and 20° and for two orientations of grain boundaries: *a*-boundary and *b*-

dx.doi.org/10.1021/jp404825h | J. Phys. Chem. C 2013, 117, 15741−15748

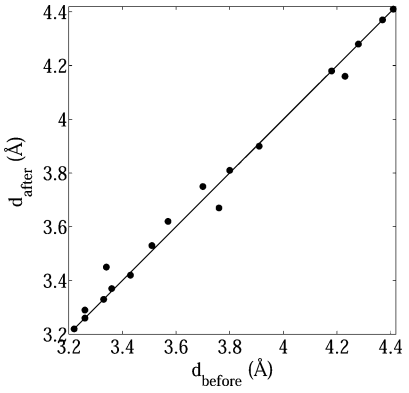

Figure 6. Dependence of the distance between trapping molecule pairs after MC relaxation (d_{after}) on the distance between them before MC relaxation (d_{before}).

boundary. As can be seen from Figure 5, trapping pairs with mutual distances below 4 Å are responsible for traps that are deep in the band gap. Other trapping pairs produce shallow traps that are close to the top of the valence band. The distribution of distances between molecules in trapping pairs at the grain boundaries is shown in Figure 7. One should note that

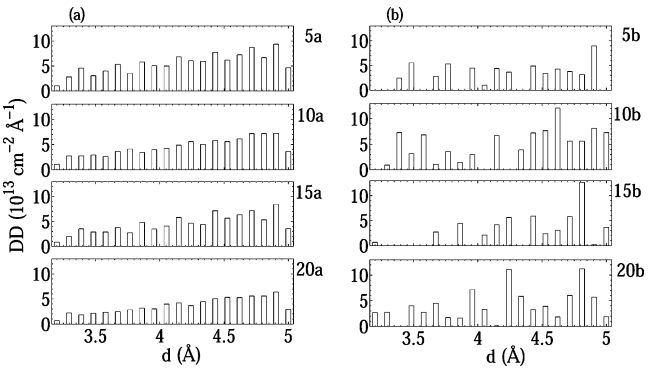

Figure 7. Trapping pair distance (d) distributions (DD) at different grain boundaries. The boundaries are denoted as Xy, where X is the angle between monocrystal grains and y is the direction perpendicular to the boundary surface.

molecule pairs with distances below 3.2 Å can also exist. However, these were not present in small systems calculated in the previous section; hence, their energy cannot be reliably calculated using the fitting function. Nevertheless, such states are rather rare and we neglect their surface density.

By inspecting Figure 7, one can notice that trapping pair distance distributions for *a*-boundary systems are similar for all angles. All of them are increasing functions with similar shapes. On the other hand, the distributions for *b*-boundary systems largely depend on misorientation angle. In addition, the distribution is not continuous as it is for *a*-boundary and some distances are preferred. This difference can be explained by the geometry of the naphthalene unit cell. Only *a* and *c* directions of the unit cell are not perpendicular. Therefore, the *c* direction is not parallel to the *a*-boundary surface. For this reason, in the case of *a*-boundary, different *ab* planes give different contributions to the trapping pair distance distribution. By adding the contribution from different *ab* planes, one obtains a continuous function. In the case of *b*-boundary, the *c* direction is parallel to the grain boundary surface. Consequently, molecule pairs from one *ab* plane have their copies in other *ab* planes and each *ab* plane gives the same contribution to trapping pair densities. This produces discrete trapping pair distance distributions. The difference between *a*- and *b*-boundary is illustrated in Figure 8, where spatial distribution of trapping pair distance is given. Each filled circle in Figure 8 represents a molecule in the layer at the grain boundary. The color of the circle indicates the distance between that molecule and the nearest molecule from the opposite side of the boundary. As one can notice, in the case of *a*-boundary, distributions for different *ab* planes are different (as evidenced by the nonperiodicity of the pattern shown in Figure 8a), whereas distributions for different *ab* planes in the case of *b*-boundary are equal (as evidenced by the periodic pattern in Figure 8b).

With trapping pair distance distributions at hand, the electronic density of trap states can be straightforwardly calculated as explained. Densities of trap states for eight aforementioned boundaries are given in Figure 9. Because the focus of this work is on trap states that are significantly above the top of the valence band, only trapping pairs with mutual distances below 4 Å are included in the distribution shown in Figure 9. In addition, we have assumed that each trapping pair introduces one trap state, although, in some cases, it can introduce two trap states, as demonstrated in Figure 3. For *a*-boundary systems, the density of trap states weakly depends on angle. Going deeper in the band gap, the density of trap states monotonously decreases, which is a consequence of the monotonously decreasing density of trapping pairs at the

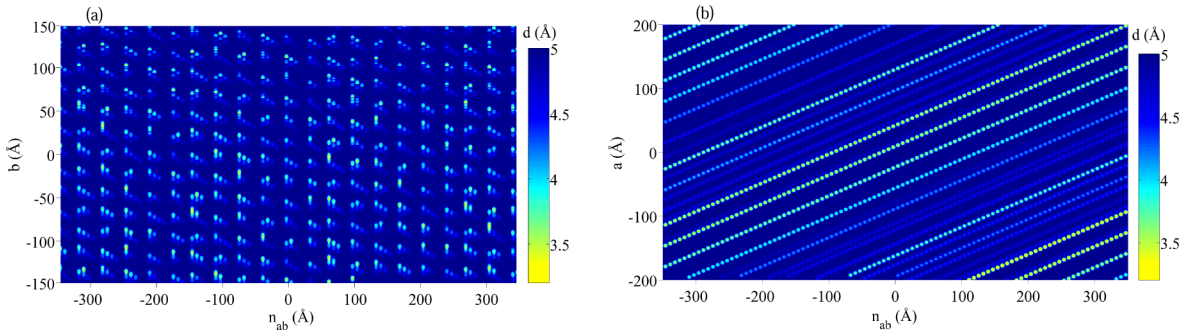

Figure 8. Spatial trapping pair distance distribution for *a*-boundary (a) and *b*-boundary (b) systems with the misorientation angle of 10°. The axis perpendicular to the *ab* plane is denoted as n_{ab}. Spatial trapping pair distance distribution is calculated using a radially symmetric weight function[53] calculated at the position of the molecular center of mass with a cutoff radius of 14.8 Å.

dx.doi.org/10.1021/jp404825h | J. Phys. Chem. C 2013, 117, 15741−15748

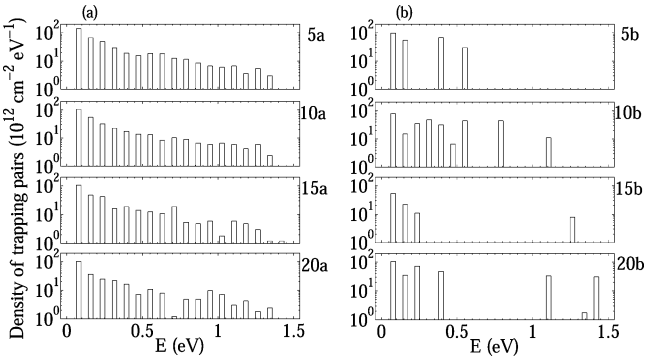

Figure 9. Electronic density of trap states at different grain boundaries. The boundaries are denoted as *Xy*, where *X* is the angle between monocrystal grains and *y* is the direction perpendicular to the boundary surface. Densities of trap states are given in a logarithmic scale. Energies of the trapping states are defined with the top of the valence band as a reference level.

grain boundary. For *b*-boundaries, the density of trap states is discrete with some distances preferred as a consequence of discrete density of trapping pairs at the grain boundary.

DISCUSSION

Our results clearly demonstrate the presence of trap states at the positions in the grain boundary where two molecules from opposite sides of the boundary are closely spaced, and hence, the electronic coupling of their HOMO orbitals is rather strong. In ref 23, it was argued that grain boundaries act as barriers for charge carriers rather than traps. Such an argument was drawn from an assumption that electronic coupling between molecules is weaker at the grain boundary than in the bulk. Our results show that such an assumption is not appropriate; strong electronic coupling at certain positions at the boundary creates trap states within the band gap of the material. However, one should also note that electronic coupling between neighboring molecules from opposite sides of the boundary can be weak at certain positions. At these positions, the grain boundary acts as a barrier and tends to confine the wave function to one side of the boundary. This effect can be seen from state (10) in Figure 3 and states (3) and (10) in Figure 4. Positions of strong electronic coupling and trap states will be absent only in the case of a grain boundary void when two grains with the same orientation are separated by empty space. Consequently, a void (microcrack) within an organic crystal[54] is expected to act as a barrier.

On the other hand, various numerical simulations of organic crystal FETs were based on a model that considers the transport at the boundary as a thermoionic jump over the barrier or tunneling through the barrier.[12,16,21,22] One should note that FETs typically operate at high charge densities. Therefore, the traps become filled with carriers, which, in turn, create an electrostatic potential that acts as a barrier for the transport of other charges. Such "trap charging induced barriers" should be distinguished from the barriers discussed in the previous paragraph.

Using the obtained results, the density of trap states for naphthalene polycrystals can be estimated. The calculated number of trap states per unit of boundary surface of two misoriented grains is 3×10^{13} cm^{-2} in the case of the misorientation angle of 5° and *a*-boundary, and takes similar values for other boundaries. Only trapping pairs with mutual distances below 4 Å were considered in the calculation. In the work of Chwang and Frisbie,[9] the density of trap states was estimated from activation energies for charge transport in a single grain boundary FET based on sexithiophene. It was found that trap densities at acceptor-like levels take values from 7.0×10^{11} to 2.1×10^{13} cm^{-2}, depending on the grain boundary length and the angle of misorientation. Therefore, our results are of the same order of magnitude as the experimentally based estimate for the material belonging to the same class of materials as naphthalene.

Next, we estimate the number of grain boundary induced trap states per unit of volume and compare it to other relevant material parameters. The typical size of experimentally evidenced monocrystal grains[8,9,20,55] is of the order of 1 μm, which translates into volume trap density of $N_t = 9 \times 10^{17}$ cm^{-3} assuming grains of a cubical shape. On the other hand, the number of energy states per unit of volume in the valence band of a bulk naphthalene monocrystal is $N_v = 6.1 \times 10^{21}$ cm^{-3}. Although N_t is much lower than N_v, it can still be significant to affect the charge transport and optical properties of naphthalene. In ref 55, grain boundary defects were identified as the most pronounced and the most stable defects. The density of point bulk defects was (over)estimated[55] to be in the $N_p = 10^{14}$–10^{16} cm^{-3} range. Because our calculated value of N_t is larger than N_p, our results confirm the conclusion that grain boundary defects are the most pronounced defects.[55] A compilation of the estimates of the density of trap states from FET characteristics was reported in ref 11. The estimated density of states at 0.2 eV above the valence band is in the range of $(0.7–3) \times 10^{19}$ cm^{-3} eV^{-1}, whereas at 0.3 eV above the valence band, it is in the $(1.5–4) \times 10^{18}$ cm^{-3} eV^{-1} range (see Figure 6 in ref 11). On the basis of these values, one can roughly estimate the density of trap states with energies higher than 0.2 eV above the valence band to be in the $(10^{17}–10^{18})$ cm^{-3} range, which is of the same order of magnitude as our calculated N_t.

Finally, we discuss the implications of our findings on properties of electronic and optoelectronic devices based on this class of materials. Since our results show that hole traps are located at the positions of strongest electronic coupling between orbitals of the two molecules from opposite sides of the boundary, one expects that there will be an electronic trap at the same position. We have verified this expectation by performing an explicit calculation of electron states at the boundary. As a consequence, traps at grain boundaries will not prevent radiative recombination of electrons and holes in LED devices or light absorption in the case of solar cells. Nevertheless, the traps will certainly broaden the absorption or emission spectrum of the material. Furthermore, the estimated number of traps per unit of volume is comparable to typical charge carrier densities in operating LED and solar cell devices. As a consequence, charge carrier transport will certainly be strongly affected by the traps. On the other hand, FETs typically operate at charge carrier densities much larger than the trap densities. As a consequence, the traps are filled with carriers and affect the charge carrier transport only through electrostatic barriers created by the trapped charges, as discussed previously.

CONCLUSIONS

In this paper, we have introduced the methodology for the calculation of electronic states at grain boundaries in small molecule based organic semiconductors. We focused our study

on low-angle grain boundaries, since our results indicated that they have lower energies than high-angle grain boundaries. The results indicate that grain boundaries introduce trap states within the band gap of the material. Wave functions of these states are localized on pairs of molecules from opposite sides of the boundary whose mutual distance is smaller than the distance between two adjacent molecules in a monocrystal. Strong electronic coupling between the orbitals of the two molecules is responsible for the creation of the trap state. While the naphthalene molecule was used in our study, we expect that the origin of trap states will be the same in any other small molecule based organic semiconductor since electronic coupling as a mechanism of trap state creation is present in any other material from this class.

The energy of the trap state was found to correlate to the distance between two molecules that create the trap. This correlation was then used to calculate the electronic density of trap states solely based on geometrical arrangement of molecules near the boundary. This approach was exploited to calculate the density of trap states for different boundaries and estimate the number of trap states per unit of volume in a real polycrystal. This number is significant and may consequently reduce the carrier mobility and deteriorate the performance of devices based on polycrystalline organic semiconductors.

AUTHOR INFORMATION

Corresponding Author

*E-mail: marko.mladenovic@ipb.ac.rs.

Notes

The authors declare no competing financial interest.

ACKNOWLEDGMENTS

This work was supported by a European Community FP7 Marie Curie Career Integration Grant (ELECTROMAT), the Serbian Ministry of Education, Science and Technological Development (Project ON171017), the Swiss National Science Foundation (SCOPES project IZ73Z0_128169), and FP7 projects (PRACE-2IP, PRACE-3IP, HP-SEE[S6] and EGI-InSPIRE).

REFERENCES

(1) Cheung, D. L.; Troisi, A. Modelling Charge Transport in Organic Semiconductors: From Quantum Dynamics to Soft Matter. *Phys. Chem. Chem. Phys.* **2008**, *10*, 5941−5952.

(2) Friend, R. H.; Gymer, R. W.; Holmes, A. B.; Burroughes, J. H.; Marks, R. N.; et al. Electroluminescence in Conjugated Polymers. *Nature* **1999**, *397*, 121−128.

(3) Burroughes, J. H.; Bradley, D. D. C.; Brown, A. R.; Marks, R. N.; Mackay, K.; Friend, R. H.; Burns, P. L.; Holmes, A. B. Light-Emitting Diodes Based on Conjugated Polymers. *Nature* **1990**, *347*, 539−541.

(4) Colvin, V. L.; Schlamp, M. C.; Alivisatos, A. P. Light-Emitting Diodes Made from Cadmium Selenide Nanocrystals and a Semiconducting Polymer. *Nature* **1994**, *370*, 354−357.

(5) Dodabalapur, A.; Torsi, L.; Katz, H. E. Organic Transistors: Two-Dimensional Transport and Improved Electrical Characeristics. *Science* **1995**, *268*, 270−271.

(6) Li, G.; Shrotriya, V.; Huang, J. S.; Yao, Y.; Moriarty, T.; Emery, K.; Yang, Y. High-Efficiency Solution Processable Polymer Photovoltaic Cells by Self-Organization of Polymer Blends. *Nat. Mater.* **2005**, *4*, 864.

(7) Fu, Y.-T.; Risko, C.; Bredás, J.-L. Intermixing at the Pentacene-Fullerene Bilayer Interface: A Molecular Dynamics Study. *Adv. Mater.* **2013**, *25*, 878−882.

(8) Kalihari, V.; Tadmor, E. B.; Haugstad, G.; Frisbie, C. D. Grain Orientation Mapping of Polycrystalline Organic Semiconductor Films by Transverse Shear Microscopy. *Adv. Mater.* **2008**, *20*, 4033−4039.

(9) Chwang, A. B.; Frisbie, C. D. Temperature and Gate Voltage Dependent Transport Across a Single Organic Semiconductor Grain Boundary. *J. Appl. Phys.* **2001**, *90*, 1342−1349.

(10) Chapman, B.; Checco, A.; Pindak, R.; Siegrist, T.; Kloc, C. Dislocations and Grain Boundaries in Semiconducting Rubrene Single-Crystals. *J. Cryst. Growth* **2006**, *290*, 479−484.

(11) Kalb, W. L.; Haas, S.; Krellner, C.; Mathis, T.; Batlogg, B. Trap Density of States in Small-Molecule Organic Semiconductors: A Quantitative Comparison of Thin-Film Transistors with Single Crystals. *Phys. Rev. B* **2010**, *81*, 155315.

(12) Horowitz, G.; Hajlaoui, M. E. Mobility in Polycrystalline Oligothiophene Field-Effect Transistors Dependent on Grain Size. *Adv. Mater.* **2000**, *12*, 1046−1050.

(13) Nelson, S. F.; Lin, Y.-Y.; Gundlach, D. J.; Jackson, T. N. Temperature-Independent Transport in High-Mobility Pentacene Transistors. *Appl. Phys. Lett.* **1998**, *72*, 1854−1856.

(14) Sakanoue, T.; Sirringhaus, H. Band-like Temperature Dependence of Mobility in a Solution-Processed Organic Semiconductor. *Nat. Mater.* **2010**, *9*, 736−740.

(15) Lee, S. S.; Kim, C. S.; Gomez, E. D.; Purushothaman, B.; Toney, M. F.; Wang, C.; Hexemer, A.; Anthony, J. E.; Loo, Y.-L. Controlling Nucleation and Crystallization in Solution-Processed Organic Semiconductors for Thin-Film Transistors. *Adv. Mater.* **2009**, *21*, 3605−3609.

(16) Chen, J.; Tee, C. K.; Shtein, M.; Anthony, J.; Martin, D. C. Grain-Boundary-Limited Charge Transport in Solution-Processed 6,13Bis(tri-isopropylsilylethynyl) Pentacene Thin Film Transistors. *J. Appl. Phys.* **2008**, *103*, 114513.

(17) Gundlach, D. J.; Royer, J. E.; Park, S. K.; Subramanian, S.; Jurchescu, O. D. Contact-Induced Crystallinity for High-Performance Soluble Acene-Based Transistors and Circuits. *Nat. Mater.* **2008**, *7*, 216−221.

(18) Rivnay, J.; Jimison, L. H.; Northrup, J. E.; Toney, M. F.; Noriega, R.; Lu, S.; Marks, T. J.; Facchetti, A.; Salleo, A. Large Modulation of Carrier Transport by Grain-Boundary Molecular Packing and Microstructure in Organic Thin Films. *Nat. Mater.* **2009**, *8*, 952−958.

(19) Dickey, K.; Anthony, J.; Loo, Y.-L. Improving Organic Thin-Film Transistor Performance through Solvent-Vapor Annealing of Solution-Processable Triethylsilylethynyl Anthradithiophene. *Adv. Mater.* **1976**, *21*, 392.

(20) Carlo, A. D.; Piacenza, F.; Bolognesi, A.; Stadlober, B.; Maresch, H. Influence of Grain Sizes on the Mobility of Organic Thin-Film Transistors. *Appl. Phys. Lett.* **2005**, *86*, 263501.

(21) Verlaak, S.; Arkhipov, V.; Heremans, P. Modeling of Transport in Polycrystalline Organic Semiconductor Films. *Appl. Phys. Lett.* **2003**, *82*, 745−747.

(22) Horowitz, G. Tunneling Current in Polycrystalline Organic Thin-Film Transistors. *Adv. Funct. Mater.* **2003**, *13*, 53−60.

(23) Kaake, L. G.; Barbara, P. F.; Zhu, X.-Y. Intrinsic Charge Trapping in Organic and Polymeric Semiconductors: A Physical Chemistry Perspective. *J. Phys. Chem. Lett.* **2010**, *1*, 628−635.

(24) Nan, G.; Li, Z. Modeling of Charge Transport in Polycrystalline Sexithiophene From Quantum Charge Transfer Rate Theory Beyond the First-Order Perturbation. *Org. Electron.* **2011**, *12*, 2198−2206.

(25) Verlaak, S.; Heremans, P. Molecular Micromolecular View on Electronic States Near Pentacene Grain Boundaries. *Phys. Rev. B* **2007**, *75*, 115127.

(26) Troisi, A.; Orlandi, G. Charge-Transport Regime of Crystalline Organic Semiconductors: Diffusion Limited by Thermal Off-Diagonal Electronic Disorder. *Phys. Rev. Lett.* **2006**, *96*, 086601.

(27) Nan, G.; Yang, X.; Wang, L.; Shuai, Z.; Zhao, Y. Nuclear Tunneling Effects of Charge Transport in Rubrene, Tetracene, and Pentacene. *Phys. Rev. B* **2009**, *79*, 115203.

(28) Shuai, Z.; Wang, L.; Li, Q. Evaluation of Charge Mobility in Organic Materials: From Localized to Delocalized Descriptions at a First-Principles Level. *Adv. Mater.* **2011**, *23*, 1145−1153.
(29) Sánchez-Carrera, R. S.; Atahan, S.; Schrier, J.; Aspuru-Guzik, A. Theoretical Characterization of the Air-Stable, High-Mobility Dinaphtho[2,3-b:2′ 3′-*f*]thieno[3,2-b]-thiophene Organic Semiconductor. *J. Phys. Chem. C* **2010**, *114*, 2334−2340.
(30) Hannewald, K.; Stojanović, V. M.; Schellekens, J. M. T.; Bobbert, P. A.; Kresse, G.; Hafner, J. Theory of Polaron Bandwidth Narrowing in Organic Molecular Crystals. *Phys. Rev. B* **2004**, *69*, 075211.
(31) Ortmann, F.; Bechstedt, F.; Hannewald, K. Theory of Charge Transport in Organic Crystals: Beyond Holstein's Small-Polaron Model. *Phys. Rev. B* **2009**, *79*, 235206.
(32) Martinelli, N. G.; Olivier, Y.; Athanasopoulos, S.; Delgado, M. C. R.; Pigg, K. R.; et al. Influence of Intermolecular Vibrations on the Electronic Coupling in Organic Semiconductors: The Case of Anthracene and Perfluoropentacene. *ChemPhysChem* **2009**, *10*, 2265−2273.
(33) Ciuchi, S.; Fratini, S. Electronic Transport and Quantum Localization Effects in Organic Semiconductors. *Phys. Rev. B* **2012**, *86*, 245201.
(34) Ciuchi, S.; Fratini, S.; Mayou, D. Transient Localization in Crystalline Organic Semiconductors. *Phys. Rev. B* **2011**, *83*, 081202.
(35) Ciuchi, S.; Fratini, S. Band Dispersion and Electronic Lifetimes in Crystalline Organic Semiconductors. *Phys. Rev. Lett.* **2011**, *106*, 166403.
(36) Perroni, C. A.; Marigliano Ramaglia, V.; Cataudella, V. Effects of Electron Coupling to Intramolecular and Intermolecular Vibrational Modes on the Transport Properties of Single-Crystal Organic Semiconductors. *Phys. Rev. B* **2011**, *84*, 014303.
(37) Vukmirović, N.; Bruder, C.; Stojanović, V. M. Electron-Phonon Coupling in Crystalline Organic Semiconductors: Microscopic Evidence for Nonpolaronic Charge Carriers. *Phys. Rev. Lett.* **2012**, *109*, 126407.
(38) Allen, M.; Tildesley, D. J. *Computer Simulation of Liquids*; Oxford University Press: New York, 1987.
(39) Parr, R. G.; Yang, W. *Density-Functional Theory of Atoms and Molecules*; Oxford University Press: New York, 1989.
(40) Vukmirović, N.; Wang, L. W. Charge Patching Method for Electronic Structure of Organic Systems. *J. Chem. Phys.* **2008**, *128*, 121102.
(41) Vukmirović, N.; Wang, L. W. Electronic Structure of Disordered Conjugated Polymers: Polythiophenes. *J. Phys. Chem. B* **2009**, *113*, 409−415.
(42) Martin, M. G.; Siepmann, J. I. Transferable Potentials for Phase Equilibria. 1. United-Atom Description of *n*-Alkanes. *J. Phys. Chem. B* **1998**, *102*, 2569−2577.
(43) Wick, C. D.; Martin, M. G.; Siepmann, J. I. Transferable Potentials for Phase Equilibria. 4. United-Atom Description of Linear and Branched Alkenes and Alkylbenzenes. *J. Phys Chem. B* **2000**, *104*, 8008−8016.
(44) Rai, N.; Bhatt, D.; Siepmann, J. I.; Fried, L. E. Monte Carlo Simulations of 1,3,5-Triamino-2,4,6-trinitrobenzene (TATB): Pressure and Temperature Effects for the Solid Phase and Vapor-Liquid Phase Equilibria. *J. Chem. Phys.* **2008**, *129*, 194510.
(45) Rai, N.; Siepmann, J. I. Transferable Potentials for Phase Equilibria. 10. Explicit-Hydrogen Description of Substituted Benzenes and Polycyclic Aromatic Compounds. *J. Phys. Chem. B* **2013**, *117*, 273−288.
(46) Sánchez-Carrera, R. S.; Paramonov, P.; Day, G. M.; Coropceanu, V.; Bredás, J.-L. Interaction of Charge Carriers with Lattice Vibrations in Oligoacene Crystals from Naphthalene to Pentacene. *J. Am. Chem. Soc.* **2010**, *132*, 14437−14446.
(47) Schwoerer, M.; Wolf, H. C. *Organic Molecular Solids*; WILEY-VCH Verlag: Wienheim, Germany, 2008.
(48) Hummer, K.; Ambrosch-Draxl, C. Electronic Properties of Oligoacenes from First Principles. *Phys. Rev. B* **2005**, *72*, 205205.
(49) Ponomarev, V. I.; Filipenko, O. S.; Atovmyan, L. O. Improving Organic Thin-Film Transistor Performance through Solvent-Vapor Annealing of Solution-Processable Triethylsilylethynyl Anthradithiophene. *Kristallografiya* **1976**, *21*, 392.
(50) Schmidt, M.; Kusche, R.; Kronmüller, W.; von Issendorff, B.; Haberland, H. Experimental Determination of the Melting Point and Heat Capacity for a Free Cluster of 139 Sodium Atoms. *Phys. Rev. Lett.* **1997**, *79*, 99−102.
(51) Lee, J. A.; Rösner, H.; Corrigan, J. F.; Huang, Y. Phase Transitions of Naphthalene and Its Derivatives Confined in Mesoporous Silicas. *J. Phys. Chem. C* **2011**, *115*, 4738−4748.
(52) Canning, A.; Wang, L. W.; Williamson, A.; Zunger, A. Parallel Empirical Pseudopotential Electronic Structure Calculations for Million Atom Systems. *J. Comput. Phys.* **2000**, *160*, 29−41.
(53) Stankovic, I.; Hess, S.; Kröger, M. Structural Changes and Viscoplastic Behavior of a Generic Embedded-Atom Model Metal in Steady Shear Flow. *Phys. Rev. E* **2004**, *69*, 021509.
(54) Chen, J.; Tee, C. K.; Yang, J.; Shaw, C.; Shtein, M.; Anthony, J.; Martin, D. C. Thermal and Mechanical Cracking in Bis(triisopropylsilylethnyl) Pentacene Thin Films. *J. Polym. Sci., Part B: Polym. Phys.* **2006**, *44*, 3631−3641.
(55) Verlaak, S.; Rolin, C.; Heremans, P. Microscopic Description of Elementary Growth Processes and Classification of Structural Defects in Pentacene Thin Films. *J. Phys. Chem. B* **2007**, *111*, 139−150.
(56) This work makes use of results produced by the High-Performance Computing Infrastructure for South East Europe's Research Communities (HP-SEE), a project co-funded by the European Commission (under contract number 261499) through the Seventh Framework Programme. HP-SEE involves and addresses specific needs of a number of new multi-disciplinary international scientific communities and thus stimulates the use and expansion of the emerging new regional HPC infrastructure and its services. Full information is available at: http://www.hp-see.eu/.

PCCP

PAPER

Effects of thermal disorder on the electronic properties of ordered polymers

Marko Mladenović[ab] and Nenad Vukmirović*[a]

Cite this: *Phys. Chem. Chem. Phys.*, 2014, **16**, 25950

Received 30th September 2014,
Accepted 23rd October 2014

DOI: 10.1039/c4cp04425h

www.rsc.org/pccp

The effects of thermal disorder on the electronic properties of crystalline polymers were investigated. Atomic configurations of the material were obtained using classical Monte Carlo simulations at room temperature, while electronic structure calculations were performed using the density functional theory based charge patching method and the overlapping fragment method. We investigated two different stable configurations of crystalline poly(3-hexylthiophene) (P3HT) and calculated the density of electronic states and the wave function localisation. We found that the effect of disorder in side chains is more pronounced in the more stable configuration of P3HT than in the other one due to the larger conformational freedom of side chains. The results show that disorder in main chains has a strong effect on the electronic structure and leads to the localisation of the wave functions of the highest states in the valence band, similar to localisation that occurs in amorphous polymers. The presence of such states is one possible origin of thermally activated electrical transport in ordered polymers at room temperature.

1 Introduction

Materials based on conjugated polymers attract a lot of interest due to their applications in electronic devices such as organic field-effect transistors, organic light-emitting diodes and organic solar cells.[1–5] These materials contain both crystalline and amorphous regions and consequently their electronic properties strongly depend on their morphology. In crystalline regions of the material, thiophene rings are connected into main (backbone) polymer chains, which then form two dimensional lamellar structures separated by insulating side chains.

Crystalline polymer regions exhibit better transport characteristics than amorphous regions. At first, one may expect that the electronic states in crystalline regions are fully delocalised due to the effect of periodicity. On the other hand, wave functions of electronic states in amorphous regions are well localised due to the effects of disorder. Calculations of the electronic structure of amorphous polymers show that wave functions of the highest states in the valence band are localised on few rings only.[6,7] The electronic states in crystalline regions may also exhibit localisation due to the effects of thermal disorder; at finite temperature the atoms are displaced from their equilibrium positions in a random manner and the atomic positions no longer exhibit periodicity. The importance of the effects of thermal (or dynamic, which is an alternative expression often used in the literature) disorder in small molecule based organic crystals is now widely recognized.[8–14] On the other hand, the effects of thermal disorder in polymers are less well understood. Currently available simulation results[15–17] suggest that the highest valence band states in ordered polymer materials at room temperature are localised. However, most of these calculations either consider a single polymer chain or do not include the effects of side chains.

The aim of this work is to investigate in detail the effects of thermal disorder on the electronic properties of ordered polymer materials and to identify relative importance of various sources of thermal disorder. For concreteness, we choose the poly(3-hexylthiophene) (P3HT) polymer for our study. We calculate the electronic density of states (DOS) and the localisation of hole wave functions. Atomic configurations at finite temperature are obtained using Monte Carlo (MC)[18] simulations, while the charge patching method (CPM)[6,7,19,20] and the overlapping fragment method (OFM)[7,21] are used for electronic structure calculations.

The disorder in the structure at finite temperature comes both from the disorder in the shape of the flexible alkyl side chains (that will be referred to as side chain disorder from now on) and from the disorder due to variations of torsion angles between thiophene rings in the main chains and the position of main chains (that will be referred to as main chain disorder from now on).[22] One should note that disorder of main or side chains does not imply an amorphous material. While it is well known that the wave functions in conjugated polymers are localised on the main chain, side chains with a disordered

[a] *Scientific Computing Laboratory, Institute of Physics Belgrade, University of Belgrade, Pregrevica 118, 11080 Belgrade, Serbia. E-mail: nenad.vukmirovic@ipb.ac.rs*

[b] *School of Electrical Engineering, University of Belgrade, P.O. Box 35-54, 11120 Belgrade, Serbia*

shape still affect the electronic structure as they create a disordered electrostatic potential on the main chain. Disorder in the shape of the main chain mostly affects the electronic structure through variations in electronic coupling between the rings. To isolate the effects of main and side chain disorders we investigate three types of structures: (1) the structures with straight main chains and disordered alkyl side chains; (2) the structures with disordered main chains in the absence of side chains; (3) the structures with both main and side chains disordered.

We find that the effects of disorder are least pronounced in the structures with disordered side chains. Strong wave function localisation of highest valence band states occurs in structures with main chains disordered, both with and without side chains. Such a localisation is one possible origin of thermally activated transport observed in all reported P3HT mobility measurements.

2 Methods for atomic and electronic structure calculations

The method used for electronic structure calculations is schematically described in Fig. 1. The atomic structure is obtained using in-house developed code for MC simulations. It is subsequently used to calculate the electronic structure, using the CPM and the OFM.

2.1 Lattice constants

The initial structure for MC simulations is the ideal crystalline structure of P3HT. The atomic structure of crystalline P3HT was extensively studied and different possible configurations were found.[23–32] Two different stable crystalline structures are simulated at 300 K: aligned and shifted, which are shown in Fig. 2. In the aligned structure, thiophene rings from two adjacent main chains in the π–π stacking direction are aligned. On the other hand, in the shifted structure, thiophene rings from two

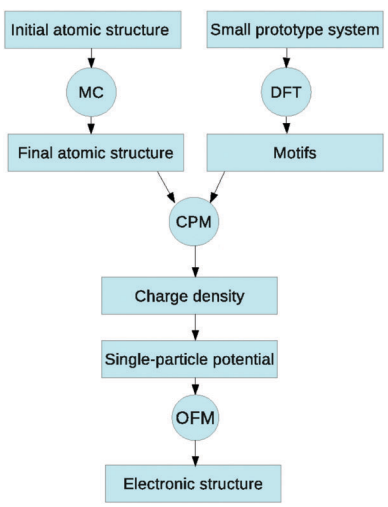

Fig. 1 Schematic representation of the algorithm for the electronic structure calculations.

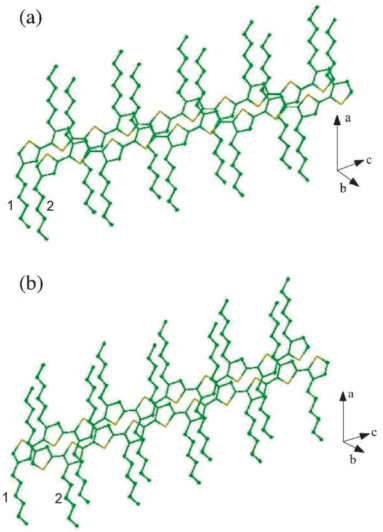

Fig. 2 Two stable configurations of crystalline P3HT: (a) aligned and (b) shifted. The main chain direction is denoted by *c*, the π–π stacking direction by *b* and the side chain direction by *a*.

adjacent chains in the π–π stacking direction are mutually shifted by the half of the unit cell in the main chain direction. Parameters of the unit cells are found using NPT (constant pressure and temperature) MC simulation at 300 K and 101.325 kPa. During the simulation, the size of the box in the main chain direction is kept constant, while two other dimensions are changed. The energy of the system is modelled as a sum of the long-range (van der Waals and Coulomb) interactions between atoms from different chains. Expression and parameters for the long-range interactions are taken from the OPLS parameters set,[33] which was previously successfully applied for the simulations of the same material.[15] Cutoff for these interactions is taken to be 12 Å. The unit cell parameters are determined as the parameters obtained when the system reaches thermal equilibrium. For the aligned structure these are: $a/2$ = 15.7 Å, b = 8.2 Å and c = 7.77 Å, while for the shifted structure these are: $a/2$ = 15.7 Å, b = 8.1 Å and c = 7.77 Å. All unit cell angles are taken to be 90°. These parameters are in very good agreement with previous computational results for the same structures of P3HT. For example, the unit cell parameters obtained for the aligned structure in ref. 24 are: $a/2$ = 16 Å, b = 8.2 Å and c = 7.81 Å, while for the shifted these are: $a/2$ = 16 Å, b = 7.85 Å and c = 7.81 Å. On the other hand, experimental results based on the X-ray diffraction measurements suggest somewhat higher value for the side chain stacking direction of 16.8 Å.[29] This difference might originate from the assumption of the ideal crystal structure without disorder made in the calculations, which is not the case in reality. Interdigitation between side chains from different lamellas is weaker in more disordered structures, and consequently, the unit cell parameter for the side chain stacking direction is higher. We find that the shifted structure is more stable at 300 K, since its potential energy per number of rings is 0.38 eV lower than the corresponding energy in the aligned structure, confirming the

results given in ref. 24 that the shifted structure is more energetically favourable.

2.2 Atomic structure

With the initial structure at hand, MC simulations are performed to obtain the snapshots of the atomic structure at room temperature. During the MC simulations bond lengths and bond angles are kept constant, while some or all torsion angles are changed. Variations of torsion angles affect electronic coupling between orbitals more strongly than variations of bond lengths and bond angles. For example, the thermal energy at room temperature $k_BT = 25$ meV leads to displacement of an atom due to bond stretching on the order of 0.02 Å, while the same energy leads to interring torsion angle change on the order of 45°, which yields the atomic displacements of more than 1 Å. For this reason, it is reasonable to keep bond angles and bond lengths constant. In each step of the MC simulation a new configuration is generated by changing the torsion angles and moving the whole polymer chain. The new configuration is accepted if it satisfies the Metropolis condition.[18] The energy of the system is calculated as a sum of torsion potentials and long range van der Waals and Coulomb interactions. Thiophene–thiophene torsion potential is taken from ref. 6, while thiophene-side chain torsion potential is taken from ref. 24. Long-range interactions are modelled in the same way as for lattice constants calculations. An OPLS parameter set is also used for the torsion potentials within side chains. Periodic boundary conditions are applied in each direction of the unit cell for the systems with disorder in side chains. Boundary conditions are open in the main chain direction for the systems with disorder in main chains. The final atomic structure is taken after the system is thermally equilibrated at 300 K, which is evidenced from the saturation in the dependence of potential energy on the number of MC steps.

2.3 Electronic structure

The final atomic configuration obtained from MC simulations is used as input for electronic structure calculations. For the system containing more than thousand atoms density functional theory (DFT) calculations would be too computationally demanding. Therefore, the CPM is applied instead of DFT. The main idea of the CPM is to calculate the electronic charge density directly, instead of obtaining it from self-consistent solving of Kohn–Sham DFT equations. The charge density is calculated as a sum of contributions (called motifs) of all atoms in the system. Motifs are extracted from the DFT calculations of a small prototype system containing 3 neighbouring rings of P3HT and they are the same as used in ref. 6. The CPM was previously applied to calculate the electronic structure of amorphous P3HT.[6,7] The details of the CPM are presented in ref. 19.

When electronic charge density is obtained, the single-particle Kohn–Sham Hamiltonian is constructed by solving the Poisson equation for the Hartree potential and using the local density approximation (LDA) for the exchange–correlation potential.[34] The single particle Hamiltonian is then diagonalized using the OFM. This method uses the eigenstates of small fragments of the system as the basis set. In this case, fragments are systems of 3 neighbouring rings of P3HT (trimers). In previous work we demonstrated that a good basis set is obtained when the fragments mutually overlap.[7] To calculate the electronic states in the desired spectral region (within 0.5 eV below the top of the valence band) with good accuracy, only one eigenstate (the HOMO state) of each fragment is needed. When the basis set is obtained, transfer and overlap integrals between basis states are calculated and subsequently, the Hamiltonian generalized eigenvalue problem is solved. These calculations can be done using parallel computer architectures, which saves a lot of computational time. A detailed description of the OFM can be found in ref. 21.

In this work, the effect of polarons was not included. Previous DFT calculations of long straight polythiophene chains at zero temperature indicate that polaron binding energy is on the order of few meVs only and that it can be ignored.[35,36] However, it is more difficult to assess the role of polarons at finite temperature when thermal disorder is present in the material. Since the main goal of this work is to understand the effect of thermal disorder on wave function localisation and DOS, as well as the contributions from main and side chains to thermal disorder, polaronic effects were not considered.

Next, we discuss the appropriateness of LDA for the description of the localisation effects. The localisation effects that we observe essentially come from two effects: (i) variations of on-site energies of rings; (ii) variations in electronic coupling between the rings. Effect (i) comes mainly from disordered long range electrostatic potential that side chains, the rest of the main chain and other main chains produce on a certain ring. Within DFT, electrostatic potential is taken into account through the Hartree term in the Kohn–Sham equation, which is an exact term. Therefore, for effect (i), the use of LDA in our calculation is not an issue. To check if LDA gives reliable values of electronic coupling (effect (ii)), we have performed the calculation of electronic energy levels of a ten unit long straight thiophene oligomer using either the LDA or B3LYP functional for the same atomic configuration. These calculations have been performed using the NWChem code[37,38] and the 6-31G basis set was used to represent the wave functions. We find that the spacing between energy levels calculated using these two functionals differs typically by 15%. Since the spacing between energy levels of straight oligomers is proportional to electronic coupling between the rings, we conclude that possible uncertainties in electronic coupling calculated using LDA are on the order of 10–20% and such uncertainties are not expected to significantly affect the localisation lengths.

3 Results and discussion

The effects of thermal disorder in crystalline P3HT are investigated by examining 3 different types of structures: the structures with disorder in side chains, the structures with disorder in main chains and the structures with disorder in both side and main chains. In the first case, main chains are kept rigid during the MC simulation, while side chains are allowed to

move freely. In the second case, side chains are removed (more precisely, replaced with a hydrogen atom) before the electronic structure calculations start, in order to isolate the effects of main chain disorder. In the case of structures with the presence of disorder in both main and side chains, the same atomic configurations are used as for the second case, but side chains are not removed in this case. To get sufficiently large statistics, for each of the investigated cases and for both aligned and shifted structures, 100 different realizations are generated. Each configuration contains 10 polymer chains stacked in the π–π direction, while each chain contains 10 rings. The total number of atoms in each configuration is 2520. For subsequent analysis only 10 highest states from each configuration are taken into account, since they cover a spectral range of about 0.5 eV below the HOMO level, which is the range of interest for the electrical transport properties. To analyse the effects of disorder, we calculate the DOS and the localisation length of hole states.

3.1 Density of electronic states

Densities of states obtained from the calculations are shown in Fig. 3. In the case of disorder in side chains in the aligned structure, DOS is nearly discrete, composed of several peaks (Fig. 3a). These peaks correspond to the peaks in the DOS of the ideal crystalline structure without any disorder. In the shifted structure, peaks are broader and overlap more than in the aligned structure, making DOS continuous (Fig. 3b). Thus, the effects of side chain disorder on DOS are more pronounced in the shifted structure than in the aligned. The difference in DOS for shifted and aligned structures can be explained by the difference in the spatial distribution of side chains in these two structures. In the aligned structure, side chains connected to the aligned thiophene rings from neighbouring chains in the π–π direction are at the same side of the main chains (chains denoted by 1 and 2 in Fig. 2a). On the other hand, in the shifted structure these side chains are at the opposite sides. The distance between nearest side chains in the shifted structure (chains denoted by 1 and 2 in Fig. 2b) is greater than in the aligned. Therefore, side chains in the shifted structure have more conformational freedom than in the aligned. This is evidenced by the distributions of the thiophene-side chain torsion angle for both structures, given in Fig. 4a and b. The distribution of thiophene-side chain torsion angles is significantly wider in the shifted structure, which results in a higher degree of side chain disorder. This difference in morphology leads to the difference in the electronic structure.

In the structures with disordered main chains, DOS is continuous (Fig. 3c and d). In the case of aligned structures, distribution of energies is significantly wider than in the shifted structure. Distributions of thiophene–thiophene torsion angles for the aligned and shifted structures are similar (Fig. 4c and d) and agree well with the results of ref. 16. Therefore, the difference in the distribution of the energies is not caused by the shape of the chains. Electronic coupling between different chains is 0.11 eV in the ideal aligned structure and 0.07 eV in the ideal shifted structure. This substantial difference leads to the wider distribution of the energies in the aligned structure. When both main and side chains are disordered, the DOS is continuous (Fig. 3e and f) without any apparent difference between structures. This similarity in DOS can be explained by the effect of compensation between wider energy distribution in the shifted structure when only side chains are disordered and wider energy distribution in the aligned structure when only main chains are disordered.

A suitable measure of disorder in the system is the distribution of diagonal Hamiltonian elements given by $H_{ii} = \langle i|H|i\rangle$, where $|i\rangle$ are wave functions of trimers and H is the Hamiltonian of the system. Wave functions of the trimers are localised on the main chain and on the carbon atoms in the side chains closest to the thiophene rings. Consequently, if main chains of trimers are rigid, their wave functions and energies of HOMO levels will be equal. When only disorder in side chains is applied, the difference between diagonal Hamiltonian elements arises only

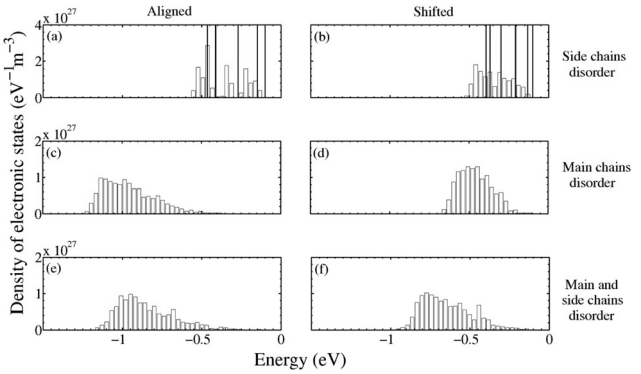

Fig. 3 DOS in the case of: (a) aligned structure with disorder in the side chains (bins) and ideal crystalline aligned structure (vertical lines); (b) shifted structure with disorder in the side chains (bins) and ideal crystalline aligned structure (vertical lines); (c) aligned structure with disorder in main chains and side chains omitted; (d) shifted structure with disorder in main chains and side chains omitted; (e) aligned structure with disorder in both side and main chains (f) shifted structure with disorder in both side and main chains.

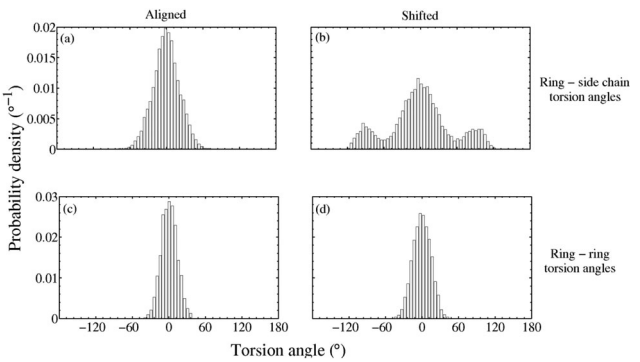

Fig. 4 Distribution of the (a) thiophene-side chain torsion angles in the aligned structure; (b) thiophene-side chain torsion angles in the shifted structure; (c) thiophene–thiophene torsion angles in the aligned structure; (d) thiophene–thiophene torsion angles in the shifted structure. In panels (c) and (d) the angles are shifted by 180° for clarity. To exclude the effects of finite box dimensions in the main chain direction, in (c) and (d) only torsion angles between rings in the middle of the chains are taken into account.

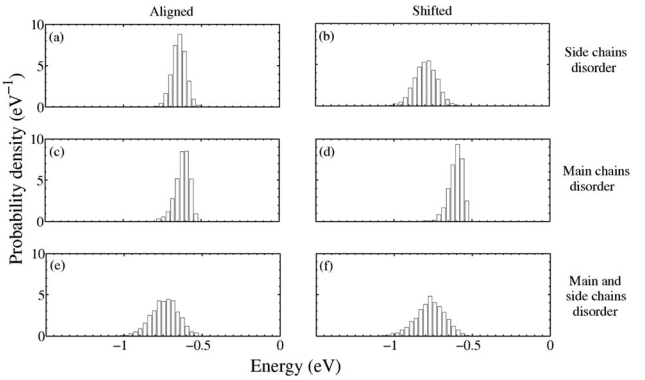

Fig. 5 Distribution of the diagonal elements of the Hamiltonian in: (a) aligned structure with disorder in side chains; (b) shifted structure with disorder in side chains; (c) aligned structure with disorder in main chains and side chains omitted; (d) shifted structure with disorder in main chains and side chains omitted; (e) aligned structure with disorder in both main and side chains and (f) shifted structure with disorder in both main and side chains. To exclude the effects of finite box dimensions in the main chain direction, in (c), (d), (e) and (f) only trimers in the middle of the chains are taken into account.

from variations in H, due to the variations in the electrostatic potential caused by side chain disorder. On the other hand, when disorder in main chains is present, variations in H_{ii} arises both from H and $|i\rangle$, since wave functions of trimers now differ significantly. Distributions of diagonal elements of the Hamiltonian are given in Fig. 5. As expected, distributions are widest in the case when both disorders are present (Fig. 5e and f). Having in mind the results for DOS presented above, which suggest that disorder in main chains has more impact on the electronic structure of P3HT than disorder in side chains, one may find unexpected that distributions given in Fig. 5c and d are similar to the distributions given in Fig. 5a and b. Side chains have more conformational freedom than main chains, especially in the shifted structure. Therefore, their disorder affects the electrostatic potential more than disorder in main chains. When effects of disorder in main chains are isolated, side chains are removed and, consequently, variations of electrostatic potential are weaker than in the case of disorder in side chains, which leads to the weaker variations in H.

3.2 Wave function localisation

Wave functions of HOMO levels for 6 different cases are shown in Fig. 6. In the ideal crystalline structure the wave function of the HOMO level (and any other level) is completely delocalised, as Bloch theory predicts. When the side chain disorder is partially applied, wave functions remain delocalised (Fig. 6a and b). They are not delocalised along the whole structure, as in the ideal structure. Delocalisation is broken both in the π–π stacking direction and in the main chain direction. On the other hand, wave functions of HOMO levels in the case of disorder in main chains are localised, both with and without side chains included (Fig. 6c–f). They are localised on 5–15 rings, usually on 2 neighbouring chains (as in Fig. 6c and e). Therefore, thermal disorder in the crystalline P3HT localises the wave function of the HOMO level, as in the amorphous phase.[6,7]

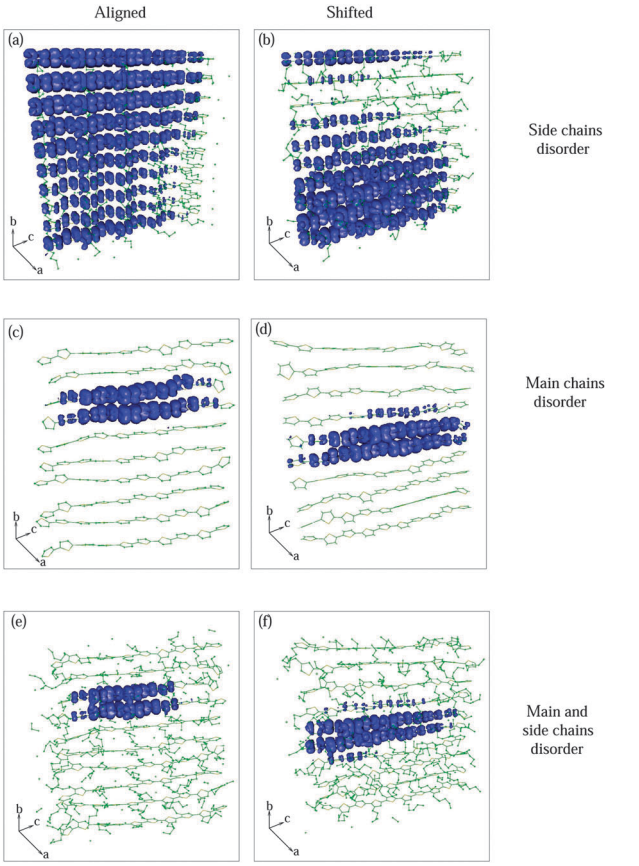

Fig. 6 Wave function moduli of the HOMO level of crystalline P3HT in the case of: (a) aligned structure with disorder in side chains; (b) shifted structure with disorder in side chains; (c) aligned structure with disorder in main chains and side chains omitted; (d) shifted structure with disorder in main chains and side chains omitted; (e) aligned structure with disorder in both side and main chains (f) shifted structure with disorder in both side and main chains. Isosurfaces correspond to the probability of finding a hole inside the surface of 90%.

To investigate the effects of disorder on the wave function localisation more precisely, we calculate two localisation lengths for each state: localisation in the π–π stacking direction L_b and localisation in the main chain direction L_c. If the wave functions are represented in the orthonormal basis set of well localised orbitals, the localisation length can be generally defined as $L = 1 \Big/ \sum_m |d_m|^4$, where d_m is the expansion coefficient of the wave functions in the orthonormal basis $|m\rangle$.[7] The basis set used in the OFM calculations is not orthonormal. The orthonormal basis set is constructed by transformation $|m\rangle = \sum_m T_{mi}|i\rangle$ using transformation matrix $T = (S^{-1/2})^*$, where S is the original overlap matrix and $|i\rangle$ are original basis wave functions. Expansion coefficients of the orthonormal basis set are related to the original coefficients c_i *via* $d_m = \sum_i \left(S^{1/2}\right)_{mi} c_i$. For the orthonormal basis set the condition $\sum_m |d_m|^2 = 1$ is satisfied. In our case, this sum can be divided into two sums, one over different chains and other over rings in one chain: $\sum_{i=1}^{N_c} \sum_{j=1}^{N_m} |\beta_{ij}|^2 = 1$,

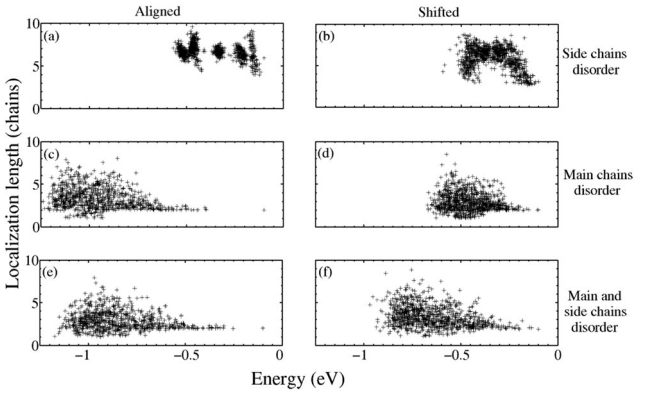

Fig. 7 Dependence of L_b on the energy of the electronic state in the case of: (a) aligned structure with disorder in the side chains; (b) shifted structure with disorder in the side chains; (c) aligned structure with disorder in main chains and side chains omitted; (d) shifted structure with disorder in main chains and side chains omitted; (e) aligned structure with disorder in both side and main chains (f) shifted structure with disorder in both side and main chains.

where N_c and N_m are the number of chains and the number of rings within one chain, respectively. Following the general definition of the localisation length, L_b is defined as $L_b = 1 \Big/ \sum_i |\beta_i'|^4$, where $|\beta_i'|^2 = \sum_{j=1}^{N_m} |\beta_{ij}|^2$. Similarly, L_c is defined as $L_c = 1 \Big/ \sum_j |\beta_j''|^4$, where $|\beta_j''|^2 = \sum_{i=1}^{N_c} |\beta_{ij}|^2$.

Plots of the dependence of L_b on the energy of the electronic states are shown in Fig. 7. In the ideal crystalline structure (both aligned and shifted), L_b of the HOMO level is equal to the number of chains, which is 10 in this case. Lower states in the ideal structure have an L_b of either 6.67 or 10. In the case of the aligned structure with disordered side chains (Fig. 7a), the values of L_b for the HOMO level vary from 4 to 10. Other states have L_b which is around the value of L_b in the ideal structure. In the case of the shifted structure, distribution of the energies of states is wider than in the aligned. Consequently, it is difficult to isolate the values of L_b for HOMO levels from Fig. 7b. Looking into the range of 0.2 eV below the highest energy, the value of L_b is between 3 and 6, which is lower than the values of L_b in aligned structures. Therefore, wave functions of HOMO levels are more localised in the shifted structure than in the aligned. In all remaining cases (Fig. 7c–f) we get qualitatively similar results. Values of L_b for the highest occupied states are low, they take values from 2 to 4 chains. States with lower energies have wider distributions of L_b, suggesting that delocalised states exist. The shape of the plot of L_b is similar to the plot of the hole localisation length of the amorphous P3HT, given in ref. 7.

Results for L_c are similar to the results for L_b. The minimal value for L_c when both side and main chains are disordered is 3. Electronic coupling is stronger in the main chain direction than in the π–π stacking direction and therefore localisation in the π–π stacking direction is stronger than in the chain direction.

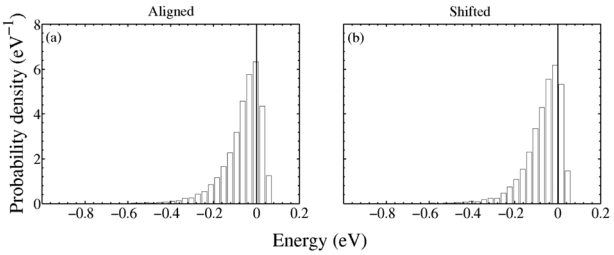

Fig. 8 Distribution of difference between electronic coupling between chains and variations of diagonal Hamiltonian elements in the case of: (a) aligned and (b) shifted structure.

It is interesting to note that the highest states in the valence band are typically localised on 2 neighbouring chains when main chains are disordered. The state will be localised on two chains if the electronic coupling $t_{mn} = \langle m|H|n\rangle$ between orbitals m and n from different chains is greater than variations of the diagonal Hamiltonian elements. The distributions of the quantity $d = t_{mn} - |H_{mm} - H_{nn}|$ are given in Fig. 8. Since d takes positive values as well, existence of strong coupling between chains is confirmed, which explains localisation on two neighbouring chains.

The total localisation length can be found using the general definition previously given. A plot of its dependence on the energy of the states is given in Fig. 9. For the highest states, when main chains are disordered, it takes values from 5 to 15 rings (Fig. 9c–f). These values are slightly higher than the values of the localisation length of highest states in the valence band of amorphous P3HT, which is around 5.[7] This difference is expected, since crystalline P3HT, despite the high degree of disorder, is still more ordered than amorphous. In the sense of the hole localization length, effects of disorder in crystalline and amorphous P3HT are similar. Delocalised states (localised on more than 10 rings) start to appear only few hundreds of meV below the top of the valence band. This is in agreement with the findings presented

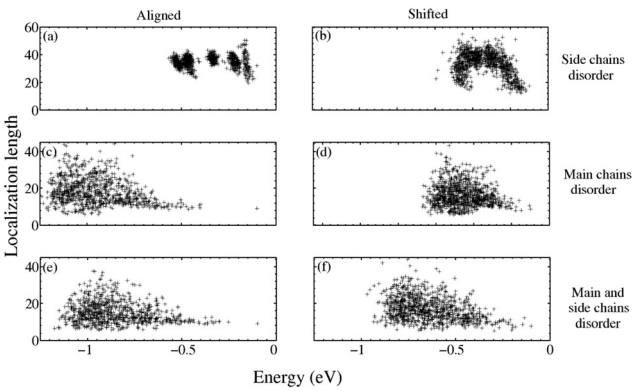

Fig. 9 Dependence of the total localization length on the energy of the electronic state in the case of: (a) aligned structure with disorder in the side chains; (b) shifted structure with disorder in the side chains; (c) aligned structure with disorder in main chains and side chains omitted; (d) shifted structure with disorder in main chains and side chains omitted; (e) aligned structure with disorder in both side and main chains (f) shifted structure with disorder in both side and main chains.

in ref. 17 where DOS and localization length in PBTTT are calculated. Results for the carrier localization orbital density of HOMO levels of crystalline P3HT at 300 K, given in ref. 15, indicate the presence of both localised (4–10 rings) and weakly (more than 10 rings) localised states. These calculations were performed without alkyl side chains and for isolated main chains. We obtain qualitatively the same results for L_c, since we find states localised on few rings within a chain and states that are extended over the entire chain. To conclude, our findings agree with previous findings that wave functions of the highest states in the valence band are localised and that delocalised (or weakly localised) states also exist below these states.

Results for total localization length and L_b are qualitatively similar for the structures with isolated disorder in main chains and with both disorder in main and side chains. Nevertheless, side chains have a significant quantitative effect on electronic properties. This can be seen by comparing the DOS (Fig. 3c *vs.* Fig. 3e and Fig. 3d *vs.* Fig. 3f), localization length (Fig. 9c *vs.* Fig. 9e and Fig. 9d *vs.* Fig. 9f) and on-site Hamiltonian elements (Fig. 5c *vs.* Fig. 5e and Fig. 5d *vs.* Fig. 5f). By comparing the figures one can also see that the effect of side chain disorder is stronger in the shifted than in the aligned structure, which is due to the larger conformational freedom of the shifted structure, as discussed in Section 3.1. Therefore, to obtain reliable results, side chains should be included in the calculations.

3.3 Consequences for electrical transport

We now discuss the consequences of our findings about thermal disorder on electrical properties of the material. In small molecule based organic crystals (SMOCs) the effects of thermal disorder[14] were used to explain the temperature dependence of the mobility where the mobility that decreases with increasing temperature is typically observed. On the other hand, all mobility measurements of P3HT, even for highest quality ordered samples, yield a thermally activated temperature dependence.

Our results suggest that in ordered P3HT there is a spectral region within first 200 meV below the top of the valence band with electronic states localised to just a few rings. In a combined molecular dynamics–electronic structure study in ref. 15 such states were found to be persistently localised in the sense that their position does not vary over time on the order of few nanoseconds. Below the spectral region with localised states, there is a region where both localised and delocalised states exist. It is well understood that the spatial and energetic distribution of electronic states that we obtained leads to thermally-activated transport; at low temperature most carriers populate localised states at the top of the valence band, which yield low mobility, while at higher temperatures less localised or delocalised states become more populated and the transport is much better then.[39]

However, what is the main difference between polymers and SMOCs where a different temperature dependence of mobility is observed? In SMOCs, thermal disorder leads to localised electronic states, as well. However, the spectral region where these states exist is much narrower. For example, in ref. 13 the spectral region with strongly localised states has the width of approximately $0.2t$, where t is the electronic coupling transfer integral between two neighbouring molecules (which is typically on the order of 100 meV in SMOCs). In ref. 10 this range is equally narrow and is comparable to or even smaller than thermal energy k_BT at room temperature. For this reason, thermally activated behaviour is not observed in SMOCs.

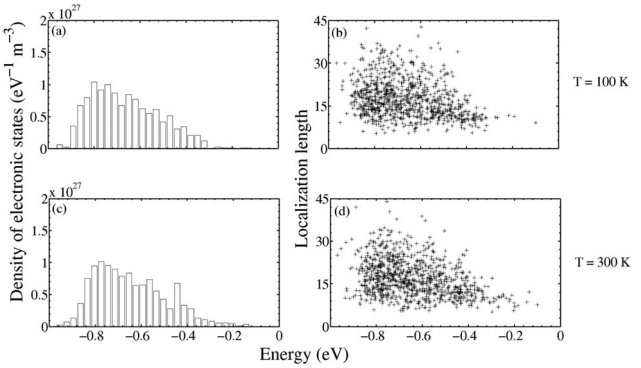

Fig. 10 (a) DOS of the shifted structure with disorder in main and side chains at 100 K. (b) Dependence of the total localization length on the energy of the electronic state of the shifted structure with disorder in main and side chains at 100 K. (c) DOS of the shifted structure with disorder in main and side chains at 300 K. (d) Dependence of the total localization length on the energy of the electronic state of the shifted structure with disorder in main and side chains at 300 K.

The comparison between the effects of thermal disorder in ordered polymers and SMOCs illustrates the dual role of temperature when thermal disorder and transport properties are concerned. The temperature acts on the one hand to create well localised states and on the other hand to promote the carriers from such localised states to delocalised states with better transport. In SMOCs higher temperatures lead to better localization of the states and consequently to a smaller mobility. On the other hand, in ordered P3HT polymers, in the range of temperatures from 100 K to 300 K, the temperature has a weak effect on the DOS and on the dependence of localization length on energy. This conclusion was obtained from the comparison of these two quantities at 100 K and 300 K, presented in Fig. 10. A weak effect of temperature on the degree of localization was also shown in ref. 15 (Table 1). Therefore, the temperature dependence of mobility in ordered polymers originates from thermal activation of carriers from localised states to delocalised or less localised states with better transport. While we show that the effects of thermal disorder alone lead to thermally activated mobility, this does not necessarily imply that they are the dominant cause of thermally activated mobility observed in realistic samples. Various imperfections of chemical or structural nature produce traps where carriers can be localised and these can also lead to thermally activated mobility.

4 Conclusion

In this work the effects of thermal disorder on the electronic structure of crystalline P3HT were investigated. The influence of side chains and main chains on the thermal disorder was investigated separately for the first time. The main conclusions

from the obtained results can be summarized as follows. The disorder in side chains has a significant effect on the electronic structure of P3HT. The effect is more pronounced in the shifted structure than in the aligned, due to higher conformational freedom of side chains. The disorder in main chains has a strong effect on the electronic structure, leading to the localization of HOMO level wave functions to few rings only. Such a degree of localization is similar to the localisation in amorphous P3HT and it is a possible cause of thermally activated mobility that is typically observed in ordered polymers.

Acknowledgements

This work was supported by a European Community FP7 Marie Curie Career Integration Grant (ELECTROMAT), the Serbian Ministry of Education, Science and Technological Development (Project ON171017) and FP7 projects (PRACE-3IP, HP-SEE[40] and EGI-InSPIRE).

References

1 R. H. Friend, R. W. Gymer, A. B. Holmes, J. H. Burroughes, R. N. Marks, *et al.*, *Nature*, 1999, **397**, 121–128.
2 J. H. Burroughes, D. D. C. Bradley, A. R. Brown, R. N. Marks, K. Mackay, R. H. Friend, P. L. Burns and A. B. Holmes, *Nature*, 1990, **347**, 539–541.
3 V. L. Colvin, M. C. Schlamp and A. P. Alivisatos, *Nature*, 1994, **370**, 354–357.
4 A. Dodabalapur, L. Torsi and H. E. Katz, *Science*, 1995, **268**, 270–271.
5 G. Li, V. Shrotriya, J. S. Huang, Y. Yao, T. Moriarty, K. Emery and Y. Yang, *Nat. Mater.*, 2005, **4**, 864.
6 N. Vukmirović and L. W. Wang, *J. Phys. Chem. B*, 2009, **113**, 409–415.
7 N. Vukmirović and L.-W. Wang, *J. Phys. Chem. B*, 2011, **115**, 1792–1797.
8 T. Vehoff, B. Baumeier, A. Troisi and D. Andrienko, *J. Am. Chem. Soc.*, 2010, **132**, 11702–11708.
9 A. Troisi and D. L. Cheung, *J. Chem. Phys.*, 2009, **131**, 014703.
10 A. Troisi, *J. Chem. Phys.*, 2011, **134**, 034702.
11 J. Böhlin, M. Linares and S. Stafström, *Phys. Rev. B: Condens. Matter Mater. Phys.*, 2011, **83**, 085209.
12 Y. Yao, W. Si, X. Hou and C.-Q. Wu, *J. Chem. Phys.*, 2012, **136**, 234106.
13 S. Fratini and S. Ciuchi, *Phys. Rev. Lett.*, 2009, **103**, 266601.
14 A. Troisi and G. Orlandi, *Phys. Rev. Lett.*, 2006, **96**, 086601.
15 D. L. Cheung, D. P. McMahon and A. Troisi, *J. Am. Chem. Soc.*, 2009, **131**, 11179–11186.
16 D. P. McMahon, D. L. Cheung, L. Goris, J. Dacuna, A. Salleo and A. Troisi, *J. Phys. Chem. C*, 2011, **115**, 19386–19393.
17 T. Liu and A. Troisi, *Adv. Funct. Mater.*, 2013, **24**, 925–933.
18 M. Allen and D. J. Tildesley, *Computer Simulation of Liquids*, Clarendon Press, Oxford Science Publications, New York, USA, 1987.
19 N. Vukmirović and L. W. Wang, *J. Chem. Phys.*, 2008, **128**, 121102.
20 M. Mladenović, N. Vukmirović and I. Stanković, *J. Phys. Chem. C*, 2013, **117**, 15741–15748.
21 N. Vukmirović and L.-W. Wang, *J. Chem. Phys.*, 2011, **134**, 094119.
22 D. L. Cheung, D. P. McMahon and A. Troisi, *J. Phys. Chem. B*, 2009, **113**, 9393–9401.
23 O. Alexiadis and V. G. Mavrantzas, *Macromolecules*, 2013, **46**, 2450–2467.
24 S. Dag and L.-W. Wang, *J. Phys. Chem. B*, 2010, **114**, 5997–6000.
25 W. Xie, Y. Y. Sun, S. B. Zhang and J. E. Northrup, *Phys. Rev. B: Condens. Matter Mater. Phys.*, 2011, **83**, 184117.
26 C. Poelking and D. Andrienko, *Macromolecules*, 2013, **46**, 8941–8956.
27 R. S. Bhatta, Y. Y. Yimer, D. S. Perry and M. Tsige, *J. Phys. Chem. B*, 2013, **117**, 10035–10045.
28 M. Moreno, M. Casalegno, G. Raos, S. V. Meille and R. Po, *J. Phys. Chem. B*, 2010, **114**, 1591–1602.
29 T. J. Prosa, M. J. Winokur, J. Moulton, P. Smith and A. J. Heeger, *Macromolecules*, 1992, **25**, 4364–4372.
30 R. Colle, G. Grosso, A. Ronzani and C. M. Zicovich-Wilson, *Phys. Status Solidi B*, 2011, **248**, 1360–1368.
31 N. Kayunkid, S. Uttiya and M. Brinkmann, *Macromolecules*, 2010, **43**, 4961–4967.
32 A. Maillard and A. Rochefort, *Phys. Rev. B: Condens. Matter Mater. Phys.*, 2009, **79**, 115207.
33 W. L. Jorgensen, D. S. Maxwell and J. Tirado-Rives, *J. Am. Chem. Soc.*, 1996, **118**, 11225–11236.
34 R. G. Parr and W. Yang, *Density-Functional Theory of Atoms and Molecules*, Oxford University Press, New York, USA, 1989.
35 K. D. Meisel, H. Vocks and P. A. Bobbert, *Phys. Rev. B: Condens. Matter Mater. Phys.*, 2005, **71**, 205206.
36 S. Zade and M. Bendikov, *Chem. – Eur. J.*, 2008, **14**, 6734–6741.
37 E. J. Bylaska, W. A. de Jong, N. Govind, K. Kowalski, T. P. Straatsma, M. Valiev, D. Wang, E. Apra, T. L. Windus, J. Hammond, P. Nichols, S. Hirata, M. T. Hackler, Y. Zhao, P.-D. Fan, R. J. Harrison, M. Dupuis, D. M. A. Smith, J. Nieplocha, V. Tipparaju, M. Krishnan, Q. Wu, T. V. Voorhis, A. A. Auer, M. Nooijen, E. Brown, G. Cisneros, G. I. Fann, H. Fruchtl, J. Garza, K. Hirao, R. Kendall, J. A. Nichols, K. Tsemekhman, K. Wolinski, J. Anchell, D. Bernholdt, P. Borowski, T. Clark, D. Clerc, H. Dachsel, M. Deegan, K. Dyall, D. Elwood, E. Glendening, M. Gutowski, A. Hess, J. Jaffe, B. Johnson, J. Ju, R. Kobayashi, R. Kutteh, Z. Lin, R. Littlefield, X. Long, B. Meng, T. Nakajima, S. Niu, L. Pollack, M. Rosing, G. Sandrone, M. Stave, H. Taylor, G. Thomas, J. van Lenthe, A. Wong and Z. Zhang, *NWChem, A Computational Chemistry Package for Parallel Computers, Version 5.1*, Pacific Northwest National Laboratory, Richland, Washington 99352-0999, USA, 2007.

38 M. Valiev, E. Bylaska, N. Govind, K. Kowalski, T. Straatsma, H. V. Dam, D. Wang, J. Nieplocha, E. Apra, T. Windus and W. de Jong, *Comput. Phys. Commun.*, 2010, **181**, 1477.
39 N. F. Mott and E. A. Davis, *Electronic Processes in Non-Crystalline Materials*, Clarendon Press, New York, USA, 1979.
40 This work makes use of results produced by the High-Performance Computing Infrastructure for South East Europe's Research Communities (HP-SEE), a project co-funded by the European Commission (under contract number 261499) through the Seventh Framework Programme. HP-SEE involves and addresses the specific needs of a number of new multi-disciplinary international scientific communities and thus stimulate the use and expansion of the emerging new regional HPC infrastructure and its services. Full information is available at: http://www.hp-see.eu/.

THE JOURNAL OF PHYSICAL CHEMISTRY C

Article

pubs.acs.org/JPCC

Electronic States at the Interface between Crystalline and Amorphous Domains in Conjugated Polymers

Marko Mladenović[†,‡] and Nenad Vukmirović*[,†]

[†]Scientific Computing Laboratory, Institute of Physics Belgrade, University of Belgrade, Pregrevica 118, 11080 Belgrade, Serbia

[‡]School of Electrical Engineering, University of Belgrade, P.O. Box 35-54, 11120 Belgrade, Serbia

ABSTRACT: Conjugated polymers exhibit complex structure with interlaced crystalline and amorphous domains. We have investigated electronic structure of the interface between crystalline and amorphous domains in poly(3-hexylthiophene) (P3HT). Two types of the interface were considered: sharp interface and interface composed of extended chains. We have found that HOMO states of both interface types belong to the crystalline domains. States belonging to both domains were not found. We have calculated HOMO and LUMO band offsets between crystalline and amorphous domains. These offsets are close to previous estimates in the case of interface with extended chains. We find that there is no formation of trap states at the investigated interfaces. Regardless of the interface type, amorphous domains present high barriers for charge carriers, which lead to charge transport through crystalline domains.

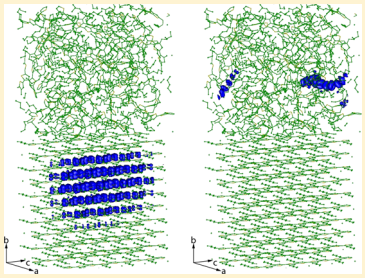

INTRODUCTION

Organic semiconductors based on conjugated polymers have stimulated significant research interest in last decades due to their applications in organic solar cells, organic field-effect transistors, and organic light-emitting diodes.[1−5] Understanding the electronic and transport properties of conjugated polymers is the precondition for the enhancement of their performance. On the other hand, electronic structure of a material is strongly affected by its atomic structure. Conjugated polymers exhibit complex structure: they contain both crystalline (ordered) and amorphous (disordered) domains.[6,7] While the electronic structures of single crystalline and single amorphous domains are well understood, there is a lack of knowledge about the electronic structure of the interface between these two regions.

In real conjugated polymers, amorphous and crystalline domains are interlaced. According to previous works,[6−9] it is believed that a single polymer chain typically spreads across both amorphous and crystalline domains. There are three types of such chains: bridge chains, which connect different crystalline regions through an amorphous region; folded chains, which connect different parts of the same crystalline domain and extended chains, which are extended out from crystalline and have their end in the amorphous domain.[6,7] However, chains can also be entirely localized in the crystalline or amorphous domain. Amorphous domains have larger band gap than crystalline due to reduced electronic coupling between monomer units.[6,7,10,11] Differences in band gaps produce band offsets in the valence and conduction band between crystalline and amorphous domains. Offset in the valence band acts as a barrier for a hole to jump from crystalline domain into amorphous.[6,11−13] In all previous works, amorphous and crystalline domains in conjugated polymers were investigated separately and the effects of the interface between these two domains were not explicitly taken into account.

To fully understand electronic properties of conjugated polymers, calculations that include both crystalline and amorphous domains are needed. In this paper we perform such calculations and obtain microscopic insights into the electronic states at the interface between crystalline and amorphous regions in poly(3-hexylthiophene) (P3HT). We consider two types of interfaces that we call type A and type B. Type A interface is a sharp interface between an amorphous and an ordered domain where P3HT chains belong exclusively to one of these regions, as shown in Figure 1a. This type of interface is an idealization that is highly suitable to investigate the difference between ordered and disordered regions. On the other hand, it is unlikely that a realistic interface is that sharp. Therefore, we additionally consider the type A′ interface, where an intermediate region exists between the ordered and the amorphous regions (Figure 1b). Type B interface consists of two ordered domains whose chains extend into the region between them and form an amorphous region (Figure 1c). It is believed that this type of interface is a reasonably good representation of interfaces that exist in real materials.[6,7]

In this work, we mainly investigate the energy level alignment between the states in the two regions and the possibility of having interface trap states within the band gap of the material. For all interface types we model the ordered region as an ideal crystal. Realistic ordered regions are not perfect crystals and exhibit the effects of thermal (dynamical) disorder and paracrystallinity. In our previous work,[14] we found that the effects of thermal disorder produce variations of the energy levels in the valence band on the order 0.1−0.2 eV and therefore we do not include them in this work. Along the same

Received: July 11, 2015
Revised: September 14, 2015
Published: September 16, 2015

DOI: 10.1021/acs.jpcc.5b06673
J. Phys. Chem. C 2015, 119, 23329−23333

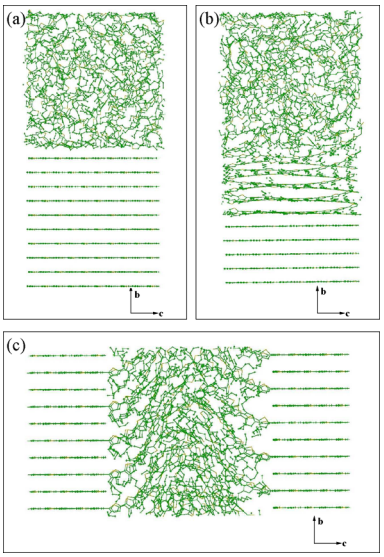

Figure 1. Atomic structures of interfaces considered in this work: (a) type A; (b) type A′; and (c) type B.

line, we do not expect that the effect of paracrystallinity, when it is reasonably small, will change the main conclusions of our work.

Our results indicate that wave functions of HOMO states are delocalized and belong to ordered domains, regardless of the interface type. Localized states in disordered domains start to appear at the energies few hundreds meV below HOMO in the case of realistic type B interface. In the case of sharp type A interface, the difference between HOMO levels in crystalline and amorphous domains is even larger. Additionally, there is no evidence of the existence of states belonging to both domains. Therefore, disordered regions present barriers for hole transport which, consequently, dominantly goes through crystalline regions.

METHODOLOGY

Atomic structure of the interface between ordered and disordered region was generated using in-house developed Monte Carlo (MC) simulations,[15] while electronic structure was calculated using the charge patching method (CPM)[16] and the overlapping fragments method (OFM).[17] Methods for the electronic structure calculations were described in detail in previous works.[10,14,16−20] Therefore, in this section we focus on the description of the procedure for generating the atomic structure.

During MC simulations crystalline domains were kept rigid. There are several types of crystalline structures reported in the literature.[14,21,22] We chose the shifted structure (neighboring chains in the $\pi-\pi$ stacking direction mutually shifted by a half of the unit cell in the backbone direction) with interdigitated side chains as representative, since it was shown that this structure is energetically favorable.[14,21] Lattice constants were obtained from NPT (constant pressure and temperature) MC simulations at zero temperature and pressure of 101.325 kPa, using the OPLS parameters set[23,24] for nonbonded interactions. These lattice constants are $a/2$ = 15.55 Å, b = 8.1 Å, and c = 7.77 Å.

The procedure for generation of amorphous domains is different for type A and B interfaces. In the case of type A interface, at the beginning, P3HT chains were randomly placed in the simulation box, which was significantly larger than the final. The box was gradually compressed until the density of amorphous P3HT reached its experimental value of around 1.1 g/cm^3.[25] Type A′ interface was generated using the same atomic configuration as for the type A interface, with a difference that several chains in the crystalline domain closest to the amorphous region were allowed to move freely. For type B interface, two different starting configurations were used: one with interdigitated backbone chains and the other where backbone chains were separated by a predefined distance in the backbone direction (denoted as c-direction in figures). In this case, the simulation box was compressed only in the backbone direction until the density in the amorphous region between crystalline domains reached its experimental value. For all types of interfaces, the temperature of 1000 K was used in MC simulations. At the end, when the final density of the amorphous region is reached, the system was cooled down to 0 K. By keeping the crystalline structure rigid and by cooling the amorphous structure, effects of thermal disorder[14] were excluded to keep focus on the difference between crystalline and amorphous region. Energy of the system in MC simulations was modeled as a sum of nonbonded van der Waals and Coloumb interactions and interring torsion potentials. OPLS parameter set was used for nonbonded interactions and torsion potentials of dihedrals within side chains, while thiophene−thiophene torsion potential was taken from ref 10. Periodic boundary conditions were applied in all directions.

Each of the obtained interface atomic structures contains around 10000 atoms. Electronic structure calculations on such systems are not feasible using standard density functional theory (DFT) codes.[26] Therefore, CPM was applied instead of DFT. Electronic charge density was calculated directly by adding contributions (called motifs) of each atom in a system.[16] Charge density of motifs was extracted from DFT calculations on a small prototype system, which consists of three thiophene rings. When charge density was obtained, the single-particle Hamiltonian was constructed. The Hamiltonian was diagonalized using OFM, which divides the system into small fragments that consist of three neighboring rings (called trimers) and uses eigenstates of these small systems as the basis set.[17]

We note that our electronic structure calculations yield the Kohn−Sham orbitals of a charge neutral system. Therefore, polaronic effects that arise as a consequence of nuclei relaxation in the presence of an additional charge are not included. The changes of energy levels due to polaronic effects were previously estimated to be on the order of 100 meV or smaller (Supporting Information, ref 27), which justifies their neglect. Additional charge also induces polarization charges at the interface of two materials with different dielectric constants. This effect is negligible in our case because we investigate the interface of two forms of the same material. Our calculations are based on local density approximation which does not yield the correct band gap. Nevertheless, the band gap error is expected to be nearly the same for ordered and disordered form of the same material and therefore obtained band offsets are reliable.

RESULTS

As explained, type A interface is a sharp interface between crystalline and amorphous region where each chain belongs to one of these regions. Both regions in the structures that we simulated contain 20 P3HT chains, each 10 thiophene rings

DOI: 10.1021/acs.jpcc.5b06673
J. Phys. Chem. C 2015, 119, 23329−23333

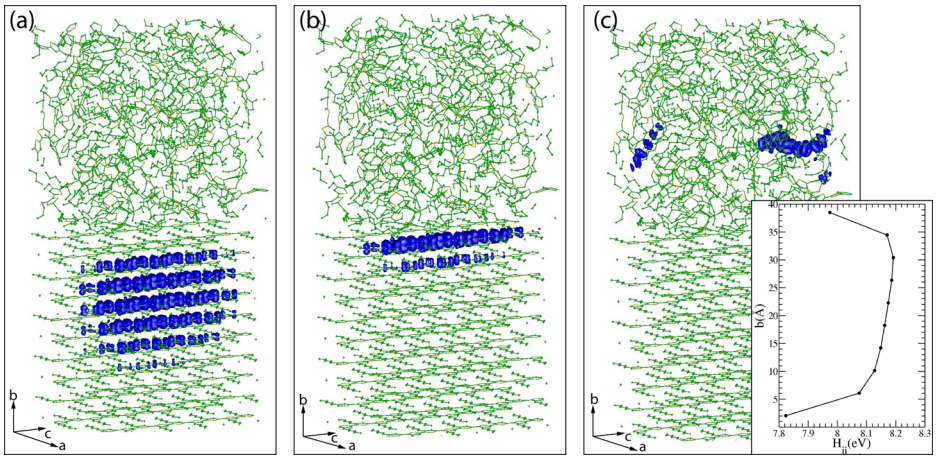

Figure 2. Wave function moduli squared of the (a) highest electronic state in the valence band in the crystalline domain, (b) localized electronic state in the valence band in the crystalline domain, and (c) highest electronic state in the valence band in the amorphous domain in the case of type A interface. The inset shows the distribution of the averaged diagonal Hamiltonian elements in the crystalline domain along *b*-direction. Isosurfaces correspond to the probability of finding a hole inside the surface of 75%.

long. In the crystalline region, the chains are arranged in two lamellas, where one lamella contains 10 chains stacked in the $\pi-\pi$ direction (denoted as *b*-direction in the figures). We have calculated energies and wave functions of the electronic states in the valence band for four different random realizations of the system. The results that were obtained are similar for all realizations and indicate that three different types of electronic states exist: (1) delocalized states in the crystalline domain (Figure 2a), (2) localized states at the edge of the crystalline domain (Figure 2b), and (3) localized states in the amorphous domain (Figure 2c). Highest states are delocalized and belong to the crystalline domain. These states have highest energies due to the strongest electronic coupling between thiophene rings (both inter- and intrachain coupling). Localized states in the crystalline domain start to appear at energies of around 0.4 eV below HOMO. These states are localized at P3HT chains, which are nearest to the amorphous region. Diagonal Hamiltonian elements of the rings nearest to the interface are smaller than diagonal Hamiltonian elements of the rings far from the interface, which can be clearly seen from the distribution of the diagonal Hamiltonian elements across *b*-direction, given in the inset of Figure 2c. Values of the elements are obtained by averaging the diagonal Hamiltonian elements of the rings that have the same *b*-coordinate. Consequently, such states have lower energies than the energy of delocalized HOMO state. Localized states are not possible in ideal crystalline domains, which are periodic in all crystallographic directions. Therefore, localized states in the crystalline domain near the interface are induced by the interface. Finally, localized states in the amorphous domain start to appear at the energies around 1 eV below HOMO. These states fully resemble the states in purely amorphous P3HT.[10,18]

Band offsets of HOMO and LUMO levels between amorphous and crystalline domains were estimated from local density of states (DOS), given in Figure 3 for one realization of the structure for each interface type. Values of offsets can vary up to 0.2 eV depending on the structure. According to Figure 3a, HOMO band offset for type A interface is around 1 eV. On the other hand, LUMO in the amorphous domain has similar energy as LUMO in the crystalline domain. It is usually assumed that HOMO and LUMO offsets are equal to the half of the band gap difference between crystalline and amorphous

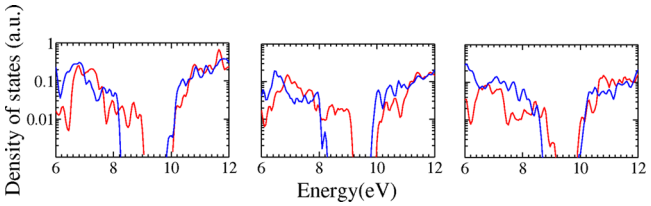

Figure 3. Density of electronic states (arbitrary units, logarithmic scale) of crystalline (red) and amorphous (blue) region in the case of (a) type A interface, (b) type A′ interface, and (c) type B interface.

domain. According to previously reported results, this offset is expected to be in the range of 0.1−0.3 eV.[6,10,11,13] Our results indicate that the presence of disordered domain affects the energy levels in crystalline domains. This can be clearly seen from the distribution of diagonal Hamiltonian elements from different chains in crystalline region (inset of Figure 2c). Difference between the diagonal Hamiltonian elements of the rings furthest from the interface and the rings closest to the interface is around 0.3 eV. Therefore, energy levels in the crystalline domain far from the interface are shifted by approximately 0.3 eV toward higher energies. This shift leads to an increase in HOMO band offset and a decrease in LUMO band offset in comparison to the offsets estimated as half of the band gap difference. The shift may originate from uneven charge distribution at the interface between ordered and disordered chains.

Intermediate region between amorphous and crystalline region (type A′ interface) presents a more realistic interface model than the sharp interface. In our simulation it consists of five P3HT chains and there is the same number of chains in crystalline region. As expected, chains closer to the crystalline region are well-ordered and chains closer to the amorphous region are more disordered (Figure 1b). The main difference between electronic structures of type A and A′ interfaces is in the localization lengths of the states in the ordered domains. Wave function of HOMO state of the type A′ interface is delocalized (Figure 4a), but with significantly lower localization length than HOMO state of the type A interface due to disorder in the intermediate domain. Highest states in the perfectly ordered domains (Figure 4b) have energies only few meV below HOMO. The difference between the HOMO state

DOI: 10.1021/acs.jpcc.5b06673
J. Phys. Chem. C 2015, 119, 23329−23333

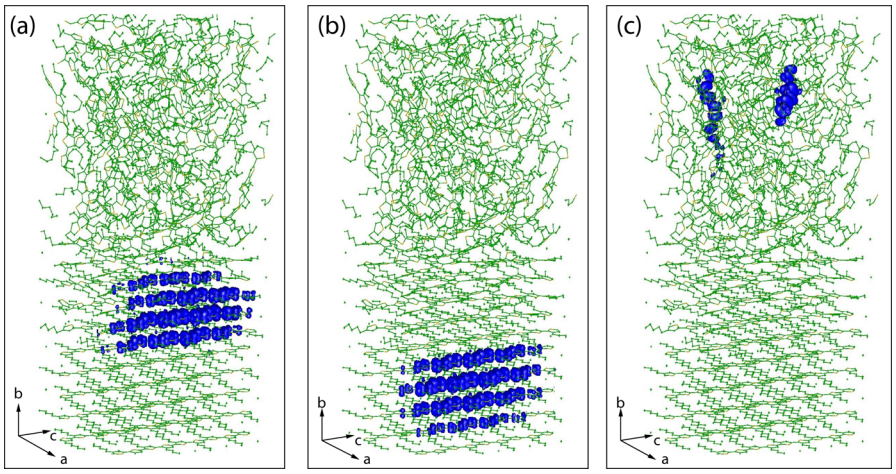

Figure 4. Wave function moduli squared of the (a) highest electronic state in the valence band in the intermediate domain, (b) highest electronic state in the valence band in the crystalline domain, and (c) highest electronic state in the valence band in the amorphous domain in the case of type A′ interface. Isosurfaces correspond to the probability of finding a hole inside the surface of 75%.

and the highest localized states in the amorphous domain (Figure 4c) is around 1 eV (Figure 3b), similar as in the case of sharp interface.

Type B interface is composed of 20 chains, where each chain contains 20 thiophene rings. Half of the rings in each chain belong to the amorphous, other half to the crystalline region. Results for the hole wave functions and energies were extracted from 8 different realizations (4 for each starting structure). We have found that in such structure two types of states exist: (1) delocalized states in crystalline domain (Figure 5a) and (2) localized states in amorphous domain (Figure 5b). The HOMO state is completely delocalized in the ordered domain. Localized states start to appear at the energies around 0.4 eV below HOMO (Figure 3c). This result is more in line with previous expectations due to the fact that this interface type is more realistic, contrary to the sharp type A interface. Wave functions of the states can leak slightly from crystalline domain to amorphous and vice versa, but they are dominantly localized in one of them. Interestingly, states in the amorphous domain can be localized on two chains, which can be explained by the presence of some degree of ordering between disordered chains.

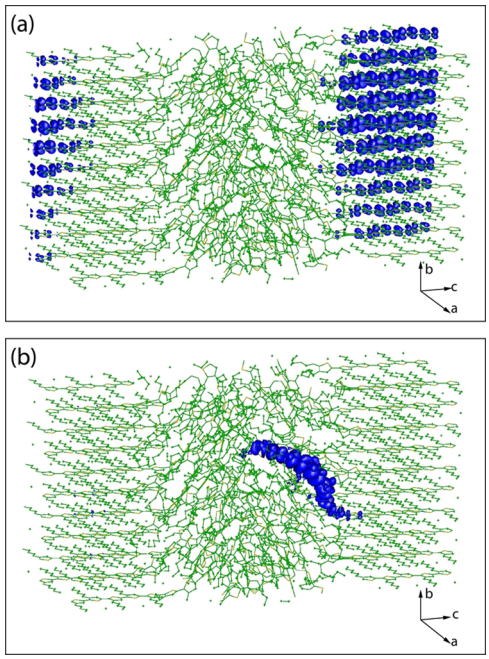

Figure 5. Wave function moduli squared of the (a) highest electronic state in the valence band in the crystalline domain and (b) highest electronic state in the valence band in the amorphous domain in the case of type B interface. Isosurface correspond to the probability of finding a hole inside the surface of 75%.

Our results indicate that the interface between amorphous and crystalline domain does not introduce trap states in the band gap of crystalline domain. This is a generally positive feature, having in mind that the presence of such trap centers would deteriorate charge mobility. Moreover, there are no states which belong to both domains. These results are qualitatively different from the results for the electronic structure of grain boundaries between misaligned naphthalene crystals, given in ref 19. At the grain boundaries in polycrystalline naphthalene there are points of both stronger and reduced electronic coupling between molecules. States localized at the points of strong electronic coupling act as traps. On the other hand, electronic coupling between chains in amorphous and crystalline domains in P3HT is always smaller than the coupling between chains in crystalline domains. This coupling is even not able to form the states which belong to both domains. The only type of states which are in some way induced by the interface are localized states at the edge of crystalline domains in type A interface. In type B interface similar states do not exist, because the drop in the electronic coupling between the rings in the direction perpendicular to the plane of the interface is not that high.

CONCLUSION

In this work electronic states at the interface between crystalline and amorphous domains in P3HT were investigated. We have considered two different interface types: sharp interface and more realistic interface that consists of extended chains. Results can be summarized as follows. Highest states in the valence band are delocalized in the crystalline domains for both interface types. Highest states in the amorphous domains are localized on one or two chains, as in the case of single amorphous domain. Amorphous domain presents a barrier for

DOI: 10.1021/acs.jpcc.5b06673
J. Phys. Chem. C 2015, 119, 23329−23333

hole transport due to high energetic offset between highest states in the crystalline and in the amorphous domain. This offset is comparable to other reported results in the case of interface that consists of extended chains. In the case of sharp interface, this offset is larger due to the energy levels shift in the crystalline domain. Importantly, we find that none of the investigated interfaces leads to formation of trap states at the interface. These results indicate that in conjugated polymer materials charge transport takes place through crystalline domains. While our results indicate that amorphous domains present barriers for charge transport, we note that paths for fast charge transport through the amorphous domain could exist if well-ordered bridging chains connect the crystalline domains through the amorphous domain, as proposed in ref 6.

AUTHOR INFORMATION

Corresponding Author

*E-mail: nenad.vukmirovic@ipb.ac.rs.

Notes

The authors declare no competing financial interest.

ACKNOWLEDGMENTS

This work was supported by a European Community FP7 Marie Curie Career Integration Grant (ELECTROMAT) and the Serbian Ministry of Education, Science and Technological Development (Project ON171017). Numerical simulations were run on the PARADOX supercomputing facility at the Scientific Computing Laboratory of the Institute of Physics Belgrade.

REFERENCES

(1) Friend, R. H.; Gymer, R. W.; Holmes, A. B.; Burroughes, J. H.; Marks, R. N.; et al. Electroluminescence in Conjugated Polymers. *Nature* **1999**, *397*, 121−128.

(2) Burroughes, J. H.; Bradley, D. D. C.; Brown, A. R.; Marks, R. N.; Mackay, K.; Friend, R. H.; Burns, P. L.; Holmes, A. B. Light-Emitting Diodes Based on Conjugated Polymers. *Nature* **1990**, *347*, 539−541.

(3) Colvin, V. L.; Schlamp, M. C.; Alivisatos, A. P. Light-Emitting Diodes Made from Cadmium Selenide Nanocrystals and a Semiconducting Polymer. *Nature* **1994**, *370*, 354−357.

(4) Dodabalapur, A.; Torsi, L.; Katz, H. E. Organic Transistors - 2-Dimensional Transport and Improved Electrical Characteristics. *Science* **1995**, *268*, 270−271.

(5) Li, G.; Shrotriya, V.; Huang, J. S.; Yao, Y.; Moriarty, T.; Emery, K.; Yang, Y. High-Efficiency Solution Processable Polymer Photovoltaic Cells by Self-Organization of Polymer Blends. *Nat. Mater.* **2005**, *4*, 864−868.

(6) Noriega, R.; Rivnay, J.; Vandewal, K.; Koch, F. P.; Stingelin, N.; Smith, P.; Toney, M. F.; Salleo, A. A General Relationship Between Disorder, Aggregation and Charge Transport in Conjugated Polymers. *Nat. Mater.* **2013**, *12*, 1038−1044.

(7) Lan, Y.-K.; Huang, C.-I. Charge Mobility and Transport Behavior in the Ordered and Disordered States of the Regioregular Poly(3-hexylthiophene). *J. Phys. Chem. B* **2009**, *113*, 14555−14564.

(8) Crossland, E. J. W.; Tremel, K.; Fischer, F.; Rahimi, K.; Reiter, G.; Steiner, U.; Ludwigs, S. Anisotropic Charge Transport in Spherulitic Poly(3-hexylthiophene) Films. *Adv. Mater.* **2012**, *24*, 839−844.

(9) Brinkmann, M.; Wittmann, J.-C. Orientation of Regioregular Poly(3-hexylthiophene) by Directional Solidification: A Simple Method to Reveal the Semicrystalline Structure of a Conjugated Polymer. *Adv. Mater.* **2006**, *18*, 860−863.

(10) Vukmirović, N.; Wang, L. W. Electronic Structure of Disordered Conjugated Polymers: Polythiophenes. *J. Phys. Chem. B* **2009**, *113*, 409−415.

(11) Tsoi, W. C.; Spencer, S. J.; Yang, L.; Ballantyne, A. M.; Nicholson, P. G.; Turnbull, A.; Shard, A. G.; Murphy, C. E.; Bradley, D. D. C.; Nelson, J.; et al. Effect of Crystallization on the Electronic Energy Levels and Thin Film Morphology of P3HT:PCBM Blends. *Macromolecules* **2011**, *44*, 2944−2952.

(12) Kaake, L. G.; Barbara, P. F.; Zhu, X.-Y. Intrinsic Charge Trapping in Organic and Polymeric Semiconductors: A Physical Chemistry Perspective. *J. Phys. Chem. Lett.* **2010**, *1*, 628−635.

(13) Sweetnam, S.; Graham, K. R.; Ngongang Ndjawa, G. O.; Heumüller, T.; Bartelt, J. A.; Burke, T. M.; Li, W.; You, W.; Amassian, A.; McGehee, M. D. Characterization of the Polymer Energy Landscape in Polymer:Fullerene Bulk Heterojunctions with Pure and Mixed Phases. *J. Am. Chem. Soc.* **2014**, *136*, 14078−14088.

(14) Mladenović, M.; Vukmirović, N. Effects of Thermal Disorder on the Electronic Properties of Ordered Polymers. *Phys. Chem. Chem. Phys.* **2014**, *16*, 25950−25958.

(15) Allen, M.; Tildesley, D. J. *Computer Simulation of Liquids*; Clarendon Press, Oxford Science Publications: New York, U.S.A., 1987.

(16) Vukmirović, N.; Wang, L. W. Charge Patching Method for Electronic Structure of Organic Systems. *J. Chem. Phys.* **2008**, *128*, 121102.

(17) Vukmirović, N.; Wang, L.-W. Overlapping Fragments Method for Electronic Structure Calculation of Large Systems. *J. Chem. Phys.* **2011**, *134*, 094119.

(18) Vukmirović, N.; Wang, L.-W. Density of States and Wave Function Localization in Disordered Conjugated Polymers: A Large Scale Computational Study. *J. Phys. Chem. B* **2011**, *115*, 1792−1797.

(19) Mladenović, M.; Vukmirović, N.; Stanković, I. Electronic States at Low-Angle Grain Boundaries in Polycrystalline Naphthalene. *J. Phys. Chem. C* **2013**, *117*, 15741−15748.

(20) Mladenović, M.; Vukmirović, N. Charge Carrier Localization and Transport in Organic Semiconductors: Insights from Atomistic Multiscale Simulations. *Adv. Funct. Mater.* **2015**, *25*, 1915−1932.

(21) Dag, S.; Wang, L.-W. Packing Structure of Poly(3-hexylthiophene) Crystal: Ab Initio and Molecular Dynamics Studies. *J. Phys. Chem. B* **2010**, *114*, 5997−6000.

(22) Poelking, C.; Andrienko, D. Effect of Polymorphism, Regioregularity and Paracrystallinity on Charge Transport in Poly(3-hexylthiophene) [P3HT] Nanofibers. *Macromolecules* **2013**, *46*, 8941−8956.

(23) Jorgensen, W. L.; Maxwell, D. S.; Tirado-Rives, J. Development and Testing of the OPLS All-Atom Force Field on Conformational Energetics and Properties of Organic Liquids. *J. Am. Chem. Soc.* **1996**, *118*, 11225−11236.

(24) Cheung, D. L.; McMahon, D. P.; Troisi, A. A Realistic Description of the Charge Carrier Wave Function in Microcrystalline Polymer Semiconductors. *J. Am. Chem. Soc.* **2009**, *131*, 11179−11186.

(25) Pfaff, M.; Klein, M. F.; Müller, E.; Müller, P.; Colsmann, A.; Lemmer, U.; Gerthsen, D. Nanomorphology of P3HT:PCBM-Based Absorber Layers of Organic Solar Cells after Different Processing Conditions Analyzed by Low-Energy Scanning Transmission Electron Microscopy. *Microsc. Microanal.* **2012**, *18*, 1380−1388.

(26) Parr, R. G.; Yang, W. *Density-Functional Theory of Atoms and Molecules*; Oxford University Press: New York, U.S.A., 1989.

(27) Vukmirović, N.; Wang, L.-W. Charge Carrier Motion in Disordered Conjugated Polymers: A Multiscale Ab Initio Study. *Nano Lett.* **2009**, *9*, 3996−4000.

DOI: 10.1021/acs.jpcc.5b06673
J. Phys. Chem. C 2015, 119, 23329−23333

Charge Carrier Localization and Transport in Organic Semiconductors: Insights from Atomistic Multiscale Simulations

*Marko Mladenović and Nenad Vukmirović**

Organic electronic semiconducting materials exhibit complex atomic structures with a lack of periodicity that lead to charge carrier localization which, in turn, strongly affects the electronic transport properties of these materials. To understand charge carrier localization and electronic transport in organic semiconductors, simulations that take into account the details of the atomic structure of the material are of utmost importance. In this article, computational methods that can be used to simulate the electronic properties of organic semiconductors are reviewed and an overview of the results that have been obtained from such simulations is given. Using these methods the effects of static disorder, thermal disorder and interfaces between domains are investigated and the microscopic origin of these effects is identified. It is shown that in strongly disordered conjugated polymer materials the main origin of the localization of charge carrier wave functions is the disordered long-range electrostatic potential. In ordered polymers, thermal disorder of main chains leads to wave function localization. In small molecule based organic semiconductors, grain boundaries introduce localized trap states at the points where electronic coupling is the strongest. It is also demonstrated that detailed atomistic simulations are necessary for quantitative and sometimes even qualitative description of charge mobility in organic materials.

1. Introduction

Organic semiconductors based on conjugated polymers and small molecules have emerged in the last two decades as materials with applications in sensing, lighting, displays, solar energy conversion, and so forth.[1–10] Their main advantage is a significantly lower production cost in comparison to their inorganic counterparts.[11] Organic materials obtained by standard processing techniques exhibit a wealth of structures,[12–14] including completely disordered spaghetti-like regions formed by interlaced chains of conjugated polymers,[15] ordered regions of polymer chains arranged in two-dimensional lamellar structures,[16,17] polycrystalline small molecule-based structures[18–21] and small molecule-based single crystals.[22,23] The variety of organic semiconductors, their possible morphologies and the complexity of these morphologies make understanding of their electronic properties a rather challenging task. One cannot exploit the well developed theory of inorganic crystalline semiconductors where charge carriers are fully delocalized Bloch waves whose transport is limited by occasional scattering on phonons, defects or impurities.

On the other hand, a common feature of almost all organic semiconductors is the localization of charge carriers at band edge energies which arises due to a certain type of disorder in the material. In this feature article, we will discuss and quantify various effects of disorder that lead to charge carrier localization. We will also discuss the consequences of charge carrier localization on electrical transport properties of these materials.

To reliably calculate the wave functions and their localization properties in disordered organic semiconductors, the calculations on the length scale larger than the wave function localization length are necessary. This implies the length on the order of several nanometers, which encompasses several thousand atoms. Such a number of atoms is beyond what is achievable by standard density functional theory (DFT) based calculations. Consequently, the need for understanding the electronic properties of organic semiconductors has stimulated the development of methods for electronic structure calculations. These methods will be described in Section 3. Before describing these methods and the insights obtained from their applications to organic semiconducting materials, we will introduce a toy model of an organic semiconductor in Section 2. This model will be very helpful to qualitatively understand the essence of most effects obtained from detailed atomistic simulations. Section 4 is devoted to the overview of insights obtained from atomistic simulation about the electronic properties of the material, such as the wave function localization and the electronic density of states (DOS). In Section 5, we present insights into the electrical transport in amorphous polymers obtain from the simulations and briefly discuss possible insights into the electrical transport of other classes of organic semiconductors.

M. Mladenović, Dr. N. Vukmirović
Scientific Computing Laboratory
Institute of Physics Belgrade
University of Belgrade
Pregrevica 118
11080 Belgrade, Serbia
E-mail: nenad.vukmirovic@ipb.ac.rs

DOI: 10.1002/adfm.201402435

2. A Toy Model Hamiltonian of an Organic Semiconductor

We model the electronic Hamiltonian of the states near the top of the valence band (or the bottom of the conduction band) as

$$H = \sum_{i=1}^{N_c} H_i + \sum_{i=1}^{N_c} \sum_{j=1}^{i-1} H_{ij} \tag{1}$$

where

$$H_i = \sum_{j=1}^{L_i} \varepsilon_{ij} a_{ij}^{+} a_{ij} - \sum_{j=1}^{L_i} \sum_{k=1}^{j-1} t_{i,j;i,k} \left(a_{ij}^{+} a_{ik} + a_{ik}^{+} a_{ij} \right) \tag{2}$$

and

$$H_{ij} = -\sum_{m=1}^{L_i} \sum_{n=1}^{L_j} t_{i,m;j,n} a_{im}^{+} a_{jn} \tag{3}$$

In Equations 1–3 N_c is the total number of polymer chains, L_i is the length (number of monomers) of polymer chain i, ε_{ij} is the on-site energy of the monomer j on chain i, $t_{m,j;n,k}$ are the electronic coupling elements between the monomer j on chain m and the monomer k on chain n, while a_{ij} and a_{ij}^{+} are the carrier annihilation and creation operators on site j in chain i. This Hamiltonian is flexible enough to provide insight into various classes of organic materials as will be discussed below. Schematic illustration of the parameters of the Hamiltonian is presented in **Figure 1**a.

Ideally ordered polymer regions (**Figure 2**e) consist of two dimensional planes of parallel aligned chains.[24–28] In the chain direction, the monomers are bonded by covalent bonds which lead to strong electronic coupling. In the direction in the planes perpendicular to the chain direction (π–π stacking direction), the chains are bonded by weak van der Waals interaction and electronic coupling in that direction is still sufficient to cause delocalization of electronic wave function. In the third direction the planes are separated by insulating alkyl side chains which lead to completely negligible electronic coupling and conduction. Consequently, ordered polymers can to a first approximation be modeled by taking all chain lengths to be equal $L_i = \text{const}$, by assuming equal nearest neighbor intrachain electronic coupling elements $t_{i,j;i,j+1} = t_1$ and by taking the interchain coupling elements between neighboring monomers from different chains equal to another constant $t_{i,j;i+1,j} = t_2$, while the remaining coupling elements are assumed to be equal to zero. The value of t_1 in conjugated polymers can be estimated as half the bandwidth of HOMO (or LUMO) band of a straight polymer chain. These bandwidths are typically on the order of 2 eV (see the literature[29] for the cases of polythiophene, polyfuran and polypyrrole), which leads to the estimate for t_1 of 1 eV. On the other hand, the value of t_2 can be estimated from the bandwidth in the π–π stacking direction, which is on the order of 0.2 eV (see another study for the case of polythiophenes)[28] and gives an estimate for t_2 of 0.1 eV.

In strongly disordered polymers, the chains form a spaghetti-like structure (Figure 2d). The origin of such a shape of the chains is the fact that the energy required to rotate the monomers around the bond that connects them is comparable to thermal energy. Such rotations lead to irregular shape of the chain. It is important to note that the chains keep their shape on a time scale of at least a nanosecond.[30] This timescale is longer than the timescale relevant for charge transport processes. Therefore the disorder introduced by the irregular shape of the chains is called the "static disorder". The effects of static disorder are reflected both in the on-site energies and in the electronic coupling elements in the Hamiltonian that are no longer constant but vary in space in a largely random manner. In a disordered polymer material the monomer experiences the electrostatic potential from charges on all other monomers. Since the orientations of these monomers are largely random, the potential they create is also random and this leads to variations of monomer on-site energies. On the other hand, the electronic coupling between the neighboring monomers is mostly determined by their mutual orientations. It is well understood that the overlap of π orbitals strongly depends on the angle between them. In a typical chain in disordered polymers, the angles between monomers take largely random values, which leads to variations of intrachain nearest neighbor electronic coupling elements. Therefore, the static disorder in amorphous polymers is reflected through variations of on-site elements in Equation 2 caused by random electrostatic potential

Marko Mladenović is Research Assistant at the Institute of Physics Belgrade. His research interests are electronic and transport properties of organic semiconductors. He obtained his MSc degree in nanoelectronics and photonics at the School of Electrical Engineering, University of Belgrade in 2012. Currently, he is a PhD student working under the supervision of Dr. Nenad Vukmirović. He is the recipient of the 2014 E-MRS Graduate Student Award.

Dr. Nenad Vukmirović is Associate Research Professor at the Institute of Physics Belgrade. His research interests are theory and simulation of electronic properties of organic semiconductor materials and quantum nanostructures. He received his BSc degree in physics in 2003 and in electrical engineering in 2004, both from the University of Belgrade. He received his PhD degree in electrical engineering in 2007 from University of Leeds, UK. From 2007 to 2010 he was a postdoctoral fellow at Lawrence Berkeley National Laboratory. Dr. Vukmirović is holder of the FP7 Marie Curie Career Integration Grant for the project Electronic Transport in Organic Materials.

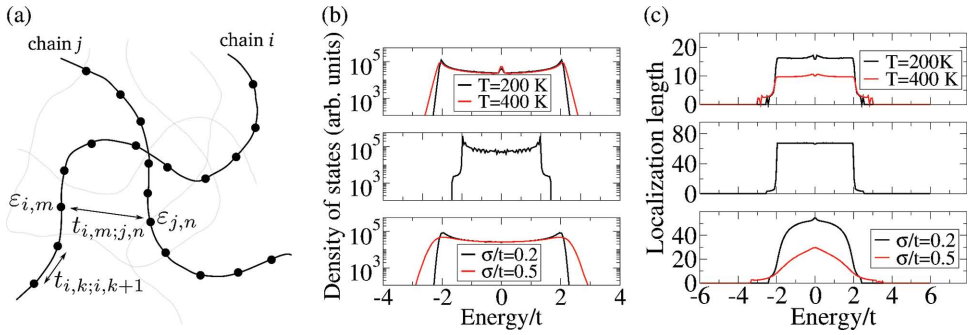

Figure 1. a) Schematic representation of disordered polymer morphology and relevant parameters of the toy model Hamiltonian. b) Electronic DOS and c) the localization length for one dimensional model with Gaussian disorder (bottom), model of a grain boundary (middle) and model of an organic crystal (top).

and through variations of electronic coupling elements in Equation 2,3 caused by rotations of the monomers around the bonds that connect them.

The Hamiltonian which is representative of small molecule based organic crystals (Figure 2f) can be obtained if one assumes that $L_i = 1$ and that $t_{i,1;j,1} = t_2$ for molecules which are nearest neighbors. Typical values of t_2 are on the order of 50 meV.[31,32] Such a Hamiltonian at first sight exhibits no effects of disorder because all the parameters of the Hamiltonian are constant and the system is perfectly periodic. However, a characteristic feature of organic materials is that the oscillations of atoms around their equilibrium positions at finite temperature are significant due to softness of intermolecular van der Waals bonds.[33] Each of the parameters of the Hamiltonian depends on atomic positions. At a certain moment in time, the atomic positions are not periodic and the parameters of the Hamiltonian take values that vary through space in a random manner. Such a disorder introduced by oscillations of atoms around their equilibrium positions is called the dynamic disorder or thermal disorder. In small molecule based crystals, the variations of $t_{i,1;j,1}$ are comparable to its mean value.[33,34]

The proposed model can also account for the effects of grain boundaries in organic crystals, through the changes in electronic coupling elements at the grain boundary.

Thermal disorder is also present in polymer based materials. In strongly disordered polymers it is an additional component of disorder that comes on top of strong static disorder and is therefore of secondary importance. However, in ordered polymer regions it is of major importance since it is the only type of disorder.

In this article, we will not take into account possible effects of polarons on the properties of organic semiconductors. The polarons are quasiparticles formed from a charged particle and the surrounding cloud of atomic displacements induced by the presence of the charged particle which lower the energy of the particle. In the Hamiltonian given by Equation 1–3 polaronic effects could be modeled by taking into account the dependence of the parameters on the atomic coordinates and by adding an additional term with the dependence of the energy of the neutral system on atomic coordinates. There is recent evidence in the literature that in several types of organic semiconductors the effects of polarons might not be as important

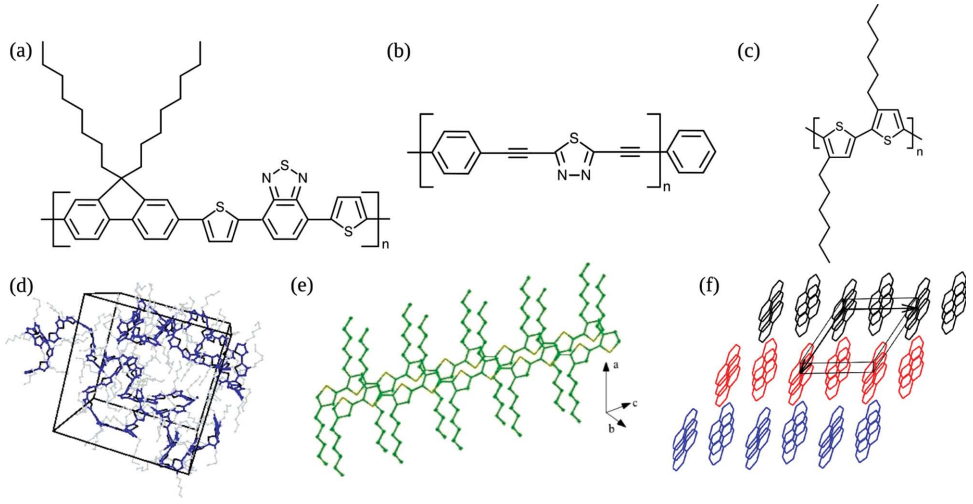

Figure 2. Chemical formulae of conjugated polymers mentioned in this article: a) poly[2,7-(9,9-dioctyl-fluorene)-alt-5,5-(4′,7′-di-2-thienyl-2′,1′,3-benzothiadiazole)] (APFO-3); b) 2,5-bis(phenylethynyl)-1,3,4-thiadiazole (PhEtTh); (c) poly(3-hexylthiophene) (P3HT) and atomic structures of several classes of organic semiconductors: d) disordered polymers; e) ordered polymers; f) small molecule based crystals.

as previously thought. The results of DFT calculations of long straight polythiophene chains have indicated that polaron binding energy is on the order of few meVs only and that it can be ignored in practice.[35,36] It has been argued elsewhere[37] that small polaron formation does not take place in oligoacenes such as pentacene and rubrene. Our calculations point out to the same conclusion for pentathiophene monolayers[38] and naphthalene crystals.[39] It is more difficult to assess the effect of polarons in disordered materials because of the lack of theoretical framework that is capable of accounting for the effects of disorder and polarons on equal footing in realistic materials. Nevertheless, one may argue that if the strength of disorder (quantified for example by the magnitude of spatial variations of onsite elements in the Hamiltonian) is larger than the monomer polaron binding energy, the effects of disorder would have a major influence on the electrical properties of the material. In this article we focus on the effects of localization caused by static or dynamic disorder and show that these are sufficient to lead to significant localization of band edge wave functions without the polaronic effects. On the other hand, further understanding of the role of polarons in organic materials is certainly desirable.

3. Methods for Electronic Structure Calculations

In this section, the methods that can be used in practice to calculate the electronic structure of organic semiconductors will be briefly described.

Atomic structure of the material is needed as an input for electronic structure calculations. In the studies of thermal disorder in ordered materials one starts with an ideal room temperature crystal structure and then evolves the system in time using molecular dynamics (MD) technique or samples various possible atomic configurations using a configurational Monte Carlo (MC) approach.[40] After the equilibration of the system takes place, one continues with the production run where uncorrelated snapshots of the atomic configuration of the system are extracted for further use in electronic structure calculations. To obtain the atomic structure of amorphous material, a more elaborate approach is needed. This is accomplished using a simulated annealing procedure. Initially, polymer chains are placed in a box which is much larger than the one that corresponds to experimental density of the material and a high temperature of 1000 K is imposed. The size of the box is then gradually decreased during the MC or MD simulation until it reaches the final size that corresponds to experimental density of the material. Finally, the temperature is also gradually decreased down to room temperature and the system is relaxed to a local minimum. The procedure of this type was established as a standard procedure for the generation of the atomic structure of amorphous polymers.[41–47] While such procedures are typically applied in simulations of amorphous polymers, one should keep in mind that the atomic structures obtained are only models that are constructed to capture the features of fully disordered polymer materials. It is well established from experiments that the polymer molecular weight affects the order in the structures and that realistic materials contain both ordered and disordered regions. It is a challenging task that is beyond of the scope of this article to obtain the atomic structure of polymer based materials in such cases.

After obtaining the atomic structure of the material, electronic structure calculations can be performed. This can be done, in principle, using DFT.[48] Within DFT, Kohn-Sham equations for wave functions of all occupied electronic states have to be solved self-consistently. Due to its significant computational cost, this approach is typically practiced only for systems with less than a thousand atoms which is usually not sufficiently large size to obtain reliable information about the properties of disordered materials.

Charge patching method (CPM)[49] can be used to directly calculate the electronic charge density. This method is based on the assumption that the contribution of a particular atom to the total electronic charge density of the system depends mainly on its local environment. Such contributions are called motifs and these are extracted from a DFT calculation of a small prototype system where atoms have the same bonding environment as in the simulated system. Contribution of an atom A at a position R_A is given as[49]

$$m_A(\mathbf{r}-\mathbf{R}_A)=\frac{w_A(\mathbf{r}-\mathbf{R}_A)}{\sum_B w_B(\mathbf{r}-\mathbf{R}_B)}\rho(\mathbf{r}) \tag{4}$$

where $\rho(r)$ is the electronic charge density obtained from DFT calculation on the small prototype system, while w_A is the weight function of an atom A. The total electronic charge density of the large system that one wants to simulate is then calculated as a sum of contributions of motifs corresponding to each atom in the system. When charge density is known, the single-particle Hamiltonian can be constructed as

$$H=-\frac{\hbar^2}{2m_0}\nabla^2+v_I+\frac{e}{4\pi\varepsilon_0}\int\frac{\rho(\mathbf{r}')}{|\mathbf{r}-\mathbf{r}'|}\mathrm{d}^3\mathbf{r}'+v_{xc}^{\mathrm{LDA}}(\rho) \tag{5}$$

where the first term is the kinetic term, the second term is the potential of core ions, the third term is the electrostatic (Hartree) potential, while the last term is the exchange-correlation term calculated using local density approximation (LDA) within DFT. The Hamiltonian obtained using CPM gives an accurate approximation of the DFT/LDA Hamiltonian for systems where there is no long range charge transfer with typical eigenenergy errors on the order of tens of meV.[49]

To describe electrical transport properties of a semiconducting material, only spectral region in the vicinity of the band gap is relevant. Therefore it is not necessary to find all eigenvalues of the Hamiltonian given by Equation (5). Instead, one can find the eigenstates closest to a certain reference energy using the folded spectrum method (FSM).[50,51] The main idea of the method is to solve the eigenvalue problem of the operator $(H-E_{\mathrm{ref}})^2$. Lowest eigenstates of this operator correspond to the eigenstates of the operator H closest to reference energy E_{ref}. With a proper choice of E_{ref} one can find the relevant states at the bottom of the conduction band or the top of the valence band.

For a system containing a large number of atoms, the use of FSM for the diagonalization of the Hamiltonian represented in plane wave basis may become too computationally demanding. Instead of using plane waves as the basis set, the Hamiltonian

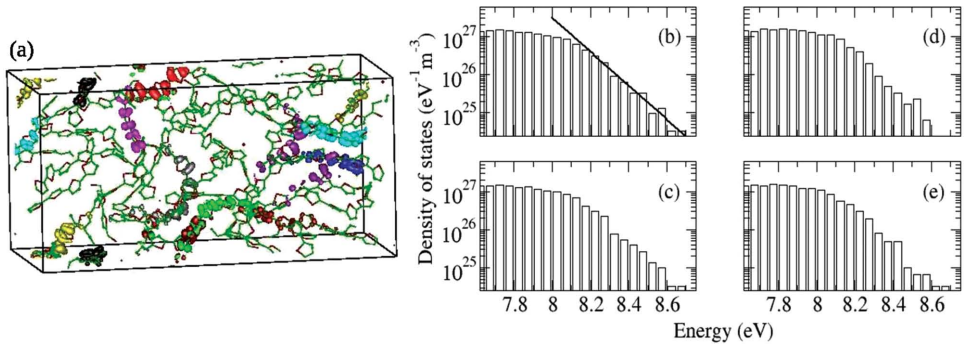

Figure 3. a) Wave functions moduli squared of top ten hole states in the portion of amorphous P3HT material of the size $58.6 \times 29.3 \times 29.3 \text{Å}^3$. The isosurfaces correspond to the 50% probability of finding the hole inside the surface. b) The hole DOS in amorphous P3HT material obtained from the full calculation; c) in the absence of interchain electronic coupling; d) calculated by including the intrachain electronic coupling between the nearest neighbors only; e) calculated by assuming that the intrachain electronic coupling between nearest neighbors is constant and equal to $t = 0.85$ eV.

can be represented in a localized and physically motivated system specific basis set. Overlapping fragments method (OFM)[52] is an efficient method which is based on the division of the system into small fragments and the use of eigenvectors of the fragments as the basis set. Good representation of relevant electronic states is obtained when the fragments mutually overlap. To achieve sufficient accuracy, only a few states per fragment are needed. OFM is particularly suitable for systems in which division into fragments is natural, such as conjugated polymers.

Several other methods have also been applied in the literature to calculate the electronic structure of large portions of organic materials—these include the density functional tight-binding method,[53] localized molecular orbital method,[54] and sometimes even direct DFT calculation[42] which however puts a severe restriction on the size of the system that can be tackled with available computational resources.

4. Localization and the Density of States

The effects of disorder discussed in Section 2 lead to localization of band edge wave functions and to the tail in the electronic DOS at the spectral region near the band edge. Grain boundaries introduce the wave functions localized at the boundary whose energies are within the band gap of the bulk semiconductor. In this section we present the densities of states and the localization lengths obtained from detailed atomistic simulations and provide insight into the origin of the results obtained with the help of a toy model presented in Section 2.

4.1. Amorphous Polymers

The wave functions and energies of electronic states in the region near the top of the valence band in the amorphous P3HT polymer (whose chemical formula is given in Figure 2c) were calculated using the CPM and OFM, as described in Section 3. The calculations have been performed for 50 different realizations of the system that consists of 12 chains, each 40 thiophene units long.[55] Such a system has 12024 atoms altogether. The electronic DOS near the top of the valence band obtained from such a set of calculations is presented in **Figure 3**b, while the dependence of localization length on energy is shown in **Figure 4**a. The localization length L was calculated as $L = 1 / \sum_m |d_m|^4$, where d_m are expansion

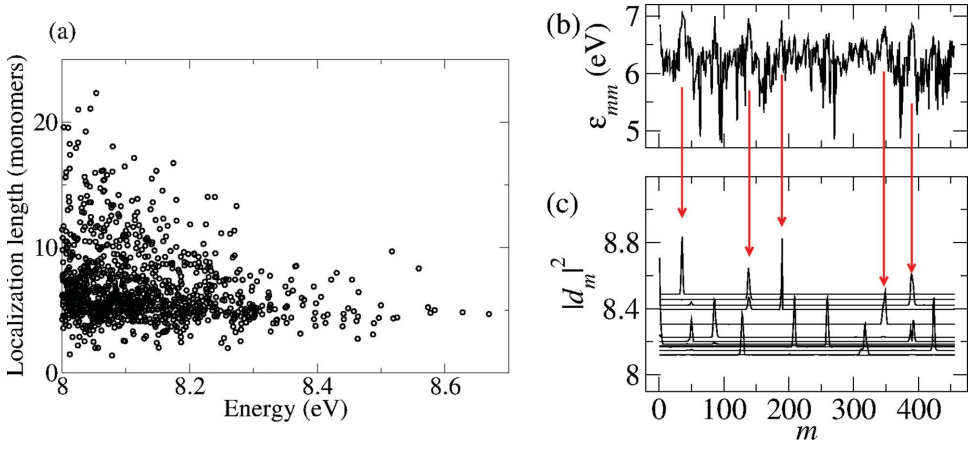

Figure 4. a) Dependence of localization length on energy in amorphous P3HT polymer; b) On-site Hamiltonian matrix elements ε_{mm} (where m is the index of the site on the polymer chain) for one realization of 12 024 atom P3HT polymer system; c) The wave functions of top hole states in 12024 atom P3HT system. $|d_m|^2$ are moduli squared in the expansion of the wave function in an orthonormal basis set shifted by the energy of the hole state in eV.

coefficients of the wave function in the orthonormal and localized basis $|m\rangle$. Strictly speaking, this quantity is in literature called the inverse participation ratio (IPR) and can be thought of as the number of monomers that the wave function is localized on. When IPR is multiplied by the length of one monomer it gives us the information about the length of the region of space where the wave function is localized. For this reason, IPR can also be thought of as the localization length where the unit of length is the length of one monomer. In the rest of this article IPR will be referred to as the localization length. The results indicate that electronic states near the valence band edge are strongly localized, while as one goes away from the band edge more delocalized states start to appear. The DOS exhibits a tail which can be well fitted with an exponential function, as shown in Figure 3b. As discussed in detail in the literature,[55] the best fit with an exponential function gives 84% confidence that the distribution is exponential, while the fits using a Gaussian function give the confidence of 16% or less.

To understand different effects in the system, we have mapped the Hamiltonian obtained from the CPM and OFM to the form of the Hamiltonian discussed in Section 2 by using the Lowdin's orthonormalization procedure, as discussed in detail elsewhere.[55]

4.1.1. The Origin of Localization

A picture that is often used to understand the localization of wave functions in conjugated polymers is so called conjugation break model. Within such a picture the wave functions are delocalized along the planar parts of the polymer chain where electronic coupling between the monomers is strong. The places where the torsion angle between the monomers is larger than some critical value break the conjugation and localize the wave function. The simplest mathematical description of the conjugation break model is the special case of the toy model outlined in Section 2 where on-site elements are constant and nearest neighbor coupling elements are constant as well, except that at the places where the conjugation break takes place they take the zero value. Within such a model the wave functions at the band edge would have the largest localization length, while the states further away from the band edge would be more localized. These results suggest that the simple conjugation break model is not appropriate for the description of amorphous polymers as it yields a completely different behavior of the dependence of localization length on energy than the one obtained from atomistic simulations. The main origin of this is the absence of variations of on-site Hamiltonian matrix elements caused by disordered electrostatic potential, which is known to be important in organic materials.[47,56,57]

On the other hand, the localization of band edge states is well known from the theory of one-dimensional disordered systems.[58] For example, a system described by our toy model Hamiltonian with constant nearest neighbor electronic coupling elements and with onsite elements drawn from a Gaussian distribution yields the dependence of localization length on energy which is qualitatively similar to the dependence that we obtain. However, a more detailed investigation is required to understand the origin of the dependence of localization length that we obtain and to establish if the results obtained can be really related to the results of disordered one-dimensional systems.

On that route, one first has to establish if the polymer material can in certain sense be considered simply as a collection of independent polymer chains. In Section 2, we have discussed that interchain electronic coupling in ordered polymers is an order of magnitude smaller than the intrachain coupling. In amorphous polymers where the spatial region between the main chains is also filled by insulating side chains, it is expected that interchain electronic coupling is even less important since it may have significant values only at certain points in space where parts of two main chains are closely stacked. To check if this is really the case, we have excluded interchain electronic coupling from the calculation. The DOS obtained without interchain electronic coupling is presented in Figure 3c. By comparing Figure 3b and Figure 3c it is evident that the effect of interchain coupling on electronic DOS is very small. The same is the case for the dependence of localization length on energy (not shown) which changes only slightly in the absence of interchain electronic coupling. One should note that these results do not suggest that interchain electronic coupling is irrelevant in organic materials. In Sections 4.2. and 4.3. we demonstrate the important role of interchain or intermolecular electronic coupling in the formation of electronic states in ordered polymers and at grain boundaries between small molecule based crystals. In addition, when electrical transport is concerned, long-range transport is impossible without interchain coupling which is required for charge transfer between different chains.

Next, to simplify the Hamiltonian, we exclude all intrachain electronic coupling elements except the ones between nearest neighbors. The comparison of Figure 3b and Figure 3d indicates that this is a good approximation. Finally, we set all nearest neighbor electronic coupling elements to a constant value $t = 0.85$ eV which corresponds to the most probable value in the distribution of these elements. Even such a drastic change has a weak effect on electronic DOS, as seen by comparing Figure 3b and Figure 3e. Such a result shows that the Hamiltonian which includes only on-site elements and constant nearest neighbor intrachain coupling elements captures the main features of the electronic states near the band edge, including their localization properties. Consequently, the variations of on-site elements that originate from disordered electrostatic potential introduced from the rest of the system are responsible for localization of wave functions rather than the breaks in conjugation. This conclusion can further be supported from Figure 4b,c. The hole wave functions are localized precisely at the places of largest on-site elements in agreement with the notion that these elements are responsible for localization.

4.1.2. The Factors that Influence the Electrostatic Disorder

Given the established importance of the disordered electrostatic potential created by the rest of the system on a certain site, it is of great relevance to understand the factors that determine the degree of spatial variations of such a potential. In typically used conjugated polymers there is always some degree

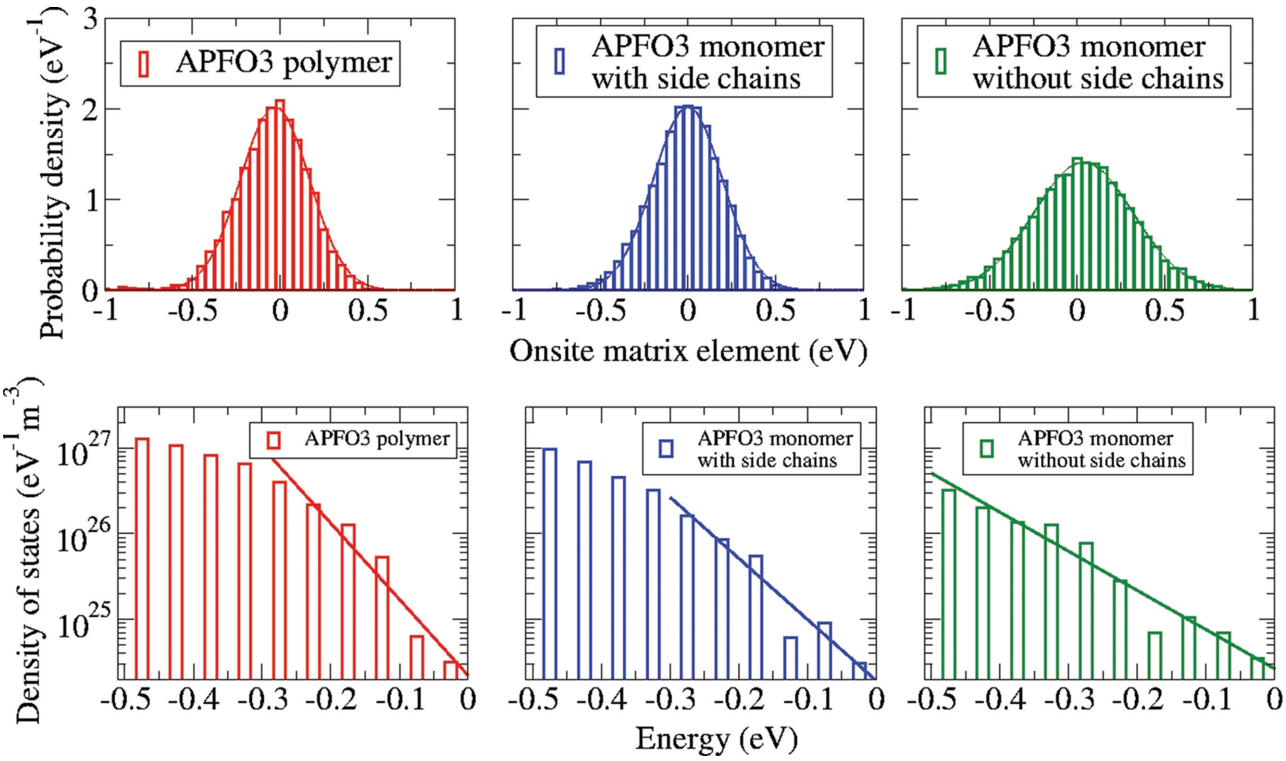

Figure 5. The distribution of on-site matrix elements for several materials based on APFO-3 (top). The lines are best fits to the Gaussian distribution with the standard deviation parameter $\sigma = 197$ meV (APFO-3 polymer), $\sigma = 197$ meV (APFO-3 monomer with side chains), and $\sigma = 282$ meV (APFO-3 monomer without side chains). The density of hole states for these materials (bottom). The lines represent fits to the exponential DOS $D(E) = D_0 \exp(-E / E_b)$, with $E_b = 48.9$ meV for APFO-3 polymer, $E_b = 60.9$ meV for APFO-3 monomer with side chains and $E_b = 95.1$ meV for APFO-3 monomer without side chains.

of charge transfer in the monomer. Consequently, from the electrostatic point of view, each monomer can be considered as a dipole that creates a long-ranged electrostatic potential. Since the polymers have irregular shape, the orientations of these dipoles vary and there is a great degree of randomness in the overall potential created by these dipoles. The strength of the electrostatic potential on a certain site depends both on the strength of the dipoles and on their distances from the site. For this reason, one expects that alkyl side chains that act as spacers between the main chains tend to reduce the electrostatic disorder.

To investigate the effects of electrostatic disorder in more detail, we consider three systems based on APFO-3 polymer (whose chemical formula is given in Figure 2a), the APFO-3 polymer with side chains, the APFO-3 monomer with side chains, and the APFO-3 monomer without side chains.[59] The monomer of APFO-3 is in a donor–acceptor–donor configuration which leads to the creation of dipoles within the monomer. For this reason, it is an interesting material for the study of electrostatically induced disorder. To quantify the electrostatic disorder, we present the distribution of diagonal Hamiltonian matrix elements H_{ii}, where i is the fragment orbital. The distribution of these elements in the case of APFO-3 polymer with side chains and APFO-3 monomer with side chains is presented in **Figure 5**. These distributions are nearly the same which is an expected result since both systems have the same built-in dipoles in the monomer and the same distribution of distances between the sites on the main chain and the dipoles. In addition, the distribution of torsion angles in both systems is rather similar which leads to similar distribution of the dipoles orientation. On the other hand, the comparison of the APFO-3 monomer with and without side chains (also shown in Figure 5) yields a wider distribution of elements in the monomer without side chains. The origin of wider distribution is the absence of side chains, which leads to proximity of the surrounding dipoles and consequently to a stronger and more disordered potential.

Next, we compare the DOS of the three materials, shown in Figure 5. It is expected that the material with wider distribution of diagonal matrix elements has a wider tail in the DOS at the band edge. Indeed, as seen from the fit of the DOS to an exponential function presented in Figure 5, APFO-3 monomer without side chains has significantly larger E_b than the other two materials. The comparison of APFO-3 polymer and APFO-3 monomer with side chains yields somewhat smaller E_b in APFO-3 polymer. These two materials have the same distribution of diagonal elements, while the smaller E_b in APFO-3 polymer comes from tail narrowing introduced by intrachain electronic coupling in the polymer.[59]

4.1.3. Impact of Electrostatic Disorder on the Band Gap

The effect of disordered electrostatic potential may be so pronounced in some materials to even lead to a drastic reduction

of the band gap. One such material is PhEtTh (whose chemical formula is given in Figure 2b).[60] The calculation of the amorphous PhEtTh sample, consisting of 5 decamers (1010 atoms) yields the bandgap of 0.62 eV. On the other hand, the band gap of an isolated straight PhEtTh chain is 1.64 eV, while the band gaps of isolated chains in the amorphous geometry take the values in the 1.60–1.85 eV range. One should note that these band gaps were obtained from the calculation based on the LDA approximation and are therefore underestimated in comparison to true band gaps. Nevertheless, here we are mainly interested in the change of the band gap from straight polymer single chain to amorphous material and we are not focused on the absolute values of the band gap. The reader interested in the absolute value of the band gap may estimate it by dividing the LDA gap with a factor of 0.6.[60]

The directly calculated interchain coupling elements in amorphous PhEtTh take the values on the order of 10 meV and these certainly cannot explain the difference between the band gaps of the material and the individual chains. To understand this band gap difference, we have performed the calculations where we have represented the Hamiltonian in the basis of eigenstates of single chains. In this basis certain coupling elements can be easily turned on and off and therefore their influence on the electronic structure can be identified. First, we represent the Hamiltonian in this basis and do not turn any elements off. We obtain the band gap of 0.79 eV, somewhat different than the band gap obtained by plane wave diagonalization. This difference originates from the incompleteness of the basis set used. However, this difference is not large and therefore this basis set can be used to understand the role of different coupling elements. Next, the interchain coupling elements of the Hamiltonian $H-H_s$ (where H is the Hamiltonian of the whole system, while H_s is the sum of Hamiltonians of individual isolated chains) between the eigenstates of single chains were turned off and the band gap obtained is 0.8 eV. Then, we also turn off the intrachain off-diagonal coupling elements and obtain the band gap of 1.01 eV. Finally, when onsite term is also ignored we obtain the single chain band gap of 1.6–1.85 eV.

From these calculations, we can identify the relative importance of various factors in determining the band gap of the system. Individual chains have band gaps in the 1.6–1.85 eV region. Other chains create an additional potential on each chain which changes the onsite energies and leads to the reduction of the band gap to 1.01 eV. This potential also mixes different states from a particular chain, which leads to further band gap reduction to 0.8 eV. Finally, interchain electronic coupling has a rather weak effect and only slightly reduces the band gap to 0.79 eV.

Such a drastic effect of electrostatic potential on the band gap was not obtained in polythiophene polymers[41] with or without side chains. The main difference between polythiophene and PhEtTh materials lies in the fact that the monomer of PhEtTh, which is a donor acceptor copolymer, has a significant dipole moment that originates from the charge transfer of 0.14 electrons from thiadiazole to benzene ring. On the other hand, such a strong dipole moment in not present in polythiophenes. These dipoles then introduce long range electrostatic potential which is responsible for band gap reduction.

Reduction of the band gap by electrostatic disorder can be understood from a simple one dimensional model (which is a special case of the toy model from Section 2) where on-site energies have a Gaussian distribution with standard deviation σ and electronic coupling t is present between nearest neighbors only. In Figure 1b,c (bottom panel) we present the DOS and the localization length (obtained by averaging of 25 000 different realizations of the system consisting of 100 sites) for such a model for two values of the σ/t ratio. As seen from the figure, when this ratio increases, localized states deeper in the band gap start to appear and consequently the band gap is reduced. However, one should have in mind that polymers where this effect is pronounced also have a rather poor mobility due to wide DOS tail and are therefore not suitable for any practical applications in electronics. Consequently, for electronic applications one should generally avoid polymers with strong built-in dipole moments within the monomer.

4.2. Thermal Disorder in Ordered Conjugated Polymers and Small Molecules

As pointed out in Section 2, the effects of thermal disorder may be significant in ordered conjugated polymer materials. This expectation comes from the weakness of interchain van der Waals bonding and the possibility of monomer rotation around the bonds that connect them (torsions) at finite temperature. Thermal disorder in ordered conjugated polymer materials originates both from disorder in the shape of main (backbone) chains and alkyl side chains. Wave functions of relevant electronic states are localized dominantly on the main chains. Therefore, disorder in main chains, which includes variations in torsion angles between thiophene rings and the displacements of the entire chains, directly affects the localization length of wave functions. On the other hand, the effect of side chains on the electronic structure is not that transparent. Disorder in the shape of side chains produces spatial variations of the electrostatic potential on the main chains, which subsequently affect the electronic structure.

The effects of thermal disorder on electronic structure of crystalline region of P3HT were investigated using the atomic structures of P3HT at a temperature of 300 K generated from MC simulations. Crystalline P3HT may exhibit the structure where main chains are aligned and the structure where these are mutually shifted by half a unit cell length in the main chain direction.[24] Below we will show the results for the shifted structure which is more energetically favorable,[24] while one expects qualitatively the same results for the aligned structure.

The isolated effect of disorder in side chains was investigated first by keeping main chains rigid during MC simulations. Then, the simulations were repeated allowing disorder in main chains as well. During the simulations the bond lengths and bond angles were kept constant, since their variations have only a slight effect on the electronic structure. Electronic structure calculations were performed using the CPM and the OFM. Small molecules consisting of three neighboring thiophene rings (trimers) were used as fragments in the OFM.

Effects of thermal disorder on electronic structure of P3HT were quantified by calculating the DOS and the wave function

localization length for ten highest states in the valence band, which cover the relevant spectral region of around 0.5 eV. The calculation was repeated for 100 different random realizations of the atomic positions for the system that consists of 10 chains, each 10 thiophene rings long.

Electronic DOS, total localization length and the localization length in the π–π stacking direction for the structures with disorder in side chains only and disorder in both main and side chains are shown in **Figure 6**. Results indicate that disorder in side chains has a relatively weak effect on the electronic structure. In this case, DOS contains several peaks (Figure 6a). These peaks correspond to the energies of the ideal crystalline structure, which are also shown for reference. On the other hand, when both types of disorder are present, DOS has a wider distribution of energies (Figure 6d).

We will consider the states with a value of localization length L less than 15, as localized states because all the states within first 0.2 eV from the top of the valence band have L smaller than 15 (see Figure 6e). In the structures with disordered side chains, most of the states are delocalized (Figure 6b). When both main and side chains are disordered, both localized and delocalized states exist (Figure 6e) but all states are localized in the spectral region of 0.2 eV below the highest state. Qualitatively similar results were obtained in amorphous P3HT[55] and from other calculations in ordered polymers.[53,61] From the comparison of the results for the structure with disorder in side chains only and the structure with disorder in both main and side chains, one can conclude that disorder in main chains is mainly responsible for the localization of charge carriers in ordered P3HT.

Charge transport in ordered polymers takes place along the main chain and the π–π stacking direction. Therefore, the localization length in the π–π stacking direction is also of particular interest. It can be considered as the number of different chains that a state is localized on. Localization length in the π–π stacking direction L_b was calculated using a similar formula as for the total localization length, with a redefinition of the expansion coefficients in such a manner that they refer to chains, instead of fragments. The energy dependence of L_b is qualitatively similar as the energy dependence of L (Figure 6c,f). In the case when both types of disorder are present, the highest states in the valence band have the values of L_b around 2. These states are predominantly localized on two neighboring chains due to significantly high electronic coupling between the chains. The wave function of the HOMO state in that case is shown in **Figure 7**b. On the other hand, when the disorder in side chains only is present, the wave functions are delocalized among a larger number of chains, as can be seen from Figure 6c and from the wave function of HOMO state shown in Figure 7a.

With the presented results, one can build a detailed picture on the role that the constituents of the polymer material have when the effects of thermal disorder are concerned. Side chains create a disordered electrostatic potential which leads to some degree of localization in the π–π stacking direction. Although these chains are flexible and have a rather disordered shape, their effect is not very strong because charge transfer between C and H atoms is small and therefore the electrical dipoles that create the electrostatic potential are weak. The dominant cause of localization then comes from disorder in the shape of main chains which has a strong effect both on the intrachain and interchain electronic coupling. Interestingly, the interchain electronic coupling remains sufficiently strong to delocalize the carrier over two chains.

Other simulations of thermally disordered polymers also lead to the results that are consistent with parts of this picture. It was demonstrated elsewhere[61] that electronic states on a single polythiophene main chain, in the absence of side chains exhibit localization. The localization of the states on a single chain of the PBTTT polymer lamella (where side chains were not included in the calculation) was predicted from calculations in the literature.[53]

The importance of thermal disorder in small molecule based organic crystals is now well appreciated[33] and will be only briefly discussed here. Its effects have been mostly studied within an one dimensional model where electronic coupling between the molecules n and $n+1$ depends on the displacements of these molecules u_n and u_{n+1} as $t(u) = t\left[1+\alpha(u_{n+1}-u_n)\right]$.[33,62,63] In Figure 1b,c (top panel) we present the DOS and the localization length for such a system consisting of 100 sites, obtained by averaging over 25 000 realizations of the system, with atomic displacements from the Gaussian distribution with standard

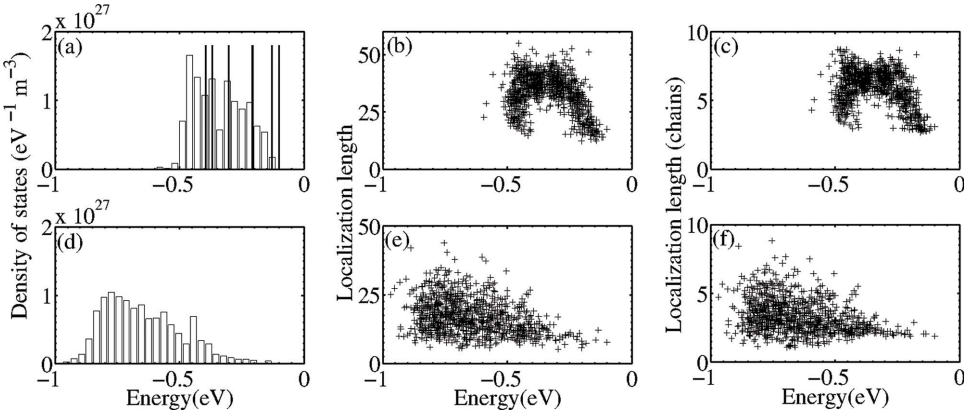

Figure 6. DOS for a) structures with disorder in side chains only and d) structures with disorder in both main and side chains; total localization length for b) structures with disorder in side chains only and e) structures with disorder in both main and side chains; localization length in the π–π stacking direction for c) structures with disorder in side chains only and f) structures with disorder in both main and side chains.

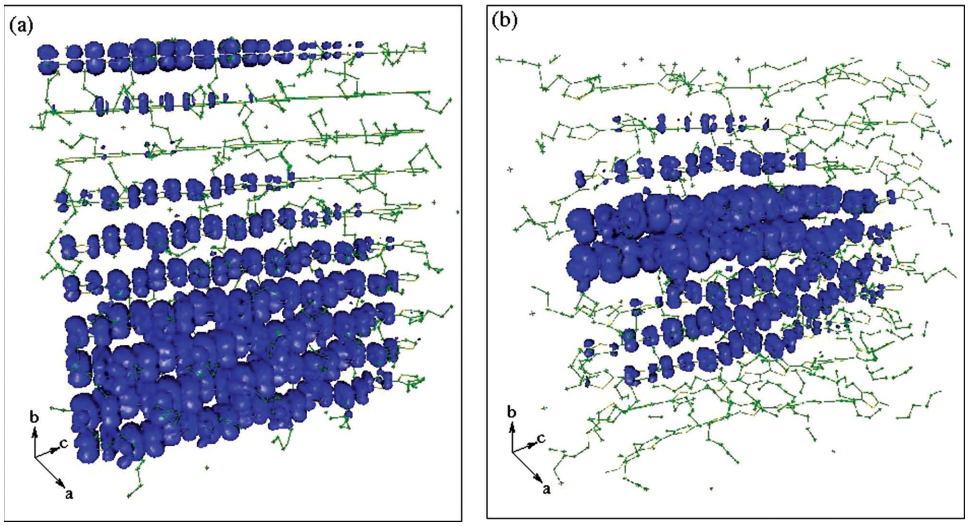

Figure 7. Isosurfaces of wave function moduli squared for HOMO state of P3HT with a) disorder in side chains only and b) disorder in both main and side chains. Isosurfaces correspond to the probability of finding a hole inside the surface of 90%.

deviation $\sigma = \sqrt{\frac{2\lambda k_B T}{t\alpha^2}}$, where T is the temperature and $\lambda = 0.1$. As can be seen from the figure, the presence of localized states near the band edge is a feature of this class of systems, while the states further away from the band edge are less localized. The increase of temperature leads to a wider tail in the DOS (see top part of Figure 1b) and to better localization of the states away from the band edge (see top part of Figure 1c). In the calculations performed starting from realistic atomic structure from MD snapshots and using the CPM and OFM to perform electronic structure calculations the presence of localized states at the band edge is also obtained.[38,64]

4.3. Grain Boundaries in Polycrystalline Organic Semiconductors Based on Small Molecules

Organic thin films based on small molecules are typically polycrystalline. It implies that they contain grain boundaries which separate the grains with different crystalline orientations. Grain boundaries are considered to be the most limiting intrinsic factor for charge carrier transport.[18,20,21,65–67] Nevertheless, the precise way in which they affect the electronic properties is not well understood. Quite a few works suggest the presence of trap centers at the boundaries.[18,19,21,65,68–71] The trapping of carriers at these centers leads to the drop in charge carrier mobility. On the other hand, there are suggestions that grain boundaries act as barriers for charge carriers, which inhibit the transport across the boundary.[72,73] Therefore, detailed electronic structure calculations are required to gain better understanding of the effect of grain boundaries.[71]

Initial atomic structure used in the simulation consists of two joined naphthalene crystalline grains with different crystalline orientations. Low-angle grain boundaries (misorientation angles from 5° to 20°) are most relevant since the calculations indicate that the energy of the structure increases as the angle of misorientation between the grains increases. Structures were optimized using MC simulations. Simulations are firstly performed at a finite temperature of 300 K and subsequently cooled down to 0 K, in order to exclude thermal disorder effects, which can additionally affect the electronic structure, as discussed in Section 4.2. Electronic structure calculations were performed using the CPM and the FSM. Since the electronic transport in such materials is two-dimensional, calculations were performed for single layers of polycrystalline naphthalene, each containing around 1400 atoms.

Wave functions of the electronic states at the top of the valence band for the system consisting of two crystalline grains with a misorientation angle of 10° are shown in **Figure 8**. By inspecting the isosurfaces for the presented states, one can notice three types of states: 1) states localized on two molecules at the boundary (Figure 8a); 2) other states localized at the boundary (Figure 8b), and 3) delocalized states (Figure 8c).

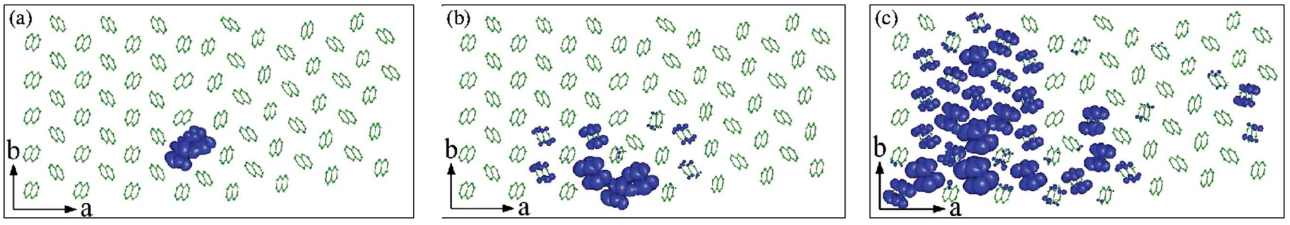

Figure 8. Isosurfaces of wave function moduli squared of the a) HOMO, b) HOMO-3, and c) HOMO-9 state of naphthalene grain boundary with misorientation angle of 10°. Isosurfaces correspond to the probability of finding a hole inside the surface of 90%.

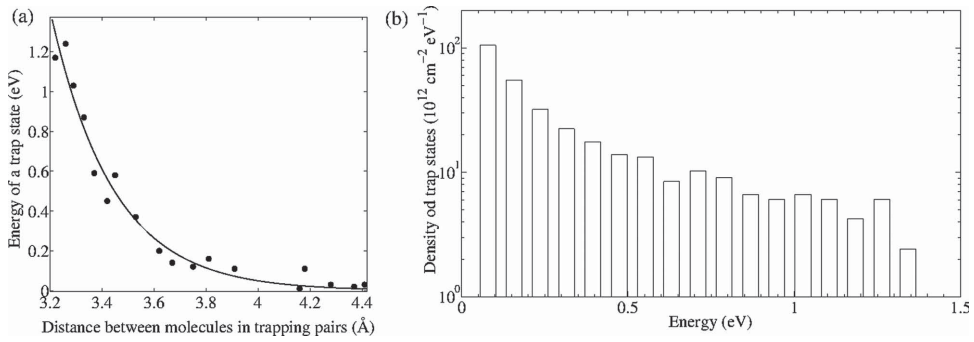

Figure 9. a) The dependence of the energy of trap states at the grain boundary on the distance between molecules which form the traps. The data obtained from all simulated systems are presented in the figure. Energies of the trapping states are defined with the top of the valence band as a reference level. b) Density of trap states for the system of two naphthalene crystalline grains with misorientation angle of 10°.

Results for other simulated systems are qualitatively the same. The highest states are always localized on molecule pairs at the boundary. Molecules in such pairs have mutual distance significantly smaller than the distance between neighboring molecules in a crystal. States created by these pairs can be very deep in the band gap, even more than 1 eV above the band edge. It is well-known that the decrease in the distance between the molecules increases the electronic coupling between them.[74] Therefore, higher electronic coupling between molecules at the boundary is responsible for the creation of the trap states in the band gap. Other localized states produce shallow traps, with the depth of up to 0.1 eV. Delocalized states start to appear at certain energy where the energy spectrum becomes continuous. Such states exist in a single crystal and they are not induced by a boundary. However, our results indicate that delocalized states are mostly localized at one side of the boundary (as in Figure 8c). For such states, grain boundary acts as a barrier.

Simulation results indicate that the energy of a trap state is strongly correlated to the distance between molecules which form the trap, as shown in **Figure 9**a. The exponentially decreasing function gives the best fit to this dependence. Additionally, the changes in the distances between molecules in trap centers after the atomic relaxation in MC simulation are not larger than 0.1 Å. Therefore, one can predict the energy of a trap state without MC simulations and electronic structure calculations, only by using the distance between the molecules and the fitting function. This method produces an error of around 0.1 eV. Using this approach, the density of trap states for large grain boundaries can be calculated. In Figure 9b the density of trap states for large grain boundary (around 30 nm) with misorientation angle of 10° is given.

The features obtained from a detailed atomistic simulation can largely be understood from a simple model of a grain boundary. We consider a special case of the model given by Equation 1–3 where the system consists of 100 sites arranged on a line. Electronic coupling between neighboring sites is t, except for the coupling between the two middle sites which is given by a uniform random number between 0 and $2t$. Different electronic coupling between the middle sites models the effect of the grain boundary on electronic properties. In Figure 1b,c (middle panel) the DOS and the dependence of the localization length on energy obtained by averaging the results over 25 000 different realizations of the system are presented. The presence of localized states within the band gap of the material induced by the grain boundary is evident from the figures.

5. Electronic Transport

5.1. Amorphous Polymers

Understanding the relationship between the atomic structure of the material and its electrical properties is a highly challenging task. This is the case in particular for disordered polymers where there is no periodicity of the atomic structure that can be exploited. The details of the atomic structure are also not very well known. In addition, specialized and efficient methods are required to perform electronic structure calculations on large supercells that are needed to extract sufficient statistics about the electronic properties of disordered materials.

For these reasons, phenomenological approaches were typically used to model electrical transport in disordered organic materials. In these approaches, one assumes that the system consists of a set of sites, characterized by their energy and the spatial position. Charge carrier transport in such a system then takes place by hopping between these sites. The energies of sites are drawn from a predefined distribution such as the Gaussian or the exponential distribution. The most usual assumptions about the spatial positions of sites are that they are located on cubic lattice or that they are distributed randomly in space with a uniform distribution. The probability of carrier hopping from site i to an unoccupied site j in a unit of time is often assumed to take the Miller-Abrahams form $W_{ij} = W_0 \exp\left(-2R_{ij}/a\right)$ for downward transitions $(E_i \geq E_j)$ and $W_{ji} = W_{ij} \exp\left[-\left(E_i - E_j\right)/(k_B T)\right]$ for upward transitions (E_i/E_j). In previous equations, R_{ij} is the spatial distance between sites i and j, E_i is the energy of the carrier at site i, T is the temperature, while W_0 and a are constant coefficients in the exponentially decaying dependence of W_{ij} on R_{ij}. Such a model of electronic transport in disordered materials (when Gaussian DOS is assumed) is usually referred to as the "Gaussian disorder model".[75–78]

Due to the simplicity of the phenomenological approaches, these have become quite popular and they are often used to fit the experimental data, such as the dependence of mobility on temperature. Nevertheless, the shortcomings of these models

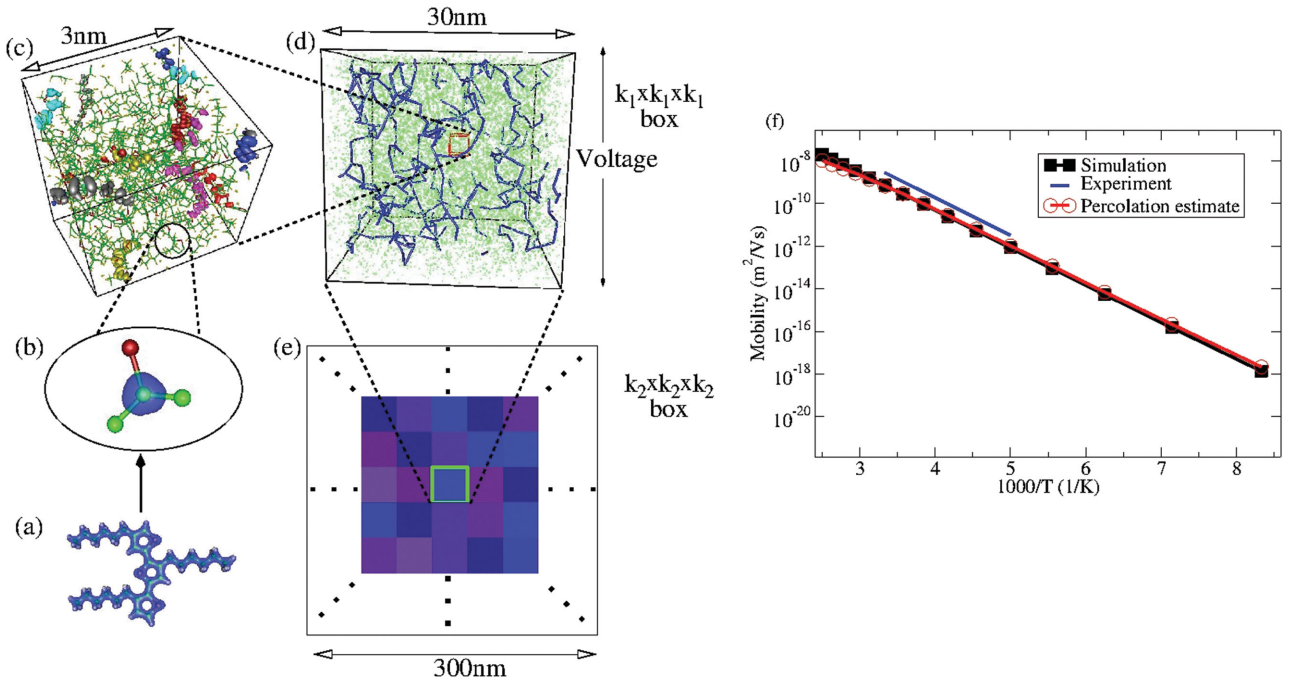

Figure 10. Schematic representation of the multiscale procedure for simulation of charge transport in amorphous polymers: a) Atomic structure and electronic charge density of the small molecule used to generate the charge density motifs; b) Charge density motif assigned to one atom type in the system; c) The atomic structure and valence band wave function isosurface plots of the disordered polymer; d) Transport sites (green dots) and the relevant current paths through the material (blue lines) when the voltage is applied in the direction indicated; e) Continuum system at the final length scale; f) Temperature dependence of hole mobility in P3HT polymer obtained from the described procedure (squares), its comparison to experimental data from the literature[87,88] (solid line) and the estimate from percolation theory (circles).

are the lack of clear physical meaning of the concepts and parameters of the model and the lack of their relation to atomic structure of the material. For example, is not clear what the "sites" in the model correspond to in the real physical system. If it is assumed that the sites are distributed on a cubic lattice, it is questionable how to choose the lattice constant. Miller-Abrahams form for the transition rates was derived originally in the context of carrier hopping between impurities in solids.[79] If the wave function of a carrier on the impurity is spherical, then the overlap between the wave functions on the two impurities decays exponentially with the distance between the impurities and the assumption of Miller-Abrahams form is quite plausible. On the other hand, as seen in Figure 3a, the wave functions in disordered polymers have a quite different, elongated shape, and it is questionable if such an expression is applicable to them.

Due to mentioned shortcomings of phenomenological models, the development of an approach that would link the atomic structure of the material to its electrical properties is of great interest. We have developed such an approach that links the quantities on four length scales to obtain the macroscopically measurable property of the material, such as the charge carrier mobility.[30] The whole approach in its present form focuses on homogeneous strongly disordered materials. Presently, it cannot be directly applied to more complex materials that contain both disordered and ordered phases. Nevertheless, the parts of the approach and the ideas from the approach will certainly be helpful in the development of the approach for treatment of more complex materials.

At the smallest length scale (on the order of few angstroms), we perform DFT calculations on small molecules (shown in **Figure 10**a) to obtain the motifs used in the CPM (shown in Figure 10b).

At the next length scale (Figure 10c), we perform electronic structure calculations to obtain the energies and wave functions of charge carriers. The atomic structure of the polymer material at this length scale is obtained from classical MD using a simulated annealing procedure, as described in Section 3. Electronic structure calculations at this length scale are performed using the CPM which constructs the single particle Hamiltonian, which is then diagonalized either using the FSM or the OFM. At this length scale, we also calculate the charge carrier hopping rates between the states as

$$W_{ij} = \pi \sum_{\alpha} \frac{\left|M_{ij,\alpha}\right|^2}{\omega_\alpha} \left[(N_\alpha + 1)\delta\left(E_i - E_j - \hbar\omega_\alpha\right) + N_\alpha \delta\left(E_i - E_j + \hbar\omega_\alpha\right) \right] \quad (6)$$

where W_{ij} is the probability of hopping from state i to state j in a unit of time, E_j and E_j are the energies of states, $\hbar\omega_\alpha$ is the energy of phonon of mode α, N_α the number of phonons in that mode given by the Bose-Einstein distribution, $M_{ij,\alpha}$ and is the electron-phonon coupling constant between electronic states i and j due to phonon mode α. The phonon modes are obtained from the same classical force field that was used in MD simulations by diagonalizing the corresponding dynamical matrix. The electron-phonon coupling constants are obtained

from the CPM by calculating the change in the single particle Hamiltonian due to displacements according to a given phonon mode.

One should pay particular attention to the size of the simulation box at this length scale. It is absolutely necessary that it is larger than the localization length of strongly localized wave functions (otherwise the obtained wave functions would not be representative of wave functions in real system). On the other hand, its size is limited by the computational cost of electronic structure calculations. With the combination of CPM and OFM, we can calculate the system that contains on the order of 10 000 atoms which corresponds to box size on the order of 5 nm. Such a size is sufficient to obtain reliable wave functions. Nevertheless, with such a calculation we obtain several tens of wave functions in the spectral region within ≈0.5 eV, which is the spectral region of interest for electrical transport properties. This is too little states for the extraction of macroscopic parameter of the material such as the charge carrier mobility because a different random realization of the system would lead to a completely different mobility. For this reason, we need to go to the next length scale to simulate charge carrier transport. To get sufficient information to construct the system on the next length scale, we repeat the calculation on this length scale many times for different random realizations of the system.

At the next length scale, we consider the system as a set of sites among which the charge carriers are hopping [shown in Figure 10d]. The simulation box is constructed by putting together $k_1 \times k_1 \times k_1$ (typically $k_1 = 10$) small boxes whose size is equal to the size of the box on the previous length scale. The positions and energies of the sites in each of the small boxes are taken from the simulation on the previous length scale, by randomly choosing one of the realizations of the system on the previous length scale and randomly rotating it in space. It is well known[86] that the conductance at low electric fields for hopping transport is equal to the conductance of a network of resistors constructed by connecting sites i and j with a resistor of conductance $G_{ij} = \frac{e^2}{k_B T} n_i W_{ij} = \frac{e^2}{k_B T} n_j W_{ji}$, where n_i is the occupation of site i. The hopping rates between the sites from the same small box are directly available from the simulation on the previous length scale, while the hopping rates between different boxes are approximated in a manner that retains their statistical averages.[30] The calculations for different realizations of the system at this length scale (where the simulation box size is typically on the order of 20–30 nm) still yield different mobilities, which vary within one to two orders of magnitude depending on temperature.

To obtain the final mobility representative of the mobility of bulk amorphous polymers, we therefore need to go one length scale further (shown in Figure 10e). At this final length scale, we consider the system as the continuum with spatially varying conductivity. The simulation box is again constructed by putting together $k_2 \times k_2 \times k_2$ (with typical $k_2 = 10$) small boxes whose size is equal to the box size on the previous length scale. Each of these boxes is considered as a uniform but anisotropic conductor whose conductivity is determined from the result on the previous length scale. The mobility in direction d (where $d = x$, y or z) is calculated as $\mu_d = G_d / (enL)$, where G_d is equivalent conductance in direction d, n is the concentration of carriers, and L is the box size dimension at this length scale. We will present the results for the limit of low carrier concentration, when G_d is proportional to n and the mobility is independent of carrier concentration. At this length scale (with the box size on the order of 300 nm), one finally obtains the mobility which is nearly independent on random realization of the system. It is interesting to note that a very similar result for the mobility would be obtained if one simply took the geometrical average of the mobilities obtained at the previous length scale instead of performing the simulation of the continuum system at this length scale.

Our approach overcame the issue of insufficiently large size of the box used in electronic structure calculations through the construction of larger system on the next length scale from the information obtained on previous length scale. At each length scale we check if the simulation box is big enough by repeating the calculation on that length scale for different random realizations of the system. If the conductance obtained for different realizations significantly varies, this gives an indication that the system is not large enough and that one needs to go one length scale further. The information gained from repeated calculations is then used to construct the system on the next length scale. At the final scale the variations of the conductance for different realizations of the system are small which indicates that the simulation box on that length scale is large enough. An interesting alternative to our approach was discussed in another study.[80] That approach is based on the fact that at higher temperatures the carriers visit a significantly larger number of sites during the transport and for that reason smaller system size is required to obtain the mobility at higher temperatures than at low temperatures. One can then calculate the mobility of the small system at high temperature and use it to extrapolate to the mobility of bulk at low temperatures as described elsewhere.[80]

Temperature dependence of the mobility of amorphous P3HT polymer is presented in Figure 10f. We find that the mobility is thermally activated and its temperature dependence fits well the expression $\mu(T) = \mu_0 \exp\left[-E_A / (k_B T)\right]$, with activation energy of $E_A = 347\,\text{meV}$ and the mobility at room temperature of $\mu(T = 300\text{K}) = 0.71 \times 10^{-9}\,\text{m}^2\,\text{V}^{-1}\,\text{s}^{-1}$. On the other hand, experimental results[87,88] yield $E_A = 350\,\text{meV}$ and $\mu(T = 300\text{K}) = 2.8 \times 10^{-9}\,\text{m}^2\,\text{V}^{-1}\,\text{s}^{-1}$. Therefore, the simulation results are in quite good agreement with experiment since the correct value of activation energy is obtained and the correct order of magnitude of the mobility.

The fact that we needed to perform the simulation at several length scales up to the scale of hundreds of nanometers is a direct consequence of disordered nature of the system. For a disordered system the length scale beyond which the system starts behaving as bulk is much larger than for ordered systems. The fact that we needed to extend our simulation to the 100 nm length scale indicates that this is exactly the length scale beyond which the portion of the disordered polymer material behaves as bulk when electrical transport characteristics are concerned. All devices of smaller size would exhibit different characteristics for different realizations of the device.

In ordered materials, current is uniformly distributed through the material (at the length scale beyond the

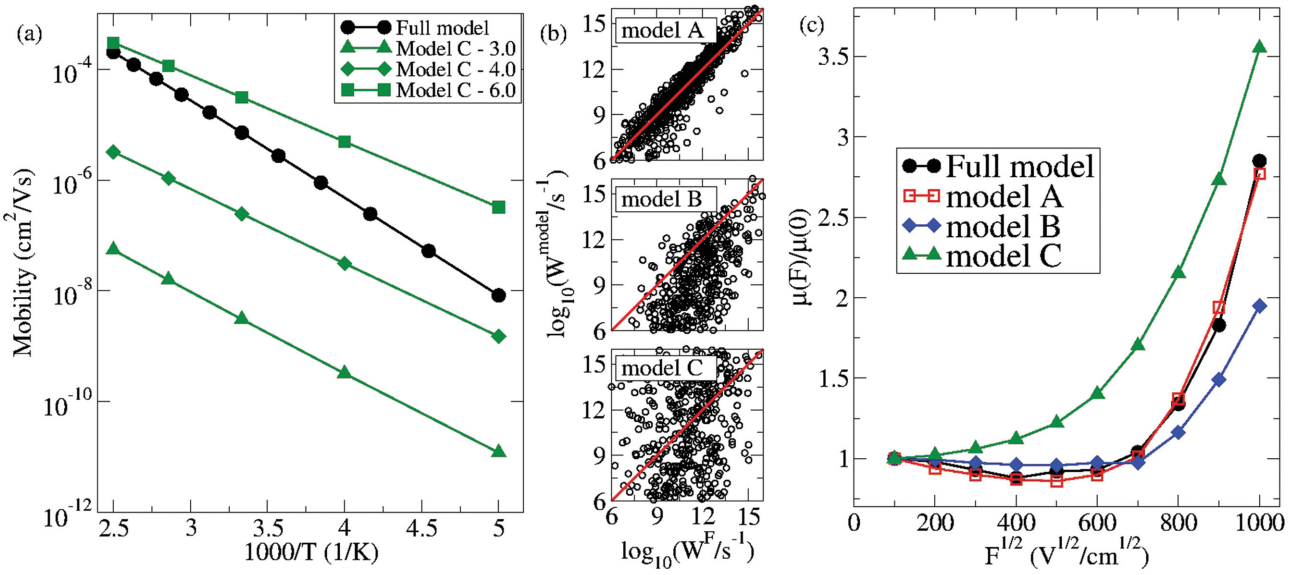

Figure 11. a) Temperature dependence of the mobility in the full model and using the model with Miller-Abrahams rates (model C). The value of the parameter a (in Angstroms) in model C is indicated in the legend. b) The comparison of hopping rates in different models with the ones obtained in the full model. c) Electric field dependence of the mobility at room temperature within different models. The parameters of the models A–C were chosen to fit the temperature dependence of the mobility from the full model.

interatomic distances). On the other hand, this is not the case in disordered materials and it is very interesting to inspect the current paths in the material. These are presented in Figure 10d. In the figure, the sites where the current is larger than 5% of the maximal current in the system are connected with lines. The currents between these sites contribute to at least 75% of the total current at each cross section perpendicular to the direction of the applied voltage. For these reasons the current paths shown in the figure can be considered as relevant current paths in the material. From visual inspection of the figure, one can notice that the overall current flow is determined by a relatively small number of current paths, which gives an indication that percolation theory might be appropriate for the description of current flow in the system.

Percolation theory often gives a good description of transport properties in disordered systems. In the context of our system, modeled as a conductor network, percolation theory suggests that the current paths are formed at the place where a continuous network of connections that spans the whole system can be formed, where connections are formed between each two sites with a conductance larger than some critical conductance G_c. The criterion that can be used to check if the continuous network that spans the system was formed is that the number of connections per site is larger than some critical value a_c. We find that the conductivity of the material can reliably be estimated (see Figure 10f) from percolation theory as $\sigma = G_c / L_c$, where G_c was determined from $a_c = 3.2$ and L_c is taken to be equal to characteristic distance between the sites $L_c = 1.5$ nm. Further confirmation of the appropriateness of the percolation theory comes from the fact that all resistors in the relevant current path indeed have $G_c > G_c$.

In our approach, we calculate the transition rates between the states using a rather detailed formula given by Equation 6 which includes the coupling to all phonon modes. To calculate these rates, one needs to calculate the wave functions, the phonon modes, and the electron-phonon coupling constants, which is computationally very demanding. On the other hand, widely used Miller-Abrahams expression contains only the energies of electronic states and the distance between the sites. It is therefore of great interest to determine to what extent can the full expression for transition rates (Equation 6) be simplified. Such an insight would be helpful to reduce the computational cost of the described multiscale procedure. Moreover, this insight will help us to address an important question about the main physical quantities that determine the charge carrier mobility. While it is widely understood that the mobility is strongly dependent on electronic DOS, one can imagine that the phonon DOS, the details of wave functions overlaps, as well as the details of the phonon modes could be important as well.

The hopping rates in the system, calculated using Equation 6 that takes into account the interaction with all phonon modes largely deviate from the traditional Miller-Abrahams form (bottom panel in **Figure 11**b). The main reason for this deviation is that the wave functions have a strongly anisotropic shape and therefore their overlap does not simply decay exponentially with distance between them.

Next, we would like to understand the consequences of the differences between the rates obtained using Miller-Abrahams form and the full model on electrical transport. The comparison of the mobilities, shown in Figure 11a, indicates that for a physically realistic prefactor $W_0 = 10^{14}\,\mathrm{s}^{-1}$, regardless of the values of the parameter a, the slope of the dependence is different. Therefore, the model with Miller-Abrahams hopping rates cannot reproduce the results of the detailed model, regardless of the choice of parameters, as long as they are physically realistic. We find that the dependence can be reproduced only with physically unrealistic pair of parameters $W_0 = 6.3 \times 10^{20}\,\mathrm{s}^{-1}$ and $a = 2\,\text{Å}$.

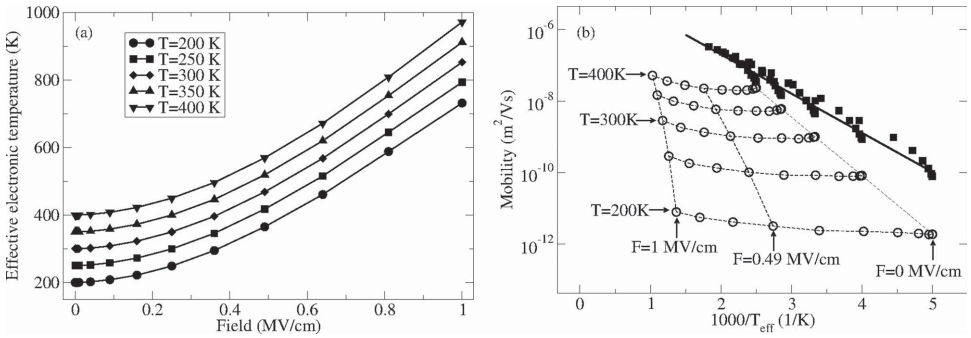

Figure 12. a) Dependence of effective electronic temperature on electric field for different values of lattice temperature. b) Dependence of mobility on effective electronic temperature in full model (circles) and in model C with $a = 6\,\text{Å}$ (squares).

While we have shown that the model with Miller-Abrahams rates yields quantitatively significantly different results than the full model, we demonstrate another example where the model with Miller-Abrahams rates gives even a qualitatively different result. This result concerns the importance of the concept of effective electronic temperature for the system in a finite electric field. The effective electronic temperature is defined from the fit of charge carrier distribution to a Boltzmann distribution and its dependence on electric field for several lattice temperatures is shown in **Figure 12**a. An important question about the effective electronic temperature is whether it can be used to replace the joint effect of electric field and lattice temperature. If this is the case, then the dependence of mobility on electronic temperature falls into one curve. As seen from Figure 12b we reproduce the results of earlier studies that this is the case in the model with Miller-Abrahams rates,[81,82] while we find that this is not the case in the full model.[83] Consequently, the model with Miller-Abrahams rates yields a qualitatively different conclusion related to the importance of effective electronic temperature than a realistic model.

Having established that the model with Miller-Abrahams rates can yield the results which are both qualitatively and quantitatively different, we would like still to find a model which is simpler than our detailed model, and yet accurate enough. We therefore introduce several approximations to the hopping rate expression. In first approximation we assume that the electron-phonon coupling constant is simply proportional to the overlap of the wave function moduli $S_{ij} = \int d^3\mathbf{r}\left|\psi_i(\mathbf{r})\right|\left|\psi_j(\mathbf{r})\right|$, which then yields the model that we call model A where the downward hopping rate is given by the expression

$$W_{ij}^{\mathrm{A}} = \beta^2 S_{ij}^2\left[N\left(E_{ij}\right)+1\right]D_{\mathrm{ph}}\left(E_{ij}\right)/E_{ij} \tag{7}$$

where β is the proportionality factor between electron–phonon coupling constants and wave function moduli overlaps, $D_{\mathrm{ph}}\left(E_{ij}\right)$ is the phonon DOS normalized to satisfy $\int_0^\infty \mathrm{d}E D_{\mathrm{ph}}(E) = 1$ and $E_{ij} = \left|E_i - E_j\right|$. Further simplification can be made by assuming that the wave function overlap decays exponentially with distance which yields model B where the downward hopping rate is given as

$$W_{ij}^{\mathrm{B}} = \beta^2 \exp\left(-2R_{ij}/a\right)\left[N\left(E_{ij}\right)+1\right]D_{\mathrm{ph}}\left(E_{ij}\right)/E_{ij} \tag{8}$$

Finally, if all the energy dependence is ignored in the last expression, one gets the model C which is the Miller-Abrahams expression. The free parameters in all these models can be adjusted to fit the temperature dependence of the mobility in the limit of low carrier concentration (albeit sometimes with physically unrealistic set of parameters), but the question is whether they can then be used to predict other properties. One of these properties is the electric field dependence of the mobility in the limit of low carrier concentration. We find that only model A can reproduce the mobility from the full model, see Figure 11c. The microscopic origin of this lies in the fact that hopping rates in model A still quite decently reproduce the hopping rates from the full model, which is not the case for models B and C, see Figure 11b.

We also note in passing that the mobility generally increases with an increase in electric field (Figure 11c), while for models A and C it exhibits a slight decrease with increasing field at low electric fields (negative differential conductance). It has been argued[77,84,85] that negative differential conductance obtained in some experiments and simulations is an artefact of the time-of-flight and kinetic Monte Carlo mobility extraction procedure which ignores the presence of diffusion current. Due to only slight negative differential conductance obtained in our simulation, it is difficult to establish with certainty if negative differential conductance is present or not.

Having established that the model A captures the most important features of the hopping rates, we can identify what are the physical quantities that determine the transport. In addition to electronic DOS, the phonon DOS is important since it appears explicitly in our model for hopping rates. Details of the wave function overlaps are important as well. On the other hand, the fact that we could simplify our initial expression to this model implies that the details of the phonon modes are not of primary importance.

Therefore, these results suggest than in addition to the widely appreciated fact that electronic DOS is important for electrical transport, the wave function overlap and the phonon DOS are also of importance.

5.2. Other Organic Semiconductors

There is a consensus that charge transport in amorphous polymers takes place by hopping between the states localized due to static disorder present in the material. On the other

hand, thermal disorder present in ordered organic materials is of dynamic nature and its influence on electrical transport properties is less transparent. This is probably one of the main reasons why a consensus about the mechanism and nature of charge transport in ordered organic materials has not been reached yet. In this subsection, we will discuss the results obtained in previous sections in view of their consequences for electrical transport properties.

5.2.1. Small Molecule Based Organic Crystals

Electrical transport in small molecule based organic crystals has been modeled using a variety of approaches. A popular approach due to its relative simplicity is based on Marcus theory of charge transfer.[31] In such an approach, the crystal is considered as a set of molecules and charge transfer rates between any two molecules are evaluated from semiclassical Marcus theory or its generalizations. The mobility through the material is then calculated from Master equation or kinetic Monte Carlo approach. However, one should be careful regarding the limitations of this approach.[37,89] Such a methodology ignores coherent propagation of the carrier between the molecules and it assumes that electronic coupling between the molecules is just a perturbation. As a result, it gives thermally activated dependence of mobility on temperature, which is in contrast to experimental results from the literature.

Other set of approaches[90–92] is based on the canonical transformation of the Hamiltonian to a new basis where electron-phonon interaction acts just as a perturbation. These approaches can yield the mobility that decreases with an increase of temperature. However, due to the approximations used in the formalism (including often neglecting of non-local electron-phonon coupling), the reliability of these approaches is still the subject of investigation.

As pointed out in Section 4.2, the eigenstates of the Hamiltonian obtained by freezing the atomic coordinates at a certain moment of time (so called adiabatic states) exhibit localization. However, as the time evolves the Hamiltonian changes and it is not clear whether the carrier will remain in the new adiabatic state or make a transition to some other state. An approach that transparently takes into account the dynamic localization of carriers combines classical MD with time propagation of the Schrodinger equation according to the Hamiltonian that depends on atomic coordinates obtained from MD.[33,93] This approach is referred to as Ehrenfest dynamics. In simulations based on Ehrenfest dynamics,[33] experimentally observed trend of mobility that decreases with increasing temperature was obtained. Given the presence of localization of band edge states (and delocalization of states further away from the band edge), this trend is something that may not be expected since higher temperature should promote the carriers from localized to delocalized states and improve the transport. However, one should note that the spectral region with localized carriers is rather narrow (smaller than k_BT at room temperature, see Figure 1b,c, top parts) and that even a relatively small temperature is sufficient to promote the carriers to delocalized states. Therefore the temperature dependence of the mobility is likely determined by other effects, such as the decrease of the localization lengths with an increase of temperature. One should also note that Ehrenfest dynamics is known to suffer from the issue that the mean energy of carriers is substantially larger than the correct one,[38,94] Fewest switches surfaces hopping method is a modification of Ehrenfest dynamics that solves this issue.[95] In simulations based on this approach[38] with the Hamiltonian obtained from CPM, it was found that the transition from one adiabatic state to another takes place when the two adiabatic states cross each other and that these transitions dominantly determine the carrier transport. Another issue with approaches based on the combination of classical MD for the motion of nuclei and quantum evolution of electronic degrees of freedom is that the phonons are treated classically, which is an approximation whose validity has yet to be investigated. The range of validity of surface hopping approaches (in particular for high mobility materials with band like transport) also remains a topic for further investigation.[96]

5.2.2. Grain Boundaries in Small Molecule-Based Organic Crystals

Results for electronic structure of polycrystalline naphthalene, presented in Section 4.3, unambiguously confirm the presence of trap centers at the grain boundary. From the calculations, we have estimated that the number of trap states per unit of volume (assuming the size of the grains is 1 μm) is $N_t = 9\times10^{17}\,\mathrm{cm}^{-3}$, while the number of states in the valence band in naphthalene bulk is $N_v = 6.1\times10^{21}\,\mathrm{cm}^{-3}$. These estimates are in good agreement with previously reported results for density of trap states in similar materials.[18,65]

Since N_t is relatively significant in comparison to N_v, traps induced by grain boundaries are expected to have a significant affect on electronic transport, especially in devices which operate in low carrier density regime, such as light-emitting diodes and solar cells. In devices which operate in high carrier density regime, such as field-effect transistors, carriers fill the traps, which affects the transport only through electrostatic barriers created by trapped carriers.[66,68,69]

A detailed model of electrical transport at a single grain boundary has not yet been developed. One of the reasons for that is the lack of complete understanding of transport model in bulk crystals, which should certainly be an ingredient of the single grain boundary transport model. Since, as discussed in Section 4.3, the grain boundary acts somewhere as a trap, and somewhere as a barrier, the current flow through the boundary will be spatially nonuniform and one may expect that it contains very interesting physics.

5.2.3. Ordered Polymers

As shown in Section 4.2, in ordered polymers there is a spectral region within first 0.2 eV from the top of the valence band where only localized states exist. These states were found to be persistently localized in the sense that their position does not significantly vary during nanosecond timescales.[61] Previous results,[61] as well as our calculations, show that localization length does not vary significantly with temperature in the range from $100\,\mathrm{K}$ to $300\,\mathrm{K}$. On the other hand, temperature increase

supports hopping from localized to delocalized states.[97] Therefore, the promotion of carriers from localized to delocalized states in ordered polymers could be the reason for thermally activated transport, which was observed in such systems in mobility measurements.[98]

At this point, it is interesting to discuss the difference in the temperature dependence of the mobility observed in small molecule based organic crystals and ordered polymers. Both classes of systems exhibit a spectral region near the band edge where only localized states exist, which is followed by the region with more delocalized states. However, this spectral region is much wider in polymers, while it is so narrow in small molecule based crystals that a large number of carriers is present in delocalized states even at relatively small temperatures. On the other hand, in polymers significant activation energy is required to promote the carriers to delocalized states, which may lead to thermally activated transport.

6. Conclusion

With the help of atomistic simulations, one can currently get important insights into the wave function localization lengths and the electronic DOS for a variety of organic semiconductor structures, such as amorphous polymers, ordered polymer regions, small molecule based organic crystals and grain boundaries in organic crystals. In the case of amorphous polymers, which exhibit strong static disorder, these results can be directly used in combination with a multiscale approach to evaluate measurable macroscopic material properties, such as the charge carrier mobility. Atomistic multiscale simulations are then necessary to obtain quantitatively correct results, while in some cases even qualitatively correct results cannot be obtained without the use of such detailed simulations. In other organic semiconducting materials and structures, where the effects of dynamic disorder are of significant importance, the results of atomistic simulations give some indication about the nature of charge carrier transport. Further research is certainly needed to better understand the carrier transport mechanism in these materials which will presumably also lead to the development of methods for a better quantitative description of electrical transport. Moreover, simulation approaches described in this article certainly open the way to study complex structures exhibited in realistic organic materials—such as the interfaces between ordered and disordered regions in conjugated polymer based materials.

Acknowledgements

This work was supported by a European Community FP7 Marie Curie Career Integration Grant (ELECTROMAT), the Serbian Ministry of Education, Science and Technological Development (Project ON171017) and FP7 projects PRACE-3IP and EGI-InSPIRE.

Received: July 21, 2014
Revised: August 22, 2014
Published online: September 22, 2014

[1] H. E. Katz, J. Huang, *Ann. Rev. Mater. Res.* **2009**, *39*, 71–92.
[2] T. Ameri, P. Khoram, J. Min, C. J. Brabec, *Adv. Mater.* **2013**, *25*, 4245–4266.
[3] K.-J. Baeg, M. Binda, D. Natali, M. Caironi, Y.-Y. Noh, *Adv. Mater.* **2013**, *25*, 4267–4295.
[4] H. Dong, H. Zhu, Q. Meng, X. Gong, W. Hu, *Chem. Soc. Rev.* **2012**, *41*, 1754–1808.
[5] Y. Lin, Y. Li, X. Zhan, *Chem. Soc. Rev.* **2012**, *41*, 4245–4272.
[6] D. Briand, A. Oprea, J. Courbat, N. Barsan, *Mater. Today* **2011**, *14*, 416–423.
[7] M. D. Angione, R. Pilolli, S. Cotrone, M. Magliulo, A. Mallardi, G. Palazzo, L. Sabbatini, D. Fine, A. Dodabalapur, N. Cioffi, L. Torsi, *Mater. Today* **2011**, *14*, 424–433.
[8] J. Nelson, *Mater. Today* **2011**, *14*, 462–470.
[9] N. T. Kalyani, S. J. Dhoble, *Renew. Sust. Energ. Rev.* **2012**, *16*, 2696–2723.
[10] A. C. Arias, J. D. Mackenzie, I. McCulloch, J. Rivnay, A. Salleo, *Chem. Rev.* **2010**, *110*, 3–24.
[11] C. J. Brabec, J. A. Hauch, P. Schilinsky, C. Waldauf, *MRS Bull.* **2005**, *30*, 50–52.
[12] J. Rivnay, S. C. B. Mannsfeld, C. E. Miller, A. Salleo, M. F. Toney, *Chem. Rev.* **2012**, *112*, 5488–5519.
[13] A. Salleo, R. J. Kline, D. M. DeLongchamp, M. L. Chabinyc, *Adv. Mater.* **2010**, *22*, 3812–3838.
[14] R. Noriega, J. Rivnay, K. Vandewal, F. P. Koch, N. Stingelin, P. Smith, M. F. Toney, A. Salleo, *Nat. Mater.* **2013**, *12*, 1038–1044.
[15] T.-A. Chen, X. Wu, R. D. Rieke, *J. Am. Chem. Soc.* **1995**, *117*, 233–244.
[16] H. Sirringhaus, P. J. Brown, R. H. Friend, M. M. Nielsen, K. Bechgaard, B. M. W. Langeveld-Voss, A. J. H. Spiering, R. A. J. Janssen, E. W. Meijer, P. Herwig, D. M. de Leeuw, *Nature* **1999**, *401*, 685–688.
[17] R. A. Street, J. E. Northrup, A. Salleo, *Phys. Rev. B* **2005**, *71*, 165202.
[18] W. L. Kalb, S. Haas, C. Krellner, T. Mathis, B. Batlogg, *Phys. Rev. B* **2010**, *81*, 155315.
[19] G. Horowitz, M. E. Hajlaoui, *Adv. Mater.* **2000**, *12*, 1046–1050.
[20] S. S. Lee, C. S. Kim, E. D. Gomez, B. Purushothaman, M. F. Toney, C. Wang, A. Hexemer, J. E. Anthony, Y.-L. Loo, *Adv. Mater.* **2009**, *21*, 3605–3609.
[21] A. D. Carlo, F. Piacenza, A. Bolognesi, B. Stadlober, H. Maresch, *Appl. Phys. Lett.* **2005**, *86*, 263501.
[22] W. Warta, N. Karl, *Phys. Rev. B* **1985**, *32*, 1172–1182.
[23] M. E. Gershenson, V. Podzorov, A. F. Morpurgo, *Rev. Mod. Phys.* **2006**, *78*, 973–989.
[24] S. Dag, L.-W. Wang, *J. Phys. Chem. B* **2010**, *114*, 5997–6000.
[25] W. Xie, Y. Y. Sun, S. B. Zhang, J. E. Northrup, *Phys. Rev. B* **2011**, *83*, 184117.
[26] T. J. Prosa, M. J. Winokur, J. Moulton, P. Smith, A. J. Heeger, *Macromolecules* **1992**, *25*, 4364–4372.
[27] N. Kayunkid, S. Uttiya, M. Brinkmann, *Macromolecules* **2010**, *43*, 4961–4967.
[28] A. Maillard, A. Rochefort, *Phys. Rev. B* **2009**, *79*, 115207.
[29] G. R. Hutchison, Y.-J. Zhao, B. Delley, A. J. Freeman, M. A. Ratner, T. J. Marks, *Phys. Rev. B* **2003**, *68*, 035204.
[30] N. Vukmirović, L.-W. Wang, *Nano. Lett.* **2009**, *12*, 3996–4000.
[31] V. Coropceanu, J. Cornil, D. A. da Silva Filho, Y. Olivier, R. Silbey, J.-L. Bredas, *Chem. Rev.* **2007**, *107*, 926–952.
[32] L. Wang, G. Nan, X. Yang, Q. Peng, Q. Lia, Z. Shuai, *Chem. Soc. Rev.* **2010**, *39*, 423–434.
[33] A. Troisi, G. Orlandi, *Phys. Rev. Lett.* **2006**, *96*, 086601.
[34] A. Troisi, G. Orlandi, J. E. Anthony, *Chem. Mater.* **2005**, *17*, 5024–5031.
[35] K. D. Meisel, H. Vocks, P. A. Bobbert, *Phys. Rev. B* **2005**, *71*, 205206.
[36] S. S. Zade, M. Bendikov, *Chem.-Eur J.* **2008**, *14*, 6734–6741.

[37] A. Troisi, *Chem. Soc. Rev.* **2011**, *40*, 2347–2358.
[38] J. Ren, N. Vukmirović, L.-W. Wang, *Phys. Rev. B* **2013**, *87*, 205117.
[39] N. Vukmirović, C. Bruder, V. M. Stojanović, *Phys. Rev. Lett.* **2012**, *109*, 126407.
[40] M. P. Allen, D. J. Tildesley, *Computer Simulations of Liquids*, Clarendon Press, New York, USA **1987**.
[41] N. Vukmirović, L.-W. Wang, *J. Phys. Chem. B* **2009**, *113*, 409–415.
[42] P. Yang, E. R. Batista, S. Tretiak, A. Saxena, R. L. Martin, D. L. Smith, *Phys. Rev. B* **2007**, *76*, 241201.
[43] G. Zhang, Y. Pei, J. Ma, K. Yin, C.-L. Chen, *J. Phys. Chem. B* **2004**, *108*, 6988–6995.
[44] G. Zhang, J. Ma, J. Wen, *J. Phys. Chem. B* **2007**, *111*, 11670–11679.
[45] H.-C. Yang, C.-Y. Hua, M.-Y. Kuo, Q. Huang, C.-L. Chen, *Chem. Phys. Chem.* **2004**, *5*, 373–381.
[46] T. Qin, A. Troisi, *J. Am. Chem. Soc.* **2013**, *135*, 11247–11256.
[47] V. Ruehle, A. Lukyanov, F. May, M. Schrader, T. Vehoff, J. Kirkpatrick, B. Baumeier, D. Andrienko, *J. Chem. Theory Comput.* **2011**, *7*, 3335–3345.
[48] R. G. Parr, W. Yang, *Density-Functional Theory of Atoms and Molecules*, Oxford University Press, New York, USA **1989**.
[49] N. Vukmirović, L.-W. Wang, *J. Chem. Phys.* **2008**, *128*, 121102.
[50] A. Canning, L.-W. Wang, A. Williamson, A. Zunger, *J. Comp. Phys.* **2000**, *160*, 29–41.
[51] L.-W. Wang, A. Zunger, *J. Chem. Phys.* **1994**, *100*, 2394–2397.
[52] N. Vukmirović, L.-W. Wang, *J. Chem. Phys.* **2011**, *134*, 094119.
[53] T. Liu, A. Troisi, *Adv. Funct. Mater.* **2013**, *24*, 925–933.
[54] D. P. McMahon, A. Troisi, *Chem. Phys. Lett.* **2009**, *480*, 210–214.
[55] N. Vukmirović, L.-W. Wang, *J. Phys. Chem. B* **2011**, *115*, 1792–1797.
[56] D. H. Dunlap, P. E. Parris, V. M. Kenkre, *Phys. Rev. Lett.* **1996**, *77*, 542–545.
[57] B. Baumeier, F. May, C. Lennartz, D. Andrienko, *J. Mater. Chem.* **2012**, *22*, 10971–10976.
[58] B. Kramer, A. MacKinnon, *Rep. Prog. Phys.* **1993**, *56*, 1469–1564.
[59] N. Vukmirović, *Phys. Chem. Chem. Phys.* **2013**, *15*, 3543–3551.
[60] J. M. Granadino-Roldan, N. Vukmirović, M. Fernandez-Gomez, L.-W. Wang, *Phys. Chem. Chem. Phys.* **2011**, *13*, 14500–14509.
[61] D. L. Cheung, D. P. McMahon, A. Troisi, *J. Am. Chem. Soc.* **2009**, *131*, 11179–11186.
[62] S. Fratini, S. Ciuchi, *Phys. Rev. Lett.* **2009**, *103*, 266601.
[63] S. Ciuchi, S. Fratini, *Phys. Rev. Lett.* **2011**, *106*, 166403.
[64] B. L. M. Hendriksen, F. Martin, Y. Qi, C. Mauldin, N. Vukmirovic, J. Ren, H. Wormeester, A. J. Katan, V. Altoe, S. Aloni, J. M. J. Frechet, L.-W. Wang, M. Salmeron, *Nano Lett.* **2011**, *11*, 4107–4112.
[65] A. B. Chwang, C. D. Frisbie, *J. Appl. Phys.* **2001**, *90*, 1342–1349.
[66] J. Chen, C. K. Tee, M. Shtein, J. Anthony, D. C. Martin, *J. Appl. Phys.* **2008**, *103*, 114513.
[67] J. Rivnay, L. H. Jimison, J. E. Northrup, M. F. Toney, R. Noriega, S. Lu, T. J. Marks, A. Facchetti, A. Salleo, *Nat. Mater.* **2009**, *8*, 952–958.
[68] S. Verlaak, V. Arkhipov, P. Heremans, *Appl. Phys. Lett.* **2003**, *82*, 745–747.
[69] G. Horowitz, *Adv. Funct. Mater.* **2003**, *13*, 53–60.
[70] S. Verlaak, P. Heremans, *Phys. Rev. B* **2007**, *75*, 115127.
[71] M. Mladenović, N. Vukmirović, I. Stanković, *J. Phys. Chem. C* **2013**, *117*, 15741–15748.
[72] L. G. Kaake, P. F. Barbara, X.-Y. Zhu, *J. Phys. Chem. Lett.* **2010**, *1*, 628–635.
[73] G. Nan, Z. Li, *Org. Electron.* **2011**, *12*, 2198–2206.
[74] J. L. Brédas, J. P. Calbert, D. A. da Silva Filho, J. Cornil, *Proc. Natl. Acad. Sci. U. S. A.* **2002**, *99*, 5804–5809.
[75] H. Bassler, *Phys. Status Solidi B* **1993**, *175*, 15–56.
[76] P. M. Borsenberger, L. Pautmeier, H. Bassler, *J. Chem. Phys.* **1991**, *94*, 5447–5454.
[77] S. D. Baranovskii, *Phys. Status Solidi B* **2014**, *251*, 487–525.
[78] R. Coehoorn, W. F. Pasveer, P. A. Bobbert, M. A. J. Michels, *Phys. Rev. B* **2005**, *72*, 155206.
[79] A. Miller, E. Abrahams, *Phys. Rev.* **1960**, *120*, 745–755.
[80] A. Lukyanov, D. Andrienko, *Phys. Rev. B* **2010**, *82*, 193202.
[81] S. Marianer, B. I. Shklovskii, *Phys. Rev. B* **1992**, *46*, 13100–13103.
[82] F. Jansson, S. D. Baranovskii, F. Gebhard, R. Osterbacka, *Phys. Rev. B* **2008**, *77*, 195211.
[83] N. Vukmirović, L.-W. Wang, *Phys. Rev. B* **2010**, *81*, 035210.
[84] H. Cordes, S. D. Baranovskii, K. Kohary, P. Thomas, S. Yamasaki, F. Hensel, J.-H. Wendorff, *Phys. Rev. B* **2001**, *63*, 094201
[85] G. Juška, K. Genevičius, K. Arlauskas, R. Österbacka, H. Stubb, *Phys. Rev. B* **2002**, *65*, 233208.
[86] V. Ambegaokar, B. I. Halperin, J. S. Langer, *Phys. Rev. B* **1971**, *4*, 2612–2620.
[87] C. Tanase, E. J. Meijer, P. W. M. Blom, D. M. de Leeuw, *Phys. Rev. Lett.* **2003**, *91*, 216601.
[88] N. I. Craciun, J. Wildeman, P. W. M. Blom, *Phys. Rev. Lett.* **2008**, *100*, 056601.
[89] J.-D. Picon, M. N. Bussac, L. Zuppiroli, *Phys. Rev. B* **2007**, *75*, 235106.
[90] Y.-C. Cheng, R. J. Silbey, *J. Chem. Phys.* **2008**, *128*, 114713.
[91] F. Ortmann, F. Bechstedt, K. Hannewald, *Phys. Rev. B* **2009**, *79*, 235206.
[92] K. Hannewald, V. M. Stojanovic, J. M. T. Schellekens, P. A. Bobbert, G. Kresse, J. Hafner, *Phys. Rev. B* **2004**, *69*, 075211.
[93] H. Ishii, K. Honma, N. Kobayashi, K. Hirose, *Phys. Rev. B* **2012**, *85*, 245206.
[94] P. V. Parandekar, J. C. Tully, *J. Chem. Phys.* **2005**, *122*, 094102.
[95] J. C. Tully, *J. Chem. Phys.* **1990**, *93*, 1061–1071.
[96] L. Wang, D. Beljonne, *J. Phys. Chem. Lett.* **2013**, *4*, 1888–1894.
[97] N. F. Mott, E. A. Davis, *Electronic Processes in Non-Crystalline Materials*, Clarendon Press, New York, USA **1979**.
[98] S. A. Choulis, Y. Kim, J. Nelson, D. D. C. Bradley, M. Giles, M. Shkunov, I. McCulloch, *Appl. Phys. Lett.* **2004**, *85*, 3890–3892.

THE JOURNAL OF PHYSICAL CHEMISTRY C

Article

pubs.acs.org/JPCC

Spontaneous Polarization Induced by Side Chains in Ordered Poly(3-hexylthiophene)

Marko Mladenović[†,‡] and Nenad Vukmirović*[,†]

[†]Scientific Computing Laboratory, Institute of Physics Belgrade, University of Belgrade, Pregrevica 118, 11080 Belgrade, Serbia

[‡]School of Electrical Engineering, University of Belgrade, P.O. Box 35-54, 11120 Belgrade, Serbia

ABSTRACT: We have found that ordered poly(3-hexylthiophene) (P3HT) exhibits spontaneous polarization along the backbone direction. This effect is caused by the lack of inversion symmetry due to head-to-tail side-chain arrangement. We have also shown that spontaneous polarization in ordered P3HT keeps significant values even at room temperature when the effects of thermal disorder are important. Consequently, it has a strong effect on electronic properties of the material. For example, at the interface between the crystalline and amorphous domain in P3HT, the electric field caused by spontaneous polarization confines the delocalized HOMO state to one side of the crystalline domain.

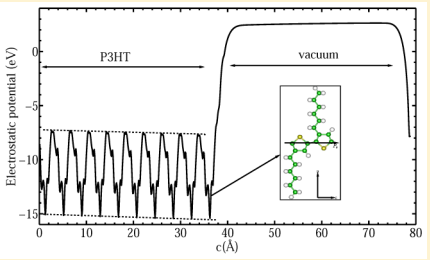

INTRODUCTION

Organic semiconductors have gained a lot of interest in past decades due to their potentially large utilization in optoelectronic devices.[1−5] However, there are still many open questions regarding their electronic and transport properties. Many issues arise from the complexity of the structure of realistic organic semiconductors. Organic solar cells are mostly composed of two different materials. Conjugated polymers used as materials for organic solar cells have complex structure composed of mixed amorphous and crystalline domains.[6,7] Therefore, it is important to take into account all significant effects that take place at the interfaces between different materials or between different domains of the same material. At the interfaces, the effects of spontaneous polarization in materials can play an important role.

Spontaneous polarization is an intrinsic property of a material that it exhibits in the absence of external electric field. It occurs in crystals that do not have a center of inversion symmetry.[8] Such materials are referred to as pyroelectrics. The subgroup of pyroelectrics is ferroelectrics where external electric field alters the orientation of electric dipoles that cause the spontaneous polarization. There are many materials that are known to have high values of spontaneous polarization, such as some oxides, nitrides, etc.[8−11] Within the class of conjugated polymers, polyvinylidene fluoride (PVDF) is reported to have the highest spontaneous polarization of 0.04−0.2 C/m^2.[12,13]

Despite the fact that P3HT serves as a model conjugated polymer and that it has been widely investigated, the effects of spontaneous polarization in this material have not been discussed before. In this paper, the importance of spontaneous polarization in ordered regioregular poly(3-hexylthiophene) (P3HT) is pointed out for the first time. We show that this effect arises from head-to-tail side-chain arrangement which breaks the symmetry along the backbone chain. First, we have calculated spontaneous polarization of ideally crystalline P3HT using density functional theory (DFT)[14] and modern theory of polarization. Next, we demonstrate that the effects of thermal disorder reduce this polarization but still keep it at a significantly large value. Finally, we discuss the effects of spontaneous polarization in crystalline P3HT on electronic properties of the interface between crystalline and amorphous P3HT where the interface is perpendicular to the backbone direction of the P3HT chain.

METHODOLOGY

Under the modern theory of polarization,[15−18] total polarization given as a sum of ionic and electronic polarization can be expressed as

$$\mathbf{P} = \mathbf{P}^{\mathrm{ion}} + \mathbf{P}^{\mathrm{elec}} = \frac{1}{V}\sum_k q_k \mathbf{r}_k + \frac{2ie}{(2\pi)^3}\sum_n \int_{\mathrm{BZ}} \mathrm{d}\mathbf{k}\langle u_{n\mathbf{k}}|\nabla_{\mathbf{k}}|u_{n\mathbf{k}}\rangle \quad (1)$$

where V is the unit cell volume; q_k and $\mathbf{r}_k$ are charges and positions of ions; $u_{n\mathbf{k}}$ are the Bloch functions; and n runs over all occupied bands. The electronic part is calculated using the Berry phase approach. Polarization along axis i is defined as a multivalued quantity, modulo $e|\mathbf{a}_i|/V$, where $\mathbf{a}_i$ is the lattice vector along the i-direction. To obtain a single value for spontaneous polarization, it should be calculated in reference to spontaneous polarization in the centrosymmetric structure.

Spontaneous polarization of an ideal crystal can be calculated using this theory as implemented in several DFT-based computer codes. To calculate the effective polarization in a thermally disordered structure, calculations of systems involving a large number of atoms are required. Standard DFT-based codes are limited to several hundreds of atoms and cannot be used for such systems. An alternative way to extract the

Received: June 2, 2016
Revised: August 2, 2016
Published: August 2, 2016

DOI: 10.1021/acs.jpcc.6b05551
J. Phys. Chem. C 2016, 120, 18895−18900

polarization of the material is from the calculation of electric fields in the system consisting of alternating layers of the material and vacuum. Let us consider such a system consisting of a material with spontaneous polarization P_s along the x-

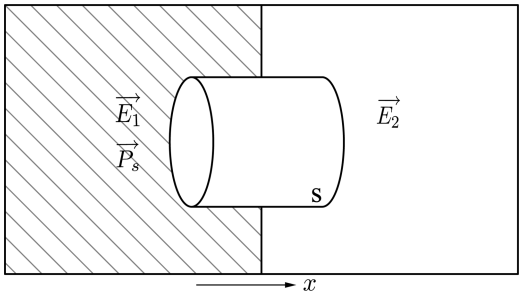

Figure 1. Sketch of the interface between a material with spontaneous polarization and vacuum.

direction and vacuum, as shown in Figure 1. Polarization in the dielectric medium is given by the formula

$$\mathbf{P} = \mathbf{P_s} + \epsilon_o \chi \mathbf{E} \quad (2)$$

where ϵ_o is the electric permittivity of vacuum; χ is the electric susceptibility of material; and $\mathbf{E}$ is the electric field in material. From the definition of the electric displacement vector, it follows that

$$\mathbf{D} = \epsilon_o \mathbf{E} + \mathbf{P} \quad (3)$$

while the Maxwell equation for $\mathbf{D}$ reads

$$\oint_S \mathbf{D} \cdot d\mathbf{S} = \rho \quad (4)$$

If we assume that there is no free charge at the interface between material and vacuum ($\rho = 0$), we obtain the equation $D_1 = D_2$ for the x-projections of the electric displacement vector in material and vacuum, respectively. Using eqs 2 and 3, we then obtain

$$P_s = \epsilon_o E_2 - \epsilon_o \epsilon_r E_1 \quad (5)$$

where ϵ_r is the relative permittivity of material. Hence, spontaneous polarization can be easily obtained with known electric fields in material and vacuum, which can be calculated as electrostatic potential derivatives.

RESULTS

Spontaneous Polarization of Ideally Crystalline P3HT.

Spontaneous polarization of ideally crystalline P3HT was calculated using DFT as implemented in ABINIT[15,17−19] and Quantum ESPRESSO packages.[17,20] We used norm-conversing pseudopotentials with LDA expression for the exchange-correlation term. There are several crystalline structures of P3HT reported in the literature.[21−31] We have considered the aligned structure (Figure 2a), where chains are mutually aligned in the $\pi-\pi$ stacking direction (b-direction, not shown in Figure 2). Unit cell parameters for this structure at 0 K, obtained from energy minimization calculated using classical potentials,[32] are a = 15.55 Å, b = 4.1 Å, and c = 7.77 Å, and all angles are 90°. The obtained value for the spontaneous polarization in the backbone direction from both calculations is 6.0×10^{-3} C/m^2. In the other two directions spontaneous polarization is 0. We have additionally checked that the value of spontaneous polarization in the backbone direction remains almost the same upon the structure relaxation. For comparison, spontaneous polarization in nitrides (GaN, InN, AlN) takes values from 2.9 to 8.1×10^{-2} C/m^2,[9] while $BaTiO_3$ has one of the highest reported spontaneous polarizations of around 0.9 C/m^2.[11]

To understand the origin of the spontaneous polarization in the backbone direction, we have calculated the polarization in that direction for the structure without side chains, which is actually polythiophene (PT), shown in Figure 2b. This structure does not have spontaneous polarization in the backbone direction. Additionally, we considered the P3HT unit cell with tail-to-tail side-chain arrangement (Figure 2c). This structure does not show pyroelectric properties as well. Therefore, we have concluded that spontaneous polarization in the first unit cell arises from head-to-tail arrangement of side chains. Atoms in side chains do not have their inversion symmetry pairs, which breaks the symmetry. On the other hand, structures shown in Figure 2b and Figure 2c exhibit

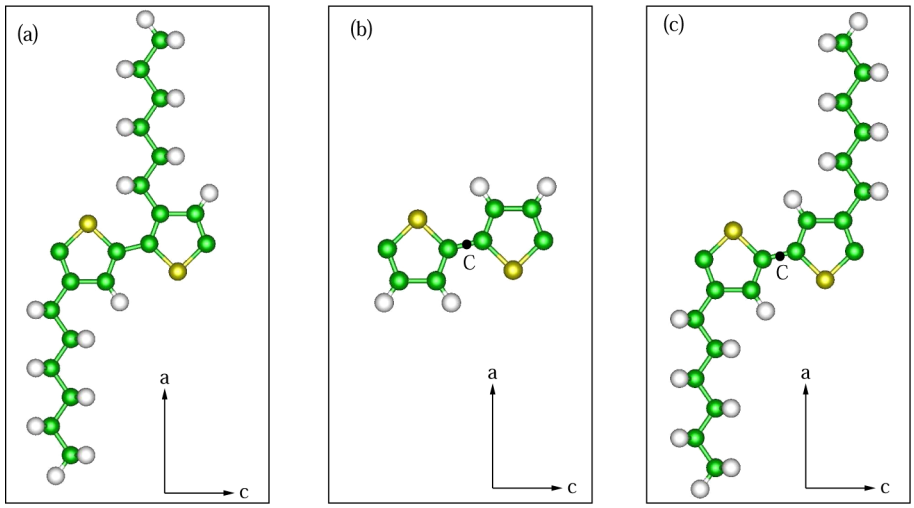

Figure 2. (a) P3HT unit cell with head-to-tail side-chain arrangement, (b) PT unit cell, and (c) P3HT unit cell with tail-to-tail side-chain arrangement.

DOI: 10.1021/acs.jpcc.6b05551
J. Phys. Chem. C 2016, 120, 18895−18900

inversion symmetry where each atom has its corresponding pair.

Structures with head-to-head and tail-to-tail side-chain arrangement are not regioregular, and they are not able to form well-ordered crystalline structure. Therefore, crystalline structure with head-to-tail arrangement of side chains is more representative. Regarding different types of P3HT unit cells, we expect that each unit cell with the lack of the inversion symmetry would have nonzero spontaneous polarization. To check this, we have calculated spontaneous polarization in the shifted structure of P3HT that we considered in our previous works.[33−35] In this structure, two subsequent P3HT chains in the $\pi-\pi$ stacking direction are mutually shifted by the half of the unit cell in the backbone direction. The unit cell parameters for shifted structure at 0 K are a = 15.55 Å, b = 8.1 Å, and c = 7.77 Å, and all angles are 90°.[35] The calculated spontaneous polarization in the backbone direction is 6.2 × 10^{-3} C/m^2, which is nearly the same as that for aligned structure. Therefore, we conclude that spontaneous polarization is robust upon the structure change if the asymmetric arrangement of side chains is preserved. Recently, P3HT unit cell with $P2_1/c$ symmetry group was proposed.[31] This symmetry group is centrosymmetric, and spontaneous polarization in this structure is not expected to occur.

To check the reliability of the alternative method for spontaneous polarization calculation described in the previous section, we have calculated the electrostatic potential along the backbone direction in the supercell that consists of a 10 thiophene ring long rigid P3HT chain and a vacuum region of the same length as the P3HT chain. This potential is shown in Figure 3. Within the material, potential is periodic with an additional linear trend arising from the electric field caused by spontaneous polarization. The peaks of this potential correspond to atom positions. The electric field in P3HT was calculated as a negative derivative of the envelope that connects the peaks. In vacuum, the potential is linear, and electric field is calculated as its negative derivative. The relative permittivity of P3HT is taken to be 4.0.[36] Using eq 5 calculated polarization is 5.6 × 10^{-3} C/m^2, which is very close to the value obtained using DFT-based codes and modern theory of polarization.

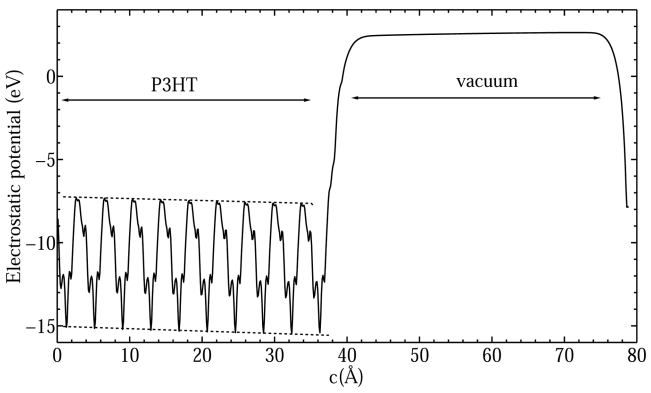

Figure 3. Electrostatic potential along the rigid P3HT chain and vacuum. This potential is one-dimensional, obtained from three-dimensional potential by averaging in two other dimensions.

Spontaneous Polarization of Thermally Disordered P3HT. Next, we consider the effects of temperature on polarization of P3HT. At nonzero temperature the atoms are displaced from their equilibrium positions, and periodicity of the structure is broken. This effect is known as thermal or dynamic disorder and is significant in conjugated polymers.[6,33,34,37,38] Side chains of P3HT are more disordered than backbone chains. It is expected that spontaneous polarization induced by side chains is lower at finite temperature than in a perfectly ordered chain. We used the structures that we produced to investigate the effects of thermal disorder in P3HT.[33,34] Each of the structures contains 2520 atoms arranged in 10 chains. Due to the high number of atoms, electrostatic potential cannot be extracted from DFT-based codes. We instead applied the DFTB+ code,[39] which is based on the density functional tight-binding method.[40] This method is an approximation of classical DFT where Kohn−Sham orbitals are represented by a linear combination of atomic orbitals and two center approximation is made in the Kohn−Sham Hamiltonian matrix. To check if DFTB+ gives the same results as ABINIT or Quantum ESPRESSO, we have calculated electrostatic potential for the structure we used to test the method for the spontaneous polarization calculation. This potential (shown in Figure 4 with a dashed line) was calculated as Coulomb potential from the point charges at atom positions, where the charge of an atom is a sum of its ion and electron charges. Obtained potential differs from the potential obtained by DFT-based codes in two ways: (1) it does not contain the exchange-correlation term and (2) atoms are modeled as point charges which is not the case in DFT-based codes. These two differences result in the potential shift and its amplitude oscillation reduction in the P3HT domain. However, potential shape and electric fields in P3HT and vacuum remained almost the same, which resulted in the spontaneous polarization of 6.3 × 10^{-3} C/m^2. Therefore, DFT-based codes can be replaced by the DFTB+ code to calculate the spontaneous polarization for large systems.

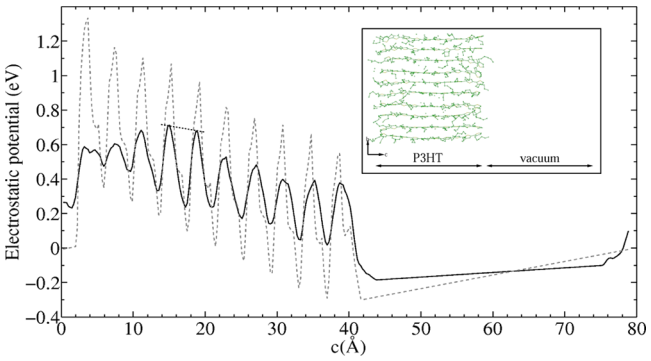

Figure 4. Averaged electrostatic potential along the interface of the disordered P3HT chain and vacuum at 300 K (solid line) and at 0 K (dashed line). The inset shows the structure used to calculate the potential along the interface of thermally disordered P3HT and vacuum.

Averaged electrostatic potential along the backbone direction of P3HT at 300 K for one structure is shown in Figure 4. The potential envelope within the P3HT domain is not unique as for rigid chains. Consequently, the choice of the envelope would affect the obtained value for electric field and spontaneous polarization. To avoid this issue, we took several different structures and calculated averaged electric field. The electric field is calculated in the middle of chains in order to exclude the effects of higher disorder present at the chain edges. The calculated value of polarization is 3.6 × 10^{-3} C/m^2, which

DOI: 10.1021/acs.jpcc.6b05551
J. Phys. Chem. C 2016, 120, 18895−18900

is lower than for the rigid chain. However, this value is significant and shows the important feature that spontaneous polarization in ordered P3HT exists even at room temperature. It is possible that a finite chain used in our simulation exhibits a higher degree of disorder than long realistic chains and that the true value of polarization at room temperature might be even higher. Spontaneous polarization is expected to vanish only for completely disordered chains, as in amorphous domains.

Electrostatic potential in vacuum is linear, and there is no uncertainty of the value for the corresponding electric field. It would be interesting to compare the values for the electric field for structures with rigid and thermally disordered chains since the spontaneous polarization is linearly dependent on the electric field in vacuum (eq 5). The value for the electric field in vacuum for the structure with the rigid chain is 8.0×10^7 V/m, while the corresponding value for thermally disordered chains (averaged over different structures) is 3.4×10^7 V/m. The ratio between these electric fields is close to the ratio between spontaneous polarizations for corresponding structures. Therefore, the electric field in vacuum can be used as a good measure for the estimation of the effect of thermal disorder on the spontaneous polarization in conjugated polymers.

Next, we estimate the possible effect of spontaneous polarization in P3HT on characteristics of P3HT/fullerene blends relevant for solar cell applications. In P3HT/fullerene-based heterojunctions the characteristic length of each domain is on the order of 10 nm. If we assume that layers of P3HT and C60 are arranged in an ideal superlattice where each domain is 10 nm long and that P3HT polarization is perpendicular to the domain interface, we obtain a potential drop in the C60 domain of around 0.9 V at low temperature and around 0.5 V at room temperature (relative permittivity of C60 is taken to be 3.6[41]). These are significant values of potential drop that should strongly affect the performance of bulk heterojunction-based devices. The spontaneous polarization of P3HT can be obtained by experimental electric measurements.[13] Having in mind that the structure of P3HT samples is complex, the experimentally obtained value can differ from that obtained by a theoretical approach. While the superlattice model is certainly a simplification of real bulk heterojunction, it demonstrates the importance of the effect of spontaneous polarization, and one should expect a potential drop of the same order of magnitude in real bulk heterojunctions.

EFFECTS OF SPONTANEOUS POLARIZATION ON ELECTRONIC STATES AT THE INTERFACE BETWEEN CRYSTALLINE AND AMORPHOUS P3HT

Realistic conjugated polymers contain both crystalline and amorphous domains. Average spontaneous polarization in an amorphous domain is 0 due to random orientation of dipoles. If spontaneous polarization exists in a crystalline domain, there is a discontinuity of the polarization at the interface between the crystalline and amorphous domain, analogously to the interface between material with spontaneous polarization and vacuum shown in Figure 1. Hence, there is a surface charge density at the end of the crystalline domain induced by spontaneous polarization, which affects the energy levels in both domains.

In our previous work,[35] we have investigated the electronic states at the interface between crystalline and amorphous domains in P3HT where we found that the highest states in the valence band were delocalized and belonged to the crystalline domain. We have investigated two interface types: (1) a sharp interface between crystalline and amorphous domains where the interface surface is perpendicular to the $\pi-\pi$ stacking direction (type A interface) and (2) a more realistic interface composed of chains extended from the crystalline into the amorphous domain in the backbone direction (type B interface). In the case of the type A interface, spontaneous polarization in P3HT does not have any influence on electronic states as there is no spontaneous polarization along the $\pi-\pi$ stacking direction. On the other hand, in the case of a type B interface, spontaneous polarization effects exist, but they are relatively weak due to the soft transition from ordered to disordered chains. Such transition corresponds to slow spontaneous polarization decline from P_s to 0. Now, we investigate the effects of spontaneous polarization in the backbone direction on the electronic states at the interface between crystalline and amorphous domains where the interface surface is perpendicular to the backbone direction (type C interface). Following the same procedure as in our previous work,[35] the amorphous structure was generated by Monte Carlo simulation by compressing the large box until the density of the amorphous domain reached an experimental value of 1.1 g/cm^3. The temperature during the simulation was 1000 K. Finally, the amorphous domain was cooled to 0 K. The crystalline domain was kept rigid all the time during the simulation. To calculate the electronic structure for obtained atomic structure, the DFTB+ code was used. As expected, the wave function of the highest state in the valence band (Figure 5) is delocalized and belongs to the crystalline domain.

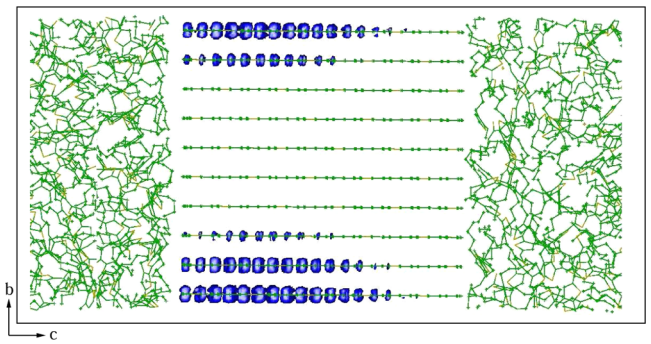

Figure 5. Wave function moduli squared of the highest electronic state in the valence band of the type C interface. Isosurfaces correspond to the probability of finding a hole inside the surface of 75%.

However, due to spontaneous polarization in the backbone direction, the state is confined at one side of the crystalline domain. As one may notice, this interface type is sharp and hence not very realistic. To build a more realistic interface model, effects of thermal disorder and disorder at the crystalline domain edges should be included. We have shown above that spontaneous polarization does not vanish with thermal disorder. Additionally, we have shown in our previous paper[35] that the introduction of an intermediate region between ideal crystalline and amorphous regions (referred to interface type A′) does not qualitatively change the results. Based on these two conclusions, we expect that localization of the wave function at one side of the crystalline domain would be present even in the realistic model. This effect will be completely absent only in the case of centrosymmetric P3HT structure, as that proposed in ref 31. Therefore, spontaneous polarization can significantly affect the electronic properties of conjugated polymers.

DOI: 10.1021/acs.jpcc.6b05551
J. Phys. Chem. C 2016, 120, 18895−18900

CONCLUSIONS

In conclusion, we have shown the existence of spontaneous polarization along the backbone chain in ordered P3HT. This effect is caused by inversion symmetry breaking arising from head-to-tail arrangement of side chains. We proposed the method to calculate spontaneous polarization in large and realistic systems. Then, we applied the method to calculate spontaneous polarization for disordered crystalline P3HT at 300 K and showed that spontaneous polarization is still significant at room temperature. Effects of spontaneous polarization are important at the interfaces between materials with different spontaneous polarization. We have demonstrated that spontaneous polarization confines the hole states at one side of the crystalline domain of P3HT in the presence of the interface between the crystalline and amorphous domain. In organic solar cells electric fields caused by spontaneous polarization can assist or hinder charge separation at the interfaces between different materials, depending on the relative orientation of polarization vectors.

AUTHOR INFORMATION

Corresponding Author

*E-mail: nenad.vukmirovic@ipb.ac.rs. Tel.: +381 11 3713152.

Notes

The authors declare no competing financial interest.

ACKNOWLEDGMENTS

This work was supported by the Ministry of Education, Science, and Technological Development of the Republic of Serbia under project ON171017, by the European Community FP7 Marie Curie Career Integration Grant (ELECTROMAT) and by the European Commission under H2020 project VI-SEEM, Grant No. 675121. The authors would like to acknowledge the contribution of the COST Action MP1406. Numerical simulations were run on the PARADOX supercomputing facility at the Scientific Computing Laboratory of the Institute of Physics Belgrade.

REFERENCES

(1) Friend, R. H.; Gymer, R. W.; Holmes, A. B.; Burroughes, J. H.; Marks, R. N.; Taliani, C.; Bradley, D. D. C.; Santos, D. A. D.; Bredás, J. L.; Logdlund, M.; et al. Electroluminescence in Conjugated Polymers. *Nature* **1999**, *397*, 121−128.

(2) Burroughes, J. H.; Bradley, D. D. C.; Brown, A. R.; Marks, R. N.; Mackay, K.; Friend, R. H.; Burns, P. L.; Holmes, A. B. Light-Emitting Diodes Based on Conjugated Polymers. *Nature* **1990**, *347*, 539−541.

(3) Colvin, V. L.; Schlamp, M. C.; Alivisatos, A. P. Light-Emitting Diodes Made from Cadmium Selenide Nanocrystals and a Semiconducting Polymer. *Nature* **1994**, *370*, 354−357.

(4) Dodabalapur, A.; Torsi, L.; Katz, H. E. Organic Transistors - 2-Dimensional Transport and Improved Electrical Characteristics. *Science* **1995**, *268*, 270−271.

(5) Li, G.; Shrotriya, V.; Huang, J. S.; Yao, Y.; Moriarty, T.; Emery, K.; Yang, Y. High-Efficiency Solution Processable Polymer Photovoltaic Cells by Self-Organization of Polymer Blends. *Nat. Mater.* **2005**, *4*, 864−868.

(6) Noriega, R.; Rivnay, J.; Vandewal, K.; Koch, F. P.; Stingelin, N.; Smith, P.; Toney, M. F.; Salleo, A. A General Relationship Between Disorder, Aggregation and Charge Transport in Conjugated Polymers. *Nat. Mater.* **2013**, *12*, 1038−1044.

(7) Lan, Y.-K.; Huang, C.-I. Charge Mobility and Transport Behavior in the Ordered and Disordered States of the Regioregular Poly(3-hexylthiophene). *J. Phys. Chem. B* **2009**, *113*, 14555−14564.

(8) Wood, C.; Jena, D. *Polarization Effects in Semiconductors: From Ab Initio Theory to Device Applications*; Springer: New York, USA, 2008.

(9) Bernardini, F.; Fiorentini, V.; Vanderbilt, D. Spontaneous Polarization and Piezoelectric Constants of III-V Nitrides. *Phys. Rev. B: Condens. Matter Mater. Phys.* **1997**, *56*, 10024−10027.

(10) Posternak, M.; Baldereschi, A.; Catellani, A.; Resta, R. *Ab initio* Study of the Spontaneous Polarization of Pyroelectric BeO. *Phys. Rev. Lett.* **1990**, *64*, 1777−1780.

(11) Neaton, J. B.; Ederer, C.; Waghmare, U. V.; Spaldin, N. A.; Rabe, K. M. First-Principles Study of Spontaneous Polarization in Multiferroic $BiFeO_3$. *Phys. Rev. B: Condens. Matter Mater. Phys.* **2005**, *71*, 014113.

(12) Sun, F.-C.; Dongare, A. M.; Asandei, A. D.; Pamir Alpay, S.; Nakhmanson, S. Temperature Dependent Structural, Elastic, and Polar Properties of Ferroelectric Polyvinylidene fluoride (PVDF) and Trifluoroethylene (TrFE) Copolymers. *J. Mater. Chem. C* **2015**, *3*, 8389−8396.

(13) Katsouras, I.; Asadi, K.; Li, M.; van Driel, T. B.; Kjaer, K. S.; Zhao, D.; Lenz, T.; Gu, Y.; Blom, P. W. M.; Damjanovic, D.; et al. The Negative Piezoelectric Effect of the Ferroelectric Polymer Poly(vinylidene fluoride). *Nat. Mater.* **2016**, *15*, 78−84.

(14) Parr, R. G.; Yang, W. *Density-Functional Theory of Atoms and Molecules*; Oxford University Press: New York, USA, 1989.

(15) Resta, R. Macroscopic Polarization in Crystalline Dielectrics: the Geometric Phase Approach. *Rev. Mod. Phys.* **1994**, *66*, 899−915.

(16) Spaldin, N. A. A Beginner's Guide to theModern Theory of Polarization. *J. Solid State Chem.* **2012**, *195*, 2−10.

(17) King-Smith, R. D.; Vanderbilt, D. Theory of Polarization of Crystalline Solids. *Phys. Rev. B: Condens. Matter Mater. Phys.* **1993**, *47*, 1651−1654.

(18) Vanderbilt, D.; King-Smith, R. D. Electric Polarization as a Bulk Quantity and its Relation to Surface Charge. *Phys. Rev. B: Condens. Matter Mater. Phys.* **1993**, *48*, 4442−4455.

(19) Gonze, X.; Amadon, B.; Anglade, P.-M.; Beuken, J.-M.; Bottin, F.; Boulanger, P.; Bruneval, F.; Caliste, D.; Caracas, R.; Côté, M.; et al. ABINIT: First-Principles Approach to Material and Nanosystem Properties. *Comput. Phys. Commun.* **2009**, *180*, 2582−2615.

(20) Giannozzi, P.; Baroni, S.; Bonini, N.; Calandra, M.; Car, R.; Cavazzoni, C.; Ceresoli, D.; Chiarotti, G. L.; Cococcioni, M.; Dabo, I.; et al. QUANTUM ESPRESSO: a Modular and Open-Source Software Project for Quantum Simulations of Materials. *J. Phys.: Condens. Matter* **2009**, *21*, 395502.

(21) Alexiadis, O.; Mavrantzas, V. G. All-Atom Molecular Dynamics Simulation of Temperature Effects on the Structural, Thermodynamic, and Packing Properties of the Pure Amorphous and Pure Crystalline Phases of Regioregular P3HT. *Macromolecules* **2013**, *46*, 2450−2467.

(22) Dag, S.; Wang, L.-W. Packing Structure of Poly(3-hexylthiophene) Crystal: Ab Initio and Molecular Dynamics Studies. *J. Phys. Chem. B* **2010**, *114*, 5997−6000.

(23) Xie, W.; Sun, Y. Y.; Zhang, S. B.; Northrup, J. E. Structure and Sources of Disorder in Poly(3-hexylthiophene) Crystals Investigated by Density Functional Calculations with van derWaals Interactions. *Phys. Rev. B: Condens. Matter Mater. Phys.* **2011**, *83*, 184117.

(24) Poelking, C.; Andrienko, D. Effect of Polymorphism, Regioregularity and Paracrystallinity on Charge Transport in Poly(3-hexylthiophene) [P3HT] Nanofibers. *Macromolecules* **2013**, *46*, 8941−8956.

(25) Bhatta, R. S.; Yimer, Y. Y.; Perry, D. S.; Tsige, M. Improved Force Field for Molecular Modeling of Poly(3-hexylthiophene). *J. Phys. Chem. B* **2013**, *117*, 10035−10045.

(26) Moreno, M.; Casalegno, M.; Raos, G.; Meille, S. V.; Po, R. Molecular Modeling of Crystalline Alkylthiophene Oligomers and Polymers. *J. Phys. Chem. B* **2010**, *114*, 1591−1602.

(27) Prosa, T. J.; Winokur, M. J.; Moulton, J.; Smith, P.; Heeger, A. J. X-Ray Structural Studies of Poly(3-alkylthiophenes): an Example of an Inverse Comb. *Macromolecules* **1992**, *25*, 4364−4372.

(28) Colle, R.; Grosso, G.; Ronzani, A.; Zicovich-Wilson, C. M. Structure and X-Ray Spectrum of Crystalline Poly(3-hexylthiophene)

DOI: 10.1021/acs.jpcc.6b05551
J. Phys. Chem. C 2016, 120, 18895−18900

from DFT-van der Waals Calculations. *Phys. Status Solidi B* **2011**, *248*, 1360−1368.
(29) Kayunkid, N.; Uttiya, S.; Brinkmann, M. Structural Model of Regioregular Poly(3-hexylthiophene) Obtained by Electron Diffraction Analysis. *Macromolecules* **2010**, *43*, 4961−4967.
(30) Maillard, A.; Rochefort, A. Structural and Electronic Properties of Poly(3-hexylthiophene) π-stacked Crystals. *Phys. Rev. B: Condens. Matter Mater. Phys.* **2009**, *79*, 115207.
(31) Dudenko, D.; Kiersnowski, A.; Shu, J.; Pisula, W.; Sebastiani, D.; Spiess, H. W.; Hansen, M. R. A Strategy for Revealing the Packing in Semicrystalline p-Conjugated Polymers: Crystal Structure of Bulk Poly-3-hexyl-thiophene (P3HT). *Angew. Chem., Int. Ed.* **2012**, *51*, 11068−11072.
(32) Jorgensen, W. L.; Maxwell, D. S.; Tirado-Rives, J. Development and Testing of the OPLS All-Atom Force Field on Conformational Energetics and Properties of Organic Liquids. *J. Am. Chem. Soc.* **1996**, *118*, 11225−11236.
(33) Mladenović, M.; Vukmirović, N. Effects of Thermal Disorder on the Electronic Properties of Ordered Polymers. *Phys. Chem. Chem. Phys.* **2014**, *16*, 25950−25958.
(34) Mladenović, M.; Vukmirović, N. Charge Carrier Localization and Transport in Organic Semiconductors: Insights from Atomistic Multiscale Simulations. *Adv. Funct. Mater.* **2015**, *25*, 1915−1932.
(35) Mladenović, M.; Vukmirović, N. J. Electronic States at the Interface between Crystalline and Amorphous Domains in Conjugated Polymers. *J. Phys. Chem. C* **2015**, *119*, 23329−23333.
(36) Maillard, A.; Rochefort, A. Role of Structural Order at the P3HT/C60 Heterojunction Interface. *Org. Electron.* **2014**, *15*, 2091−2098.
(37) Cheung, D. L.; McMahon, D. P.; Troisi, A. Computational Study of the Structure and Charge-Transfer Parameters in Low-Molecular-Mass P3HT. *J. Phys. Chem. B* **2009**, *113*, 9393−9401.
(38) Cheung, D. L.; McMahon, D. P.; Troisi, A. A Realistic Description of the Charge Carrier Wave Function in Microcrystalline Polymer Semiconductors. *J. Am. Chem. Soc.* **2009**, *131*, 11179−11186.
(39) Aradi, B.; Frauenheim, B. H. T. DFTB+, a Sparse Matrix-Based Implementation of the DFTB Method. *J. Phys. Chem. A* **2007**, *111*, 5678−5684.
(40) Elstner, M.; Porezag, D.; Jungnickel, G.; Elsner, J.; Haugk, M.; Frauenheim, T.; Suhai, S.; Seifert, G. Self-Consistent-Charge Density-Functional Tight-Binding Method for Simulations of Complex Materials Properties. *Phys. Rev. B: Condens. Matter Mater. Phys.* **1998**, *58*, 7260−7268.
(41) Snyder, C. R.; Douglas, J. F. Determination of the Dielectric Constant of Nanoparticles. 1. Dielectric Measurements of Buckminsterfullerene Solutions. *J. Phys. Chem. B* **2000**, *104*, 11058−11065.

DOI: 10.1021/acs.jpcc.6b05551
J. Phys. Chem. C 2016, 120, 18895−18900